Plasticity and Stability of the Cortical Wiring in the Human Visual System

Dissertation
zur Erlangung des akademischen Grades

doctor rerum naturalium (Dr. rer. nat.)

genehmigt durch die Fakultät für Naturwissenschaften
der Otto-von-Guericke-Universität Magdeburg

von: **MSc, Khazar Ahmadi**
geboren am 31. Januar 1988 in Tabriz, Iran

Gutachter: apl. Prof. Dr. rer. nat. Michael Hoffmann
Prof. Dr. rer. nat. Mark W. Greenlee

eingereicht am: 19. Juni 2019
verteidigt am: 28. Oktober 2019

To my life companion, who held my hands in the dark
To my parents, who launched me towards the heavens
To the loving memory of my grandmother

گویند عارفان هنر و علم کیمیاست

وان مس که گشت همسر این کیمیا طلاست

فرخنده طائری که بدین بال و پر پرد

همدوش مرغ دولت و هم عرصهء هماست

The men of knowledge say that art and science is a philosopher's stone and that the copper that associates with this philosopher's stone becomes gold.

How happy is the bird that can fly with this wing and pinion (i.e. art and science), it would fly wing by the wing of the bird of felicity and would share with the arena of phoenix.

Parvin E'tesami (1907 – 1941)
Persian poet

Acknowledgements

There are many people to whom I am indebted for their advice, encouragement and kindness. First, I would like to thank my supervisor, Prof. Michael Hoffmann, for giving me an invaluable opportunity to pursue research in his lab. His continuous support and guidance through these years helped me to develop the skills required for a successful career in academia. I count myself very fortunate to have had a nice network of colleagues and collaborators including members of the visual processing laboratory, the staff of the department of ophthalmology, magnetic resonance imaging center at Otto-von-Guericke University and the Leibniz Institute for Neurobiology for their help in recruiting participants, ophthalmological examinations and acquisition of the fMRI scans. In addition, special thanks go to Dr. Alessio Fracasso from the University of Glasgow and Prof. Serge Dumoulin from Utrecht University who helped me with the analysis of ultra-high resolution data. I would like to extend my appreciation to Prof. Antony Morland and Dr. Andre Gouws for introducing us a unique case with chiasma hypoplasia, and for doing fMRI-based pRF mapping over a weekend in York. I would also like to express my sincere gratitude to all the participants of my studies who often travelled a long distance from different cities of Germany or abroad to Magdeburg with no personal advantages to support our experiments. Finally and yet importantly, I am deeply grateful to my family. I would never have ended up here without my parents who made my education a priority over everything else in their lives. I am also thankful to my brother for his constant support and belief in me and I owe my heartful thanks to my beloved husband, Jahangir, who has been my devoted supporter and best friend sharing all the ups and downs of my adventure through a PhD.

Contributions

The contribution of the co-authors and colleagues to the present thesis is as follows:

Data presented in **chapter 5** were acquired by Dr. Aringrim, Dr. Hougaard and Dr. Amin in Danish headache center and department of neurology at the University of Copenhagen, Glostrup, Denmark. Ms. Ahmadi analyzed the fMRI data and contributed to drafting the manuscript together with Dr. Aringrim, Dr. Hougaard, Dr. Vestergaard, Prof. Hoffmann and Prof. Ashina. The remainder of the authors provided valuable assistance in the design and conception of the study.

Data presented in **chapter 6** were collected in the University medical center, Utrecht, the Netherlands. The two FHONDA individuals were referred by Dr. van Genderen and Ms. Kruijt. Dr. Fracasso and Mr. van Dijk were involved in fMRI data acquisition. Moreover, Dr. Fracasso provided assistance in methodological development and revision of the paper. Ms. Ahmadi analyzed the data and wrote the bulk of the paper. Prof. Hoffmann and Prof. Dumoulin contributed to the interpretation of the results and improvement of the manuscript.

Data presented in **chapter 7** were collected at two sites. The ultra-high resolution fMRI data were obtained at Leibnitz Institute for Neurobiology and the diffusion-weighted imaging data (DWI) were collected at magnetic resonance imaging center at Otto-von-Guericke University. Both fMRI and DWI scannings were performed in Magdeburg, Germany. In addition, population receptive field (pRF) mapping was conducted at York neuroimaging center (York, UK). The participant with chiasma hypoplasia who took part in this study was referred by Prof. Morland and Dr. Gouws. The analysis of the DWI data was performed by Mr. Puzniak. Ms. Ahmadi modified the fMRI stimuli, analyzed all the fMRI-related data and wrote the manuscript together with Mr. Puzniak. Professors. Hoffmann, Dumoulin, Morland, Speck and Pestilli, as well as Dr. Fracasso contributed to the interpretation of the results and provided comments for the manuscript. The remainder of the authors provided valuable assistance in the design and conception of the study.

Data presented in **chapter 8** were acquired in magnetic resonance imaging center at Otto-von-Guericke University, Magdeburg, Germany. Ms. Ahmadi optimized the fMRI stimuli, analyzed the data and wrote the paper. Prof. Hoffmann contributed to interpretation of the results and refined the manuscript. Visual Evoked Potentials (VEPs), ophthalmological examinations, microperimetry and assessment of visual acuity in the albinotic participants were performed at the department of ophthalmology by Ms. Reupsch, Dr. Wagner, Dr. Herbik and Ms. Heinecke respectively.

Contents

Abstract

Deciphering the mechanisms of cortical plasticity is an ultimate goal of neuroscience, as harnessing these mechanisms can foster the development of novel treatments for many neurological disorders. Using state-of-the-art brain imaging techniques, the current thesis describes the organization of the human visual cortex and its scope of plasticity and stability in four different conditions, ranging from intermittent visual dysfunction in (i) migraine to a variety of congenital chiasmal abnormalities in (ii) FHONDA, (iii) chiasmahypoplasia, and (iv) albinism.

(i) Migraine attacks are often preceded by visual anomalies known as aura. The underlying mechanisms of migraine aura are not fully understood, due to the highly challenging task of capturing patients during aura. Using functional magnetic resonance imaging (fMRI) at 3 T, the alterations of the visual cortex were assessed in five patients with migraine during various forms of aura. The blood oxygen level dependent (BOLD) signal was reduced in patients reporting negative symptoms, i.e. scotoma, and increased in patients who experienced positive symptoms such as flickering or flashing lights. Furthermore, patients with bilateral visual symptoms had corresponding bihemispherical changes in BOLD response. These findings suggest that different aura symptoms reflect different types of cerebral dysfunction.

Due to misrouting of the optic nerves at the optic chiasm, the visual cortex receives large scale abnormal input in congenital chiasmal abnormalities. Strikingly, the visual perception and basic visual functions remain intact, despite the gross anatomical malformation. This renders congenital chiasmal abnormalities as powerful models to uncover the interplay of developmental plasticity in the human visual cortex. In this thesis, the cortical organization was investigated in three types of these abnormalities, namely, FHONDA, chiasma hypoplasia and albinism.

(ii) FHONDA (foveal hypoplasia, optic nerve decussation defects and anterior segment dysgenesis) is a rare new entity of congenital chiasmal abnormalities, characterized by abnormal crossing of the temporal retinal fibers to the contralateral hemisphere in the absence of any pigmentation deficits. The population receptive field (pRF) properties of the visual cortex were determined in two affected individuals. Using fMRI at 7 T, two superimposed hemifield representations were observed on the hemisphere contralateral to the stimulated eye with bilateral pRFs, mirrored across the vertical meridian. This direct evidence of abnormal mapping in FHONDA highlights the independence of pigmentation and development of the visual cortex.

(iii) The observed superposition of the two hemifield representations prompts the question, whether the capacity of the visual cortex is limited to two superimposed maps or

there are plastic mechanisms available to host more maps. To address this question, the cortical organization in a rare individual with chiasma hypoplasia was determined. Using ultra-high resolution fMRI at 7 T and diffusion-weighted imaging (DWI) at 3 T, three hemiretinal inputs were found to converge onto the left hemisphere. Additionally, fMRI-based pRF mapping of the left V1-V3 revealed three superimposed hemifield representations in the left visual cortex, i.e. two representations of opposing visual hemifields from the left eye and one right hemifield representation from the right eye. These findings demonstrate that the developmental plasticity in the human visual cortex provides sufficient scope to support the coexistence and functioning of three hemifield maps within one hemisphere.

(iv) In albinism, the pathological decussation of the temporal retinal afferents at the optic chiasm leads to superimposed representations of opposing hemifields in the visual cortex. Applying fMRI-based pRF mapping and connective field (CF)-modeling at 3 T, the early visual cortex was investigated in 6 albinotic participants and 4 controls. In albinism, superimposed retinotopic representations of the contra- and ipsilateral visual hemifield were observed on the hemisphere contralateral to the stimulated eye. This was confirmed by the observation of bilateral pRFs during bilateral mapping. Hemifield mapping revealed similar pRF-sizes for both hemifield representations throughout V1 to V3. The typical increase of V1-sampling extent for V3 compared to V2 was absent in the albinotic participants. The similarity of the pRF-sizes for opposing visual hemifield representations highlights the equivalence of the two maps in the early visual cortex. The altered V1-sampling extent in V3 indicates the adaptation of cortico-cortical connections to the abnormal input of the visual cortex. These results thus suggest that conservative developmental mechanisms are complemented by alterations of the extrastriate cortico-cortical connectivity.

In conclusion, the findings of the current thesis indicate, on the one hand, a close correspondence of cortical signals and visual symptoms as demonstrated for migraine aura. On the other hand, in congenital chiasmal abnormalities, the interplay of subcortical stability and cortical plasticity appears to provide sufficient scope to preserve basic aspects of visual perception. The present thesis, therefore, provides significant insights into the development and reorganization of the visual system which may influence new therapeutic approaches.

Zusammenfassung

Ein bedeutendes Ziel der Neurowissenschaften ist die Erforschung der Mechanismen kortikaler Plastizität. Dieses Wissens kann helfen, neuartige Therapien für neurologische Erkrankungen zu entwickeln. Die vorliegende Arbeit beschreibt unter Verwendung modernster bildgebender Verfahren die Organisation und Plastizität des menschlichen visuellen Kortex bei folgenden Erkrankungen: bei (i) visueller Dysfunktion im Rahmen intermittierender Kopfschmerzen (Migräne) bis hin zu angeborenen Chiasma-Abnormalitäten bei (ii) FHONDA, (iii) Chiasma-Hypoplasie und (iv) Albinismus.

(i) Migräneattacken gehen oft mit visuellen Symptomen einher, die auch als Aura bekannt sind. Die grundlegenden Mechanismen der Migräne-Aura sind bis heute nicht vollständig geklärt, da insbesondere die Datenerhebung an Migränepatienten während eines Aura-Erlebnisses die Forscher vor große Herausforderungen stellt. Die Veränderungen des visuellen Kortex wurde bei fünf Patienten mit Migräne während Aura-Erlebnis mit unterschiedlicher Ausprägung untersucht. Mit Hilfe funktioneller Magnetresonanztomographie (fMRT) bei einer Magnetfeldstärke von 3 T konnte nachgewiesen werden: (i) ein signifikant reduziertes BOLD-Signal (engl. "blood oxygenation level dependent", abhängig vom Blutsauerstoffgehalt) bei Patienten, die sogenannte negative Symptome (Gesichtsfelddefekte) berichteten, und (ii) ein signifikant erhöhtes BOLD-Signal bei Patienten mit potiviten Aura-Symptomen (zusätzliche Wahrnehmung von Strukturen). Bei Patienten mit bilateralen visuellen Symptomen wurde zudem eine entsprechende bihemisphärische Änderung in der BOLD-Antwort nachgewiesen. Diese Befunde legen nahe, dass verschiedene Aura-Symptome sich auch in verschiedenen Arten zerebraler Dysfunktion widerspiegeln.

Bei angeborenen Chiasma-Abnormalitäten ist der Eingang visueller Informationen in den Kortex aufgrund von Fehlbildungen der Sehnervenkreuzung (Chiasma opticum) verändert. Auffallend ist, dass die visuelle Wahrnehmung und grundlegende Sehfunktionen trotz der anatomischen Fehlbildung weitgehend unversehrt bleiben. Deshalb sind angeborene Abnormalitäten des Chiasma opticum besonders gut geeignete Modelle, um plastische Entwicklungsprozesse im menschlichen visuellen Kortex aufzudecken. In dem zweiten Teil in vorliegender Arbeit wurde die kortikale Organisation in drei Formen dieser Chiasma-Abnormalitäten untersucht: FHONDA, Chiasmale Hypoplasie und Albinismus.

(ii) FHONDA (engl. "foveal hypoplasia, optic nerve decussation defects and anterior segment dysgenesis") ist eine noch relativ unbekannte Form einer angeborenen Fehlbildung des Chiasma opticum. Sie ist gekennzeichnet durch eine abnormale Kreuzung der temporalen Netzhautfasern in die kontralaterale Hemisphäre ohne Pigmentierungsdefizite (im Gegensatz zu dem unten beschriebenen Albinismus). Hier wurden die Eigenschaften

der rezeptiver Felder (engl. "population receptive field; pRF) des visuellen Kortex bei zwei betroffenen Probanden Bestimmt. Mit funktioneller MRT bei einer Magnetfeldstärke von 7 T konnten zwei überlagerte Halbfeld-Repräsentationen auf der kontralateralen Hemisphäre mit bilateralen pRFs, gespiegelt am vertikalen Meridian, nachgewiesen werden. Dieser Beleg einer abnormalen Kartierung bei FHONDA zeigt die Unabhängigkeit der Entwicklung des visuellen Kortex von der Pigmentierung.

(iii) Die Ergebnisse aus eine Überlagerung beider Halbfeld-Repräsentationen führen zu der Frage, ob die Kapazität des visuellen Kortex auf zwei übereinander liegende Karten beschränkt ist oder ob weitere Karten hinzugefügt werden können. Um diese Frage zu beantworten, wurde die kortikale Organisation bei einem seltenen Individuellen mit Chiasma-Hypoplasie bestimmt. Mit ultrahochauflösender fMRT bei einer Magnetfeldstärke von 7 T und zusätzlicher Diffusionsbildgebung (engl. "diffusion-weighted imaging; DWI") bei 3 T wurde drei Eingänge von Informationen aus der Netzhaut in eine die linke - Hemisphäre gefunden. Des Weiteren zeigte pRF-Kartierung von V1-V3 im visuellen Kortex drei überlagerte Halbfeld-Repräsentationen in der linken Hemisphäre: zwei Abbildungen gegenüberliegender visueller Halbfeld-Repräsentationen des linken Auges und eine rechte Halbfeld-Repräsentation des rechten Auges. Diese Ergebnisse zeigen, dass das Potential des menschlichen visuellen Kortex zu plastischer Entwicklung ausreichend Spielraum bietet, um die Koexistenz und Funktionsfähigkeit dreier Halbfeld-Repräsentationen auf einer Hemisphäre gewährleisten zu können.

(iv) Bei Albinismus führt eine fehlerhafte Kreuzung temporaler Netzhautfasern am Chiasma opticum zu einer überlagerten Repräsentation gegenberliegender visueller Halbfelder im visuellen Kortex. Unter Verwendung funktioneller MRT bei einer Magnetfeldstärke von 3 T wurden die pRF-Eigenschaften und die Vernetzung (engl. "connective field; CF") primärer visueller Areale in 6 albinotischen Teilnehmern und 4 Kontrollen untersucht. Bei Albinismus wurden überlagerte retinotope Repräsentationen des kontra- und ipsilateralen visuellen Halbfeldes auf der Hemisphäre kontralateral zum stimulierten Auge beobachtet. Dies wurde durch den Nachweis bilateraler pRFs bei bilateraler Kartierung bestätigt. Die Halbfeld-Kartierung zeigte ähnliche pRF-Größen für beide Halbfeld-Repräsentationen in V1 bis V3, was die Gleichwertigkeit beider Karten in frühen visuellen Arealen anzeigt. Das im Vergleich zu V2 in V3 erhöhte 'sampling' von V1 wurde für albinotische Teilnehmer nicht belegt. Diese Ergebnisse legen nahe, dass konservative Entwicklungsmechanismen allein nicht ausreichen, sondern um Mechanismen, die zu Veränderungen in der extrastriären kortiko-kortikalen Konnektivität führen, ergänzt werden müssen.

Zusammenfassend weist die vorliegende Arbeit auf eine enge Verbindung zwischen kortikalen Signalen und visuellen Symptomen bei Migräne hin. Darüber hinaus zeigt diese Arbeit, dass bei kongenitalen Erkrankungen des Chiasma opticum und daraus resultierender Fehlkreuzung grundlegende Mechanismen visueller Wahrnehmung durch das Zusammenspiel subkortikaler Stabilität und kortikaler Plastizität erhalten bleiben. Mit dieser Arbeit werden bedeutende Einblicke in die Entwicklung und Reorganisation des visuellen Systems geliefert, die insbesondere die Entwicklung neuer therapeutischer Ansätze beeinflussen können.

Chapter 1

Introduction

The rich stream of visual input is processed within the visual cortex which spans about 20% of the entire cortical surface (Wandell et al., 2009). The functional architecture of the visual cortex is organized in a topographic manner, i.e. adjacent cortical locations respond to nearby points in the visual field, giving rise to visual field maps that are also called retinotopic maps (Brewer et al., 2005; Hoffmann and Dumoulin 2015). Recent advancements in functional magnetic resonance imaging (fMRI), experimental methods and data analysis algorithms have led to the identification of multiple visual field maps that cover the entire occipital lobe and extend into temporal and parietal cortices. Quantitative measurement of these maps can provide an important key to understand the nature of pathologies, their symptoms and the interplay of stability and reorganization (plasticity) in the visual cortex (Baseler et al., 2011; Hoffmann et al., 2012; Masuda et al., 2008; Wandell et al., 2007).

A comparatively mild visual system pathology which allows investigating the link between transient visual symptoms and underlying cortical activation patterns is Migraine, a debilitating disease often preceded by homonymous visual disturbances known as aura (Arngrim et al., 2017a; Hadjikhani et al., 2001; Hougaard et al., 2014, 2013). Typically, aura comprises scintillating and shining zigzag patterns which begin at the centre of vision and expand peripherally over 5 - 20 min, within the visual field. The scintillations are temporarily followed by a blind region (scotoma) with the same retinotopic progression from central to peripheral visual field (Hadjikhani et al., 2001; Vincent and Hadjikhani 2007). The predominance of visual symptoms during aura attacks suggests that the pathophysiology of migraine, at least partially, involves the visual system. The exact mechanism of the aura is not known however several lines of evidence indicate that cortical spreading depression (CSD) might be an underlying cause of aura which is characterized by a spreading wave of neuronal hyperactivity followed by suppression of neuronal firing (Ayata and Lauritzen 2015; Leo and Morison 1945; Olesen et al., 2000). Due to the unpredictable and short-lasting nature of aura, direct studies of CSD in humans have been rare. Changes in cortical activation spread during aura can be measured in relation to visual field maps. Moreover, the correlation between different aura symptoms and the effects of CSD on brain activity can be validated in vivo using fMRI with potential prognostic and therapeutic implications (Arngrim et al., 2017a).

A prerequisite for the preservation of the visual field maps is the partial crossing of the optic nerves at the optic chiasm, ensuring that each hemisphere receives binocular information about the contralateral visual field. While acquired damage to the optic chiasm results in blindness in specific parts of the visual field, congenital chiasmal malformations leave major aspects of visual function intact even though visual field maps are substantially disrupted (Hoffmann and Dumoulin 2015). The partial decussation of the optic nerves in such conditions can be reduced as reported in achiasma, and hemihydra-nencephaly (Apkarian et al., 1994; Fracasso et al., 2016; Hoffmann et al., 2012; Muckli et al., 2009; Victor et al., 2000) or enhanced in albinism and FHONDA (Apkarian et al., 1983; Al-Araimi et al., 2013; von dem Hagen et al., 2008). Consequently, the visual cortex receives input not only from the contra- but also from the ipsilateral visual hemifield resulting in superimposed visual field representations. Regardless of the misrouting type, the challenge of the visual cortex is the same, i.e. incorporating large-scale erroneous input. Hence, congenital chiasmal abnormalities provide a unique opportunity to study the foundations of visual pathways formation and the scope of plasticity in the human visual system.

This thesis seeks to elucidate the neural processes that are triggered by pathologies of the visual system and thus aims to detail the interplay of stability and plasticity in the human visual system. For this purpose, four different disorders are investigated that span the range from temporary visual symptoms, as evident in the multifaceted phenomenology of the migraine aura, to profound congenital changes of the visual system anatomy, as evident in abnormalities of the optic chiasm. Chapter 2 provides a brief overview of the physiology and pathophysiology of the visual system. The main techniques and the analytical method employed throughout the experiments are discussed in chapter 3. Afterwards, the research questions are detailed in chapter 4. Chapter 5 describes how negative and positive migraine aura symptoms correlate with fMRI responses in the visual cortex. The remainder of the chapters focus on the developmental mechanisms that reflect the interplay of plasticity and stability in congenital chiasmal abnormalities. Chapter 6 investigates the extent of cortical plasticity in a new inherited visual pathway disorder called FHONDA. Chapter 7 provides the first evidence for the accommodation of three hemifield maps in an individual with chiasma hypoplasia. In chapter 8, population receptive field properties and functional cortico-cortical connectivity are characterized in albinism to further deepen our understanding of the cortical organization in this disorder. The thesis wraps up with a general discussion of the findings in chapter 9.

Chapter 2

Human visual system

2.1 From the retina to the brain

Processing of the visual information begins with translation of the light into electrical impulses at retina, an intricate layered structure comprising a variety of cell types. Photoreceptors including rods and cones are located at deepest layers of the retina. Rods situated in peripheral retina are involved in scotopic vision. In contrast, cones with a greater density in the central retina are specialized in high spatial resolution (acuity) under photopic conditions (Provis et al., 1998). There are three types of cone cells that respond to the short, middle and long wavelength of light respectively. The middle layers of retina contain bipolar, horizontal and amacrine nerve cells. Bipolar cells receive input from the photoreceptors and pass it to the retinal ganglion cells (RGCs) through direct synapses or via amacrine cells. Horizontal cells are laterally connecting interneurons which regulate photoreceptors by providing inhibitory feedbacks (Erskine and Herrera 2014; Thoreson et al., 2008). Based on physiological, morphological and molecular criteria, RGCs are classified into approximately 30 types. Each type extracts distinct visual features in parallel for transmission to the brain (Baden et al., 2016; Sanes and Masland 2015). The axons of RGCs leave the retina at the optic disc and form the optic nerve. The optic nerve fibers meet at optic chiasm which is an X-shaped intersection located at the base of the hypothalamus. In this region, fibers from nasal retina decussate the midline and project to the contralateral hemisphere while fibers from temporal retina remain uncrossed and project ipsilaterally (Erskine and Herrera 2014; Hoffmann and Dumoulin 2015). This arrangement allows the visual cortex to receive input from both eyes corresponding to the same visual hemifield and is thus vital for binocular vision. The relative size of the crossed and uncrossed projections varies across species and depends on frontalization of the eyes. For instance, in primates the number of ipsi- and contralateral fibers is approximately equal. Specifically, the reported ratio in humans is 47/53, respectively (Kupfer et al., 1967). In contrast, the percentage of ipsilateral axons is as low as $2-3$ % in animals with laterally positioned eyes such as rodents (Jeffery and Erskine 2005). After leaving chiasm, ipsilateral optic nerve fibers combined with contralateral fibers from the fellow eye form the optic tracts. The majority of optic tract axons terminate in the lateral geniculate nucleus (LGN), whereas the remainder relay information towards pulvinar and

superior colliculus. The cells within the LGN are arranged in six distinct layers each of which receives only monocular input. The first two ventral layers contain relatively large magnocellular neurons while the four dorsal layers consist of small parvocellular neurons (Livingstone and Hubel 1988). Intercalated to the magno- and parvocellular layers are granular cells known as koniocellular neurons (Kaas et al., 1978). The ipsilateral input of the temporal retina is transmitted to layers 2, 3, and 5 while the contralateral fibers of the nasal retina project to layers 1, 4, and 6 (Forrester et al., 2015). The optic radiation forwards the signal from LGN to V1 located around the calcarine sulcus of the occipital lobe (Figure 2.1). V1 is the first cortical area to receive visual input and is also known as the striate cortex due to the predominance of easily identifiable myelinated fibers within layer IV called the stria of Gennari (Dougherty et al., 2003; Trampel et al., 2011). In V1, the binocular input of the LGN is organized in an interleaved manner forming ocular dominance domains that are driven either by the left or the right eye.

Each hemifield is represented on the contralateral V1. The upper quadrants of the visual field are represented on the lower bank of the calcarine (lingual gyrus), while the lower quadrants are represented on the upper bank (cuneus). Consequently, the V1 map is inverted with respect to the visual field but consistent with the retinal image. The representation of the central visual field is located posteriorly close to the occipital pole, whereas the more peripheral regions are represented anteriorly (Wandell et al., 2009). Furthermore, a disproportionately large area of V1 is devoted to the representation of the central vision. This prominent bias toward the center of the gaze is called cortical magnification (Figure 2.2 a) which leads to higher visual acuity in the fovea, the central rod-free zone of the retina (Duncan and Boynton 2003; Hoffmann and Dumoulin 2015; Morland 2015). From V1 the information travels to area V2 which is in turn surrounded by V3. Unlike V1, these areas comprise discontinuous hemifield maps divided into two quarterfield maps, each of which is represented on the dorsal and ventral regions of V2 and V3 (Wandell et al., 2007). A collection of visual field maps has been identified beyond V3 in other extrastriate areas (see Figure 2.2 b). The multiplicity of these maps can be accounted for by functional specialization principle, meaning that specialized neuronal regions process different aspects of the visual input. For example, area V4 in the ventral stream is described as the color center while neurons in the middle temporal (MT) area, also known as V5, are motion-selective (Grill-Spector and Malach 2004). The link between certain perceptual deficits and localized brain damage confirms the functional specialization of the extrastriate areas. By contrast, lesions in early visual areas often lead to the general degradation of the vision in the corresponding regions of the visual field. This indicates that the different properties of the visual input are intermixed in these areas. Hence, the organization of the visual cortex incorporates a mixed model in which some cortical regions support a mixture of functions, whereas others are highly specialized (Wandell et al., 2009).

2.2   Congenital chiasmal abnormalities

The connections between the eyes and brain are largely altered in congenital chiasmal abnormalities. These conditions are associated with misrouting of the optic nerves at the
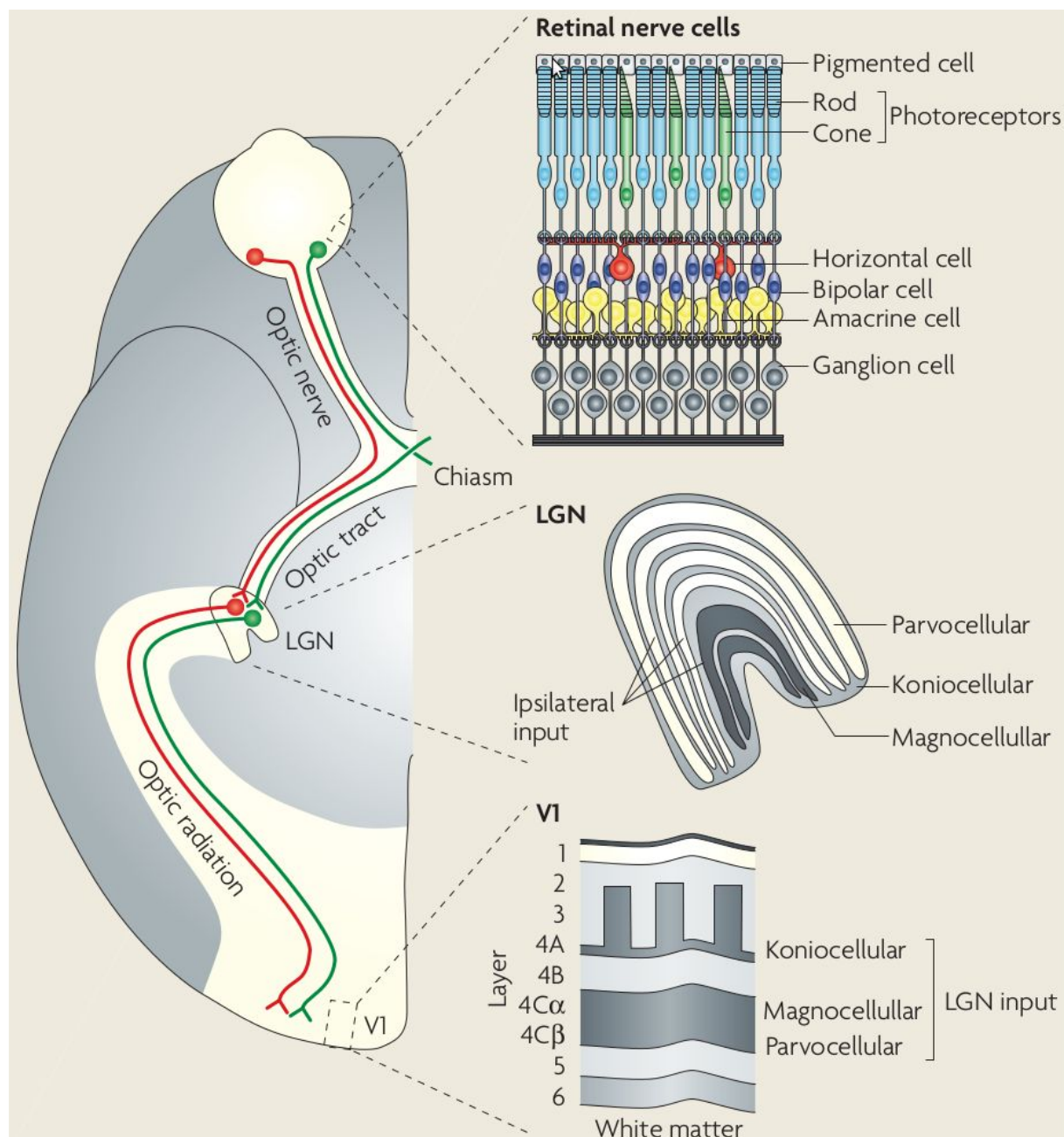
Figure 2.1: **Schematic representation of the neurotypical visual system from the eye to the visual cortex**. The LGN afferents terminate primarily in layer 4 of V1. The termination site in layer 4 depends on the layer to which the LGN neuron belongs: magno- and parvocellular neurons project mainly to layers 4Cα and 4Cβ respectively, while koniocellular neurons project to layer 4A and lower layer 3. The shading depicts the distinct pattern that emerges when slices through V1 are stained for cytochrome oxidase activity. Reprinted from (Solomon and Lennie 2007).

optic chiasm and are divided into two main categories: conditions with enhanced crossing of the temporal retinal afferents, as in albinism and FHONDA, as well as those with reduced or virtually absent crossing of the nasal fibers, as in achiasma, chiasma hypoplasia, and hemihydraencephaly . The following sections provide a detailed description of these conditions and their characteristics.
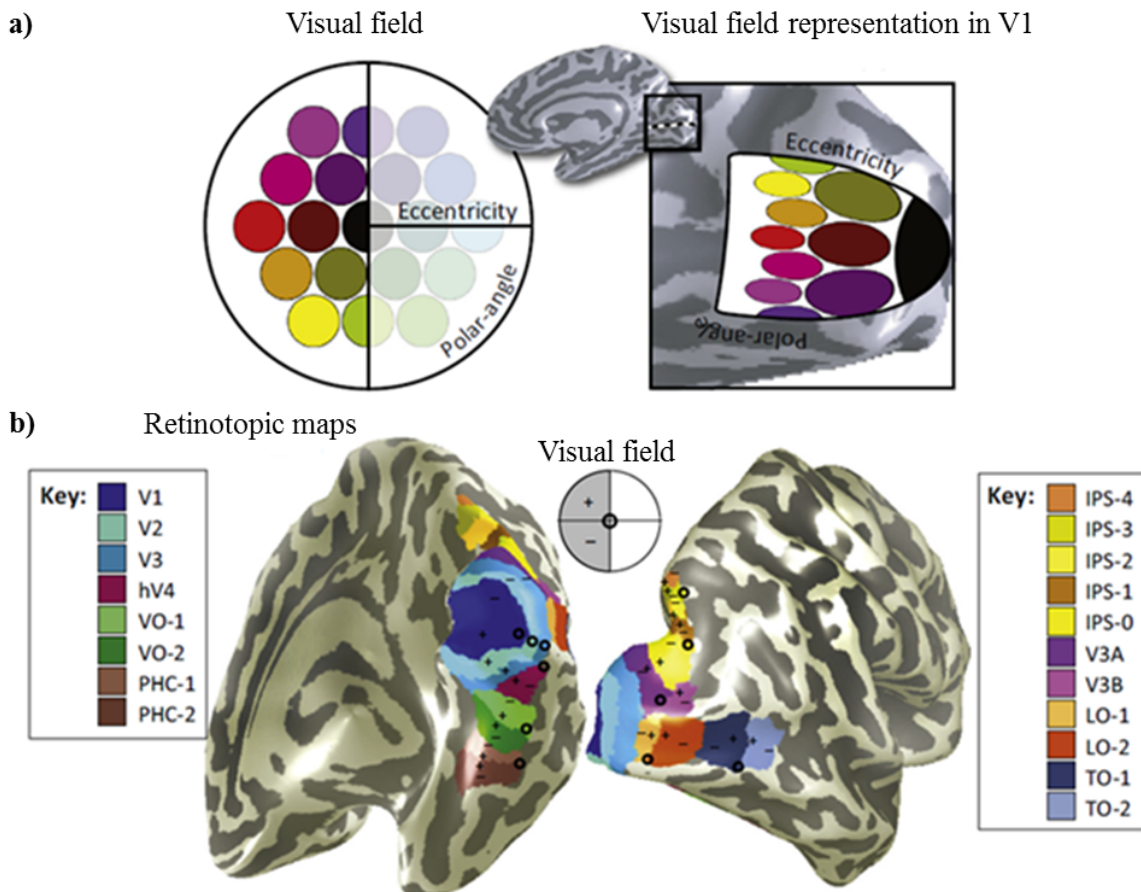
Figure 2.2: **Retinotopic maps on an inflated representation of a neurotypical hemisphere**. **a)** schematic representation of V1 illustrating image inversion and cortical magnification, **b)** schematic overview of retinotopic maps from a medial (left) & lateral (right) perspective. Foveal and upper/lower visual fields are indicated by "o","+","-" symbols. Reprinted from (Hoffmann and Dumoulin 2015).

2.2.1 Albinism and FHONDA

Albinism refers to a group of genetic mutations which lead to disrupted melanin synthesis. It is manifested by a hypopigmentation state affecting only the eyes (ocular albinism) or skin, hair and the eyes (oculocutaneous albinism). The prevalence of albinism varies across the world and has been estimated at approximately 1 in 17000 people (Grønskov et al., 2007). Common ocular symptoms include reduced visual acuity, foveal hypoplasia, nystagmus, strabismus, iris transillumination and absence of stereo vision (Oetting 1999).

In addition, albinism is associated with aberrant crossing of the temporal retinal fibers at the optic chiasm. The extent of misrouting is variable ranging between 2° - 15° (on average 8°; Hoffmann et al., 2005). Although this projection abnormality is an essential criterion in the diagnosis of albinism, it should not be considered as the pathognomonic sign. The enhanced crossing of the temporal fibers is also evident in FHONDA syndrome, a novel entity of congenital chiasmal abnormalities. Foveal hypoplasia, optic nerve decussation defects and anterior segment dysgenesis (FHONDA) is a rare disorder, attributed to a recessive mutation in the putative glutamine transporter gene SLC38A8 (Al-Araimi et al., 2013; Poulter et al., 2013). Currently, less than 20 identified cases have been reported in the literature. Despite the similarity of the symptoms in albinism and FHONDA, there is a fundamental difference between the two disorders. FHONDA is characterized by the absence of any pigmentation deficits, while albinism is per definition associated with hypopigmentation. This is of particular importance as the underlying mechanisms of misrouted optic nerves in albinism are linked to anomalies in melanin synthesis. Lack of pigmentation deficits in FHONDA indicates that similar projection errors can be induced by melanin-synthesis independent components.

2.2.2 Achiasma, chiasma hypoplasia and hemihydranencephaly

Achiasma, also known as non-decussating retinal-fugal fiber syndrome is characterized by congenital absence of the optic chiasm (Apkarian et al., 1995; Apkarian et al., 1994). As such, the nasal retinal fibers fail to cross and project entirely to the ipsilateral hemisphere. It is a rare disorder – with less than 50 published cases in the literature – associated with see-saw nystagmus, strabismus, reduced visual acuity, and absent stereo vision (Hoffmann and Dumoulin 2015). The underlying mechanisms of achiasma are not known in humans although a genetic cause is suggested from the reports in animal models (Seth et al., 2006). Chiasma hypoplasia is a similar condition identified by underdevelopment of the optic chiasm resulting in the reduced crossing of the nasal fibers. The major difference between the two disorders is the presence of residual contralateral projection in chiasma hypoplasia.

Hemihydranencephaly, on the other hand, is a very rare condition in which only one brain hemisphere is present. The unilateral hemispheric loss occurs during prenatal development, likely due to a vascular insult which prevents the normal formation of one hemisphere (Fracasso et al., 2016; Hoffmann and Dumoulin 2015; Muckli et al., 2009). Remarkably, the absence of a hemisphere often does not cause severe neurological impairments, allowing a relatively normal life (Pavone et al., 2013). The bilateral visual field is preserved, albeit restricted. This indicates a considerable reorganization of the visual pathways. Hemihydranencephaly thus resembles achiasma in the entire ipsilateral projection of the nasal fibers.

2.2.3 Visual field representations and visual perception in congenital chiasmal abnormalities

The misrouting of the optic nerves results in substantial deviation of the cortical visual field maps from those in controls (Figure 2.3). Opposing hemifields are not represented

on the opposite hemispheres rather as two overlaid representations on each hemisphere. As such, the same cortical regions are activated by the stimulation of both the contra- and the ipsilateral visual field indicating the stability of the geniculo-striate connections. The superimposed maps have been reported in all types of the congenital chiasmal abnormalities propagating from V1 to extrastriate areas (Ahmadi et al., 2019; Hoffmann et al., 2012, 2003; Kaule et al., 2014; Muckli et al., 2009). This suggests that similar mechanisms shape the organization of the visual cortex in different types of misrouting.

Despite the highly atypical visual field maps, the major aspects of the visual function are preserved in congenital chiasmal abnormalities. Qualitative observations demonstrate that affected individuals make effective use of their vision in daily activities. Furthermore, recent studies have provided a quantitative account of the intactness of the visual perception in albinism and achiasma indicating lack of crosstalk of the information between the ipsi- and contralateral visual fields (Eick et al., 2019; Klemen et al., 2012; Victor et al., 2000).
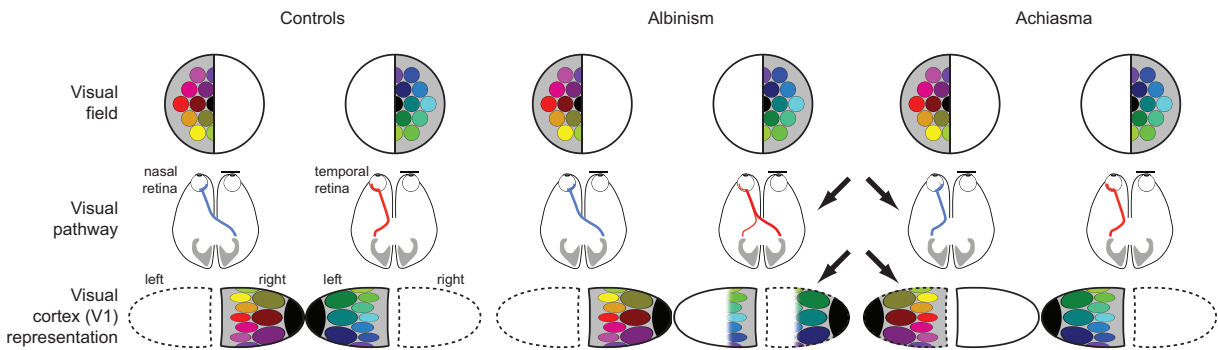
Figure 2.3: **Schematic of the visual pathways and V1 visual field maps in control, albinism and achiasma**. The top panel shows the left and right hemifields. The middle panel indicates the retino-geniculo-striate projections for the left eye. In controls, each of the temporal and nasal hemiretinae (red and blue, respectively) projects to the contralateral hemisphere. The misprojections in albinism and achiasma are shown by the black arrows. In albinism, a large part of the temporal retina projects contralaterally, leaving only a residual ipsilateral projection. In achiasma, all the nasal fibers project to the ipsilateral hemisphere. The bottom panel depicts the retinotopic maps on V1. While in control each hemifield is represented on the opposite hemisphere, in albinism and achiasma opposing hemifields are superimposed on the contra- and ipsilateral hemispheres, respectively. Reprinted from (Hoffmann and Dumoulin 2015).

2.2.4   Cortical organization schemes in congenital chiasmal abnormalities

Based on animal models, three cortical organization patterns have been proposed to accommodate the additional abnormal input from the ipsilateral visual hemifield. These models are termed 'contiguous representation', 'interleaved suppressed representation' and 'interleaved representation'. Contiguous representation requires a reordering of the geniculo-cortical connections leading to contiguous representations of the ipsi- and the

contralateral visual hemifields. This cortical scheme has been reported in albino Siamese cats (Hubel and Wiesel 1971) and ferrets (Huang and Guillery 1985). In interleaved suppressed representation pattern, the geniculo-striate connections are unaltered resulting in an interleaved representation of the opposing hemifields in V1. However, the abnormal input is suppressed which subsequently leads to hemianopia in the ipsilateral hemifield. The interleaved representation pattern is similar to the former scheme, except for lack of suppression of the abnormal ipsilateral input. While the contiguous representation and interleaved suppressed representation are available in many non-primate mammals, in humans and other primates only the interleaved representation has been reported (Guillery et al., 1984; Hoffmann and Dumoulin 2015; Hoffmann et al., 2003). This indicates a lack of sizable plasticity in the geniculo-striate projections and reflects the presence of hemifield dominance domains instead of ocular dominance domains (Guillery et al., 1984; Olman et al., 2016). To make the abnormal ipsilateral visual input available for perception, alterations of the intra-cortical mechanisms are required to selectively eliminate the integrative processes which would normally lead to binocular and stereo vision. As the integration of the inputs from opposing hemifield would result in major sensory conflicts. In conclusion, conservative i.e. unaltered, geniculo-cortical connections in combination with intra-cortical plasticity appear to be a general developmental mechanism in the human visual system.

Chapter 3

General methodology

Investigating the consequences of the transient and fundamental changes in the visual system can provide a wealth of information on the organization of the visual cortex and the scope of its plasticity. Nowadays, neuroimaging and electrophysiological experiments that last approximately less than an hour can be used to understand visual cortical responses in pathological states. The present chapter will focus on the main methodological and the analytical principles employed throughout this thesis.

3.1   Basic principles of magnetic resonance imaging

Magnetic resonance imaging (MRI) is an imaging modality commonly used in clinical practice and research. Using non-ionizing radiation, MRI generates soft tissue differentiation in multiple planes, providing a powerful tool in studying the brain and other organs of the human body. In principle, MRI utilizes the magnetic properties of hydrogen atoms in water and fat molecules. The positively charged nuclei of hydrogen spin around their axis. In the presence of an external magnetic field (B0), the magnetic moment of these nuclei aligns in the parallel or antiparallel direction to B0. The parallel orientation is preferred over the antiparallel state, leading to a net magnetization in the direction of B0. As such, the spinning positive charge of the hydrogen nuclei begins to rotate about the B0 axis. The frequency (ω) of this rotation, known as precession, is proportional to the strength of the magnetic field and is expressed by Larmor equation, where (γ) is a constant and stands for the gyromagnetic ratio.

$$\omega = \gamma B0 \tag{3.1}$$

Application of an electromagnetic pulse at Larmor frequency generates an oscillating electromagnetic field (B1) and provides sufficient energy to move a portion of protons in the antiparallel spin state to B0 and parallel to B1. Subsequently, the magnetization vector is flipped by a certain flip angle into the transverse plane. When the excitation pulse is switched off, these protons gradually return to the equilibrium state and the cycling vector approaches its original configuration in the longitudinal plane. This process is characterized by two relaxation times. T1 relaxation in which energy is transferred to

the surrounding lattice and T2 relaxation which refers to energy exchange between nuclei in high and low energy states. The difference in relaxation times between various tissues leads to the contrast observed in MRI images (Brown and Semelka 2003; Jezzard et al., 2002; McRobbie et al., 2007). During the relaxation process, the cycling magnetization vector induces a current in the receiver coil which is recorded and converted into an intensity signal. As protons give up their energy, they lose coherence which results in the reduction of the signal. The signal decays rapidly over time, in theory, on the rate of T2 relaxation, given by 1/T2. However, in practice, signal decay occurs faster due to inhomogeneities of the magnetic field. In order to take this effect into account, an effective transverse relaxation time ($T2^*$) is often stated. Thus, the amount of detectable signal is a function of $T2^*$. Spatial encoding in MRI has been made possible by the use of gradient coils which cause systematic changes in the magnetic field and lead to excitation and emission variations. Using a field gradient parallel to B0 for slice-selective excitation (z) and using a field gradient orthogonal to B0 for frequency encoding (x) and phase encoding (y), an image of a two-dimensional slice is measured in the so-called k space and reconstructed by the application of a two-dimensional Fourier transform. Finally, a three-dimensional image is obtained by making multiple slices for different values of z.

3.1.1   Functional magnetic resonance imaging

Functional magnetic resonance imaging (fMRI) is a versatile technique to study the functional organization of the brain, using hemodynamic signals (Bandettini et al., 1992; Ogawa et al., 1998; Ogawa et al., 1990) that are tightly connected to neuronal operations (Bandettini and Ungerleider 2001). The most common type of fMRI measures changes in blood oxygenation, induced by local brain activity. Due to task-dependent or spontaneous neuronal activity, the ratio of oxygenated haemoglobin to deoxygenated haemoglobin in the blood vessels increases after a few seconds with a characteristic profile, known as haemodynamic response function, HRF, (Heeger and Ress 2002; Logothetis and Wandell 2004). fMRI takes advantage of such Blood Oxygen Level Dependent (BOLD) activity. Oxygenated and deoxygenated haemoglobin have different magnetic properties. Oxyhaemoglobin is diamagnetic while deoxyhaemoglobin is paramagnetic. In the presence of the magnetic field, deoxyhaemoglobin becomes magnetized, resulting in inhomogeneities of the magnetic field and an initial reduction in signal intensity. Increased local activity is accompanied by a swift increase in Oxygen consumption, requiring an increase in cerebral blood flow (CBF). To accelerate oxygen delivery, the local supply of oxygenated blood increases much more, leading to a relative increase in the oxyhaemoglobin and subsequent decrease in the deoxyhaemoglobin, leading to fMRI signal gain(Birn et al., 1999).

Widespread use of fMRI is associated with its extensive availability, high spatial resolution, non-invasive nature and relatively easier analysis and interpretation compared to other techniques such as EEG or MEG. Nevertheless, fMRI has a few disadvantages that should be noted. It provides an indirect measure of neuronal activity, i.e. hemodynamic signals. Moreover, the relationship between the BOLD signal and hemodynamic responses has not been fully understood, which may influence the interpretation of the data. For instance, the signal might be obtained by synaptic activity rather than neuronal firing(Bandettini and Ungerleider 2001; Logothetis et al., 2001). Head movements,

respiratory and cardiovascular functions reduce the signal to noise ratio (Birn et al., 2008; Chang et al., 2009), which necessitates averaging and preprocessing to extract the fMRI signal. The last major drawback concerns the relatively low temporal resolution of fMRI due to hemodynamic response delay. Despite these limitations, fMRI has developed rapidly and gained popularity since its introduction in the early 90's.

Generally, most fMRI studies are performed using an Echo Planar Imaging (EPI) sequence (Glover 2011; Mansfield 1977), which can collect data at various resolutions with different repetition time (TR). Each voxel in the resulting scan generates a time series that is subsequently analyzed according to the task design. All the fMRI data discussed in the experimental chapters of this thesis have been acquired with EPI sequence using 3 or 7 Tesla scanners.

The application of fMRI in combination with recent developments in the computational approaches have led to remarkably extensive knowledge of the retinotopic organization of the visual cortex. In the following sections, three major analytical methods for mapping the visual areas and estimation of their functional connectivity are described.

3.2   Phase-encoded retinotopy

Phase-encoded retinotopy also known as traveling wave method is a technique to measure the representation of the visual field within human cortex which can objectively outline the borders of the visual areas (DeYoe et al., 1996; Engel et al., 1997; Sereno et al., 1995). A traveling wave of neuronal activity elicited by retinal stimulation is recorded with fMRI and analyzed by a Fourier based method. Eccentricity (distance from the center-of-gaze) and polar angle (angle from the center-of-gaze) constitute the two independent dimensions of retinotopy. A fundamental principle of the segregation of visual areas is that the boundaries are situated either at the cortical representations of horizontal or vertical meridian (DeYoe et al., 1996). In V1, upper and lower vertical meridians are represented on the lower and upper banks of the calcarine fissure, respectively. By contrast, the representation of the horizontal meridian is located at the depth of the calcarine. Reversing pattern of meridian representations continues beyond V1. At the V1/V2 border, the angular representations shift from vertical meridian to horizontal meridian forming dorsal and ventral V2, each of which representing only a quarter of the visual field (DeYoe et al., 1996; Engel et al., 1997; Wandell et al., 2009). V2 is surrounded by V3 map where the angular representations turn from horizontal meridian and progress dorsally toward the lower vertical meridian to form V3d and ventrally toward upper vertical meridian to create V3v. Similar to V2, each half of the V3 represents quadrant of the visual field. The same alternation of vertical and horizontal meridians occurs in other extrastriate areas as well.

Phase-encoded retinotopy employs two types of stimuli to elicit cortical responses. During one fMRI scan, participants view a contrast-reversing black-and-white checkerboard pattern comprising wedges that rotate (clockwise or counter-clockwise) around a central fixation point to map the angular direction stimulating each cortical location. In a second fMRI scan, a series of contrast reversing patterns in the form of expanding or contracting rings are presented to measure the eccentricity component of the map. Rotation

of the wedge stimuli leads to a traveling wave of activity moving between the representation of the upper and lower vertical meridian, while a set of rings of increasing size produce peak fMRI signals shifting smoothly from posterior to anterior regions. These stimuli often generate a BOLD signal modulation of 1 - 3% that is about 15 - 20 standard deviation above the background noise. The visual field representation of each voxel in the cortex is derived using the Fourier phase at the stimulus fundamental frequency measuring the relative delay of stimulus driven activity (Baseler et al., 2011; Engel et al., 1997; Wandell et al., 2007). Figure 3.1 shows exemplary traveling wave stimuli with color coded maps of eccentricity and polar angle on an inflated cortical surface.
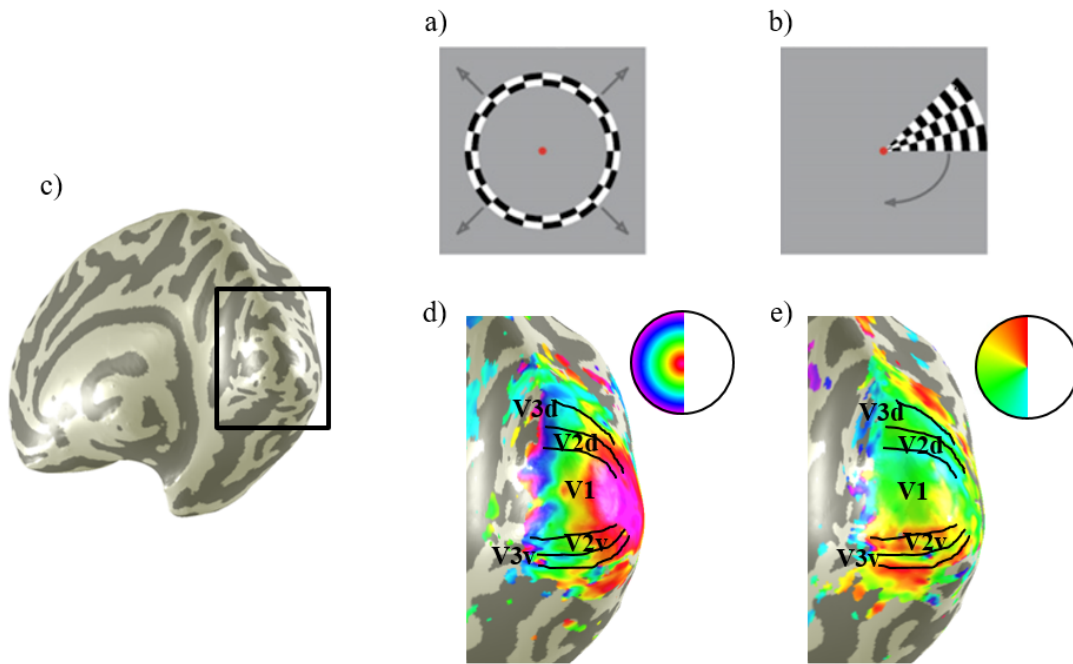
Figure 3.1: **Traveling wave measurements using ring & wedge stimuli**. An example of one stimulus frame from the **a)** expanding ring and **b)** rotating wedge is presented. The stimuli elicit strong neuronal responses in the **c)** occipital cortex shown by the large black square on an inflated brain hemisphere. Color coded maps of **d)** eccentricity and **e)** polar angle are overlaid on an expanded view of the cortical surface.

Despite the efficacy of phase-encoded retinotopy in identifying many visual field maps, particularly those with small receptive field, the method has significant limitations including uncertainty in defining foveal representation (Dumoulin and Wandell 2008; Schira et al., 2007; Tootell and Hadjikhani 2001; Wandell et al., 2007), nonlinear distortion of eccentricity estimates and difficulty in measuring maps with large receptive fields (Dumoulin and Wandell 2008; Wandell et al., 2007). To eliminate some of the intrinsic problems of this conventional approach, Dumoulin and Wandell developed a model-based method for estimating the neuronal population receptive field (Dumoulin and Wandell 2008) which will be described in detail in the next section.

3.3 Population receptive field modeling

Receptive field modeling is an important tool to predict the neural responses based on stimulus properties. It is also known as population receptive field (pRF) modeling due to measuring the pooled responses of many neurons (Wandell and Winawer 2015). The term receptive field was first coined by Sherrington to describe the region of skin surface eliciting scratch reflex (Sherrington 1910) and later was applied to visual neurons (Hartline 1938). The concept is defined as the region of visual space stimulating the recording site (Dumoulin and Wandell 2008; Victor et al., 1994; Winawer et al., 2010). The pRF model can be implemented in neuroimaging and electrophysiological modalities including fMRI, EEG and microelectrode measurements (Dumoulin and Wandell 2008; Victor et al., 1994).

The use of fMRI-based population receptive field modeling has gained increasing popularity over the last decade. This method which was introduced by Dumoulin and Wandell (Dumoulin and Wandell 2008) builds on conventional phase-encoded retinotopy and computes a model of population receptive field from responses to multiple types of stimuli. Furthermore, the model reconstructs the cortical visual field maps more accurately and provides novel estimates of neuronal population properties, such as the receptive field size and its ipsilateral extent (laterality). While the conventional approaches use the phase of fMRI time-series modulation to find the most effective visual field locations that derive a neural response, pRF model employs the temporal responses to a wide range of stimuli including rings, wedges and drifting bar apertures at various orientations for estimation of pRF properties. Hence, the pRF model extracts the information from the fMRI signal that is missed by the conventional methods.

Measuring visual field maps with large receptive fields is one of the major restrictions of the phase-encoded retinotopy, because large receptive fields are poorly analyzed by conventional ring and wedge stimuli. Modifying the stimulus sequence by incorporating mean luminance blocks (zero contrast) which replace different wedge and ring positions provides a baseline condition to distinguish differences in pRF size.

The pRF parameters are estimated from the fMRI data using a linear spatio-temporal model. Considering a linear relationship between the blood oxygenation level and the fMRI signal, the observed response y(t) can be described by the following formula in which p(t) is the predicted BOLD signal, β is the scaling factor accounting for the unknown units of the signal and e stands for the noise.

$$y(t) = p(t)\beta + e \tag{3.2}$$

For each voxel, the predicted BOLD signal is calculated using a two-dimensional (2D), circularly symmetric Gaussian pRF model defined by three parameters, i.e. the center location (x_0 and y_0) and spread σ (standard deviation).

$$g(x, y) = exp - ((x - x_0)^2 + (y - y_0)^2 / 2\sigma^2) \tag{3.3}$$

The parameters are stimulus-referred and expressed in degrees of visual angle. Afterwards, the predicted BOLD signal is obtained by convolution of the modeled pRF, the stimulus sequence and a canonical BOLD hemodynamic response function (HRF) (Boynton et al., 1996; Friston et al., 1998; Worsley et al., 2002). The pRF parameters for each voxel are

determined by minimizing the residual sum of squares (RSS) between the predicted and
observed fMRI BOLD responses (Harvey and Dumoulin 2011) using a two stage coarse-
to-fine search. In the first stage, the fMRI data is smoothed with a Gaussian kernel with
full-width at half-maximum (FWHM) of 5 mm along the cortical surface. Next, 100,000
different fMRI time series predictions are generated by varying x_0, y_0 and σ parameters
across range of values on a sampling grid. Subsequently, an optimization algorithm is
applied (Fletcher and Powell 1963) to voxels whose first stage estimates explained more
than 15% of the variance of the fMRI signal. It should be noted that no further smoothing
is performed in this stage. The goodness of fit is specified by percent variance explained
rather than the t- and p-values due to their bias toward the larger values (Dumoulin and
Wandell 2008). Polar Angle ($atan(y/x)$), eccentricity ($sqrt(x^2 + y^2)$) and pRF size (σ)
are derived from the the fitted 2D Gaussian model (Amano et al., 2009; Winawer et al.,
2010). There is a progressive increase in the pRF size from the low to high level areas
of the visual cortical hierarchy. Further, pRF size increases as a function of eccentricity
within each area (Amano et al., 2009; Dumoulin and Wandell 2008; Harvey and Dumoulin
2011; Wandell and Winawer 2015; Winawer et al., 2010). Figure 3.2 depicts the pRF size
estimates of areas V1-V4 on an inflated cortical surface as well as its relationship with
eccentricity.
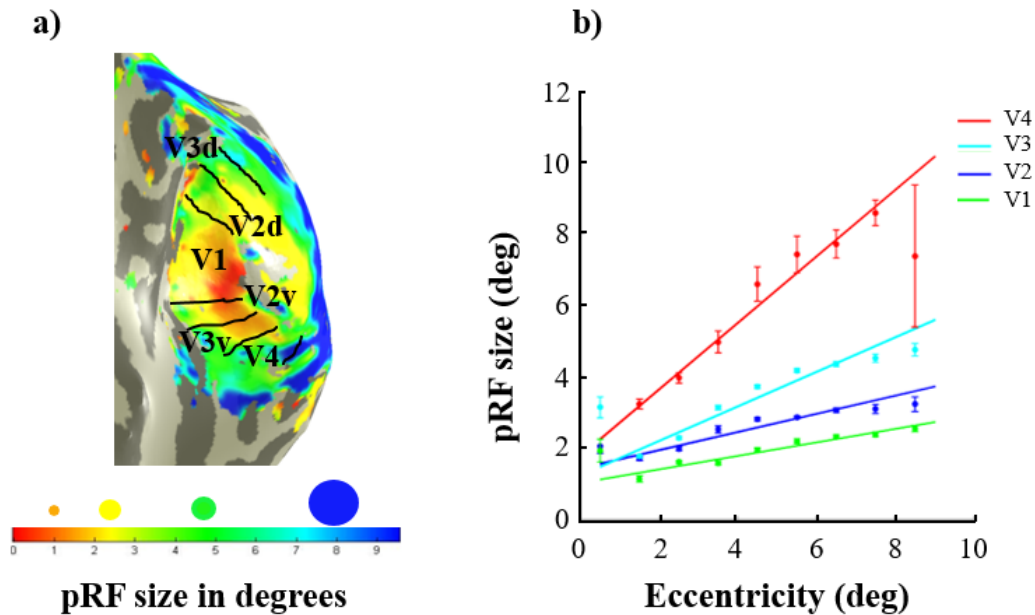
Figure 3.2: **Changes of pRF size in areas V1-V4**. **a)** The pRF size map is displayed on
an enlarged part of the occipital lobe. The colors indicate different pRF sizes as shown on the
color bar. **b)** The pRF size increases systematically from V1 to V4. In addition, Within each
area, pRF size increases linearly with eccentricity. The solid lines represent the fit to the data
(circles) and error bars show one standard error of the mean.

Similar to its size, the pRF laterality varies across the visual areas. For instance, the

pRFs in V1 are mainly confined to the contralateral visual field, while the pRF coverage in the temporal-occipital regions (TO1 and TO2) is much wider and extends significantly to the ipsilateral hemifield, reflecting their larger receptive field size (Amano et al., 2009). By combining the pRF centers and sizes across a collection of voxels within each area, the visual field coverage (visual field locations evoking a significant response in those voxels) can be visualized (Amano et al., 2009; Mackey et al., 2017; Wandell and Winawer 2015; Winawer et al., 2010). For this purpose, the pRF centers in each region are first identified. Afterwards, a binary image is created which indicates the presence of the pRF centers at each visual field location. Next, the visual field coverage is estimated by combining the pRF center and size parameters. Since many points in the visual field are covered by at least one pRF, a map representing the highest pRF value at each visual field location is created (Amano et al., 2009). In order to decrease the effect of outliers, all pRFs within each area are sampled randomly with replacement. By bootstrapping with 100 replicates, 100 coverage maps are generated and the mean of them is taken as the final coverage map. Moreover, the influence of atypically large receptive field sizes is minimized by smoothing with a median filter, meaning that for each voxel in an area, two other voxels with the closest pRF centers (two nearest neighbours in the visual field) are determined and that voxel's size parameter is replaced with the median of the three voxels' pRF sizes (Winawer et al., 2010). The range of the values of the coverage map is between 0 and 1 because the peak value of the (2D) Gaussian model is normalized to 1 (Amano et al., 2009; Winawer et al., 2010). Figure 3.3 compares the visual field coverage maps in left V1, V3d and lateral-occipital area 1 (LO1). The modest extension of the coverage map to the ipsilateral hemifield in V1 and V3d can be explained by the use of a circularly symmetric Gaussian model for the pRF which might be diminished by applying asymmetric models.
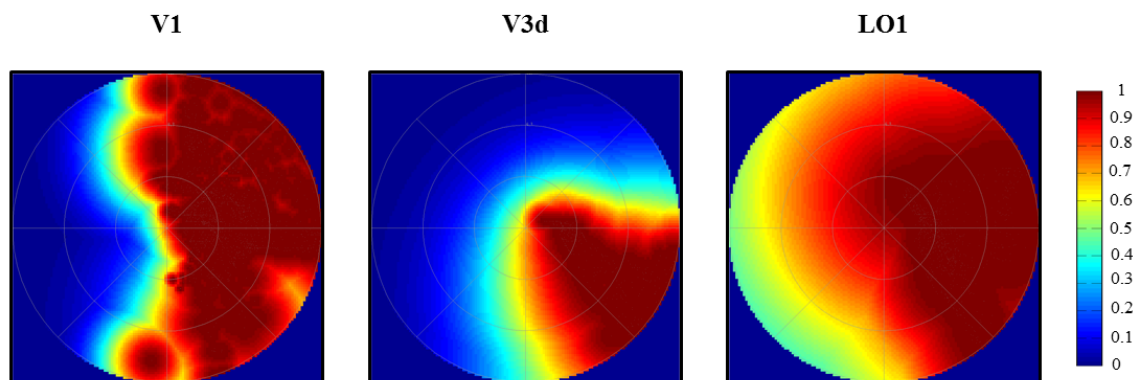
Figure 3.3: **Visual field coverage maps**. The data is plotted from the left hemisphere of one of the study participants. The V1 and V3d coverage is largely confined to the contralateral hemifield and contralateral lower quadrant. In contrast, the pRFs in LO1 span the entire contralateral visual field and overlap substantially into the ipsilateral hemifield.

The pRF modeling has provided a quantitative framework to characterize the scope of cortical plasticity and underlying neural circuitry in a variety of retinal, neurological and psychiatric disorders (Anderson et al., 2017; Baseler et al., 2011; Brewer and Barton

2014; Hoffmann et al., 2012; Levin et al., 2010; Schwarzkopf et al., 2014). The model can be adapted to measure tonotopic, somatotopic and numerosity maps in auditory, somatosensory and the association cortices (Harvey et al., 2013; Thomas et al., 2015). Further, the spatially localized pattern of functional connectivity between different visual areas can be studied through a complementary parameterized method that builds on the pRF modeling, and will be discussed below.

3.4 Connective field modeling

Understanding the cortico-cortical interactions between distinct regions of the visual cortex is essential to study the intrinsic properties of the visual information transmission. Connective field (CF) modeling developed by Haak et al., (Haak et al., 2013) constitutes an important milestone to measure the fine-grained topographic connectivity between visual areas. It predicts the neural activity in a voxel within a target region of interest (ROI) in terms of the aggregate activity in another region of the brain. Using fMRI, CF modeling expands the concept of receptive field from prefered stimulus positions to preferred cortical locations (Gravel et al., 2014). Similar to pRF modeling, the CF parameters are estimated from the fMRI time-series using a linear spatio-temporal model (see equation 3.1). The predicted fMRI signal is calculated by use of a two-dimensional (2D) isotropic Gaussian CF model that follows the cortical curvature. The CF model is defined by two parameters shown in the following formula

$$g(v) = exp - [d(v, v_0)^2 / 2\sigma^2] \tag{3.4}$$

where v_0 represents the center location in the voxel coordinates, σ stands for the Gaussian width in millimeter across the cortical surface and $d(v, v_0)$ is the shortest distance between a given voxel, v, and v_0 computed by Dijkstra algorithm (Dijkstra 1959) on a three-dimensional (3D) mesh representation of the gray/white matter boundary. The predicted fMRI signal is then obtained by calculating the overlap between the connective field and the weighted sum of the signals in the source region with no further convolution with the hemodynamic response function. Ultimately, the optimal connective field parameters are found by minimizing the residual sum of squares (RSS) between the predicted and the observed fMRI time-series. To this end, many fMRI time-series predictions are made by altering the connective field parameters i.e. center, v_0, and size, σ, across all voxel in the source region. In analogy to pRF modeling, the percent variance explained is used as a measure of goodness of fit.

Comparison of the CF and pRF model fits demonstrates the superiority of the CF modeling in explaining the variance of the time series (Figure 3.4). Specifically, the CF model can capture some of the BOLD co-fluctuations in the absence of visual stimuli during the mean luminance blocks.

Furthermore, visual field maps of the target region can be reconstructed once the CF estimates are known. As such, CF model links the voxels which have overlapping receptive fields and consequently similar time series. Figure 3.5a shows both pRF and CF derived eccentricity and polar angle maps for areas V1 - V3 in a single participant.
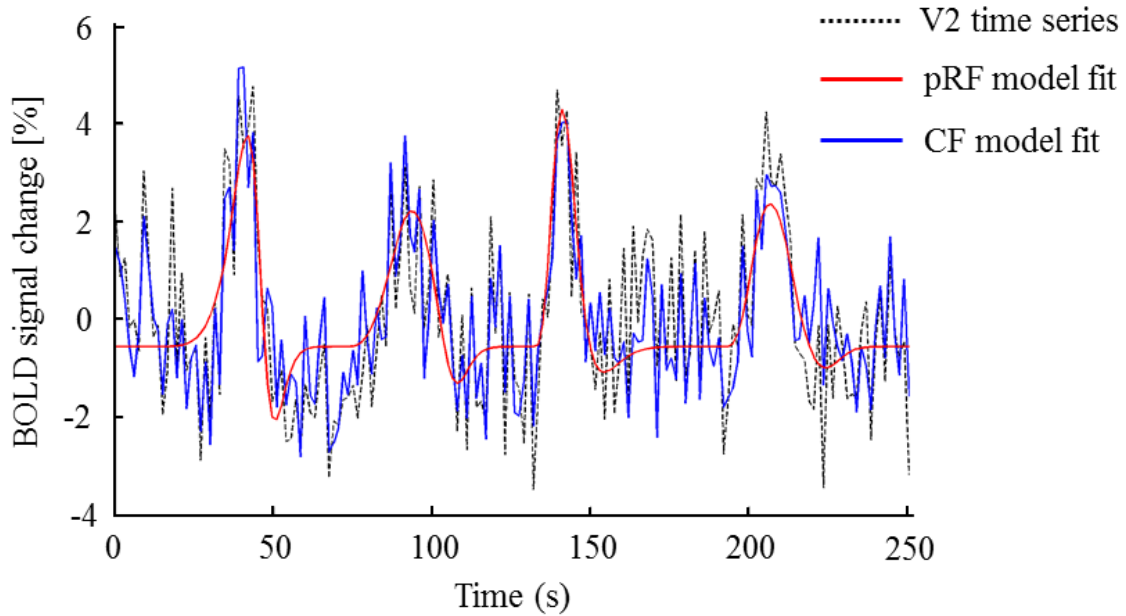
Figure 3.4: **Comparison of the pRF and CF model fits to the fMRI time series in a given voxel in V2**. The time series are shown by the dotted black lines. The pRF and CF model fits are indicated by the solid red and blue lines, respectively. The CF model outperforms the pRF model by explaining 74.25% vs 45.47% of the time series variance. Note that unlike the pRF model, CF modeling can predict the time series alterations when no stimulus is presented.

Qualitatively, there is a remarkably good agreement between the pRF- and CF-based maps. Quantitatively, this agreement is verified by a correlation analysis indicating that the derived maps are significantly correlated (r= 0.91, r= 0.75 for eccentricity and r= 0.91, r= 0.96; $p \leq 0.001$ for polar angle maps in V2 and V3 respectively).

Previous reports have shown constant sampling size and subsequently no further magnification in the pooling of signal from V1 to higher areas (Harvey and Dumoulin 2011; Schwarzkopf et al., 2011). Thus, it is expected that the connective field sizes of V1 to extrastriate areas stay steady across eccentricity. However, the connective field size of a voxel not only depends on the position of that voxel in the eccentricity map, but also on the extent to which its pRF overlaps with the ipsilateral visual hemifield (pRF laterality). Adjusting the connective field size for pRF laterality, yields V1 sampling extent which is relatively constant across eccentricity but increases through visual hierarchy (Figure 3.5 b).

Taken together, CF modeling benefits from the wide field of view in fMRI to investigate the large-scale neuronal communications between brain regions. Although other approaches such as seed-to-voxel connectivity mapping (Biswal et al., 1997; Biswal et al., 1995; Vincent et al., 2008) and independent component analysis (Beckmann et al., 2005; Calhoun et al., 2001) have been used frequently to measure functionally linked cortical networks, biologically inspired methods like CF modeling provide an alternative approach to improve the correlational-causal methodology exploited by the former tech-
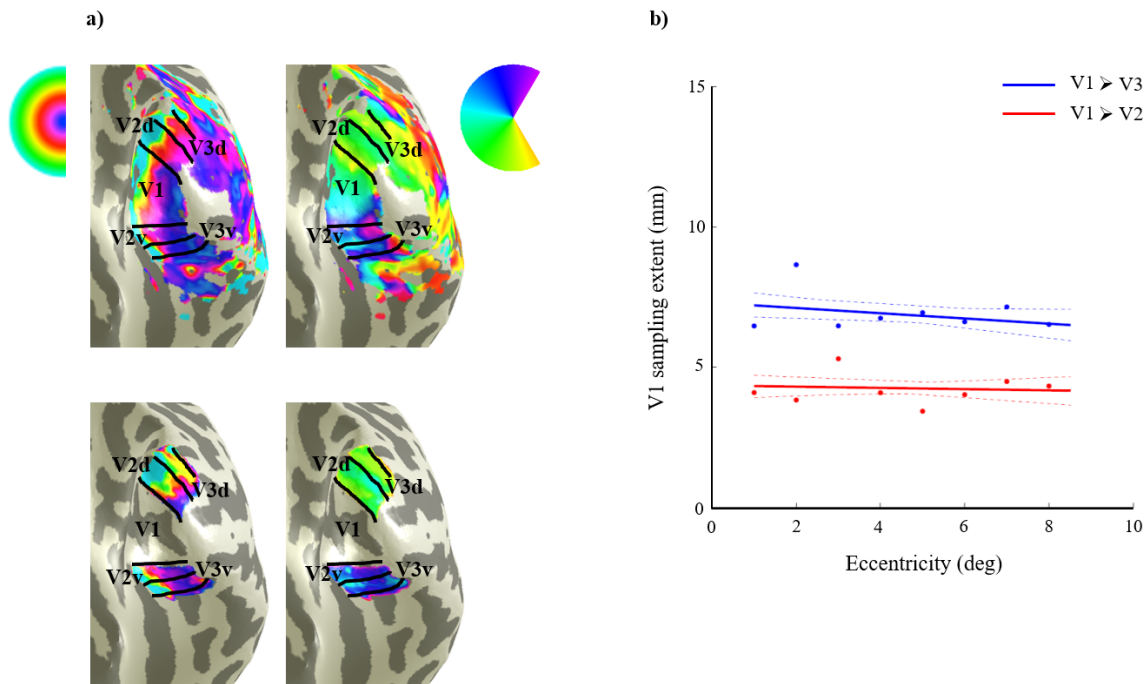
Figure 3.5: **Comparison of the pRF and CF derived map along with V1-referred CF size and eccentricity relationship**. **a)** Eccentricity and polar angle maps overlaid on the inflated surface of the right hemisphere in a single subject. The top panel depicts the visual field map estimates based on pRF modeling while the bottom panel shows the derivative maps from CF modeling. **b)** The V1-referred CF size increases substantially across the visual areas but not with eccentricity. The solid lines represent the fit to the data (bins) and the dashed gray lines indicate the 95% bootstrap confidence interval of the linear fit.

niques (Wandell and Winawer 2015). Moreover, given the dependence of CF modeling on neural-referred properties rather than stimulus-referred attributes, it can be applied to both visual field mapping and resting state fMRI to explore the connectivity profiles.

In summary, over the past three decades, phenomenal opportunities presented by fMRI in conjunction with promising analytic methods have revealed new fundamental insights in the organization of the human visual cortex. This progress will continue to provide more precise information about the major visual functions including development, plasticity and perception. The next sections will focus on the electrophysiological and ophthalmological tools used to confirm misrouting of the optic nerves and to assess the extent of ocular symptoms in congenital chiasmal abnormalities.

3.5 Event-related potentials

Event-related potentials (ERPs) reflect the postsynaptic potentials that are evoked by sensory stimuli and recorded by placing electrodes over the scalp (Luck 2005). ERP studies provide a quantitative functional assessment of the sensory pathways from the sensory organ to the cerebral cortex. Three widespread types of ERPs comprise visual evoked

potentials (VEPs), auditory evoked potentials (AEP) and somatosensory evoked potentials (SSEPs). The first technique has been applied in this thesis and will be discussed in detail in the following section.

3.5.1   Visual evoked potential

The visual evoked potential (VEP) is a measurement of the electrical signal recorded mainly from the visual cortex in response to visual stimulation. It was introduced in the 1930s (Adrian and Matthews 1934) and since then has substantially evolved (Heckenlively et al., 2006). VEP can provide crucial information on the functional integrity of the visual system (Odom et al., 2010) and has been used in the diagnosis of various neuro-ophthalmological diseases particularly, congenital chiasmal abnormalities (Apkarian et al., 1994, 1983; Creel 1979; Hoffmann et al., 2005; van Genderen et al., 2006).

The recording is typically performed with monocular stimulation and silver chloride or gold disc electrodes placed over the scalp according to the 10-20 international system (Jasper 1958). The active electrode (Oz) is located along the midline over the occipital cortex and the reference electrode (Fz) is placed over the frontal cortex. A third electrode should be connected to the ground and attached to an irrelevant point. Common positions of the ground electrode include the forehead, vertex (Cz), mastoid, earlobe (A1 or A2) or linked earlobes.

Among the several types of visual stimuli that are available to generate VEPs, the pattern onset/offset stimuli are best suited for individuals with fixation instabilities (Hoffmann et al., 2004) such as those affected with congenital chiasmal abnormalities. In this type of stimulation, the checkerboard pattern is suddenly switched with a diffuse gray background. The duration of the pattern stimuli is usually 200 ms followed by 400 ms of diffuse background. The mean luminance of these two phases should remain identical with no change of luminance during the transition (Heckenlively et al., 2006; Odom et al., 2010).

The VEP waveform is characterized by its amplitude and timing latency. The amplitude is related to the number of afferent neurons reaching the cortex and the latency refers to the time from stimulus onset to the largest amplitude of a positive or negative component (Odom et al., 2010). The pattern onset/offset VEP waveform is a triphasic consisting of a positive peak at approximately 75 ms (C1) followed by a negative peak at around 125 ms (C2) and another positive peak at 150 ms (C3).

In a normal visual system, monocular stimulation of the visual field results in VEPs in both hemispheres. In congenital chiasmal abnormalities, however, it elicits greater VEPs either on the hemisphere contralateral or ipsilateral to the stimulated eye respectively. Therefore, the use of three active electrodes (O1, O2, Oz) referenced to Fz is recommended to increase the sensitivity to these lateral asymmetries (Odom et al., 2010).

In these conditions, the polarity of the interhemispheric difference is inverted for left compared to right eye stimulation while it does not depend on the stimulated eye in controls (see Figure 3.6; Hoffmann and Dumoulin 2015; Hoffmann et al., 2005, 2006). Supplementing this paradigm with a correlation analysis improves its objectivity. Due to polarity inversion of the traces, the interhemispheric activation differences obtained

by stimulation of the left and right eye are negatively correlated in congenital chiasmal malformations. In contrast, the absence of such polarity inversion in controls leads to a positive correlation (Hoffmann et al., 2011).
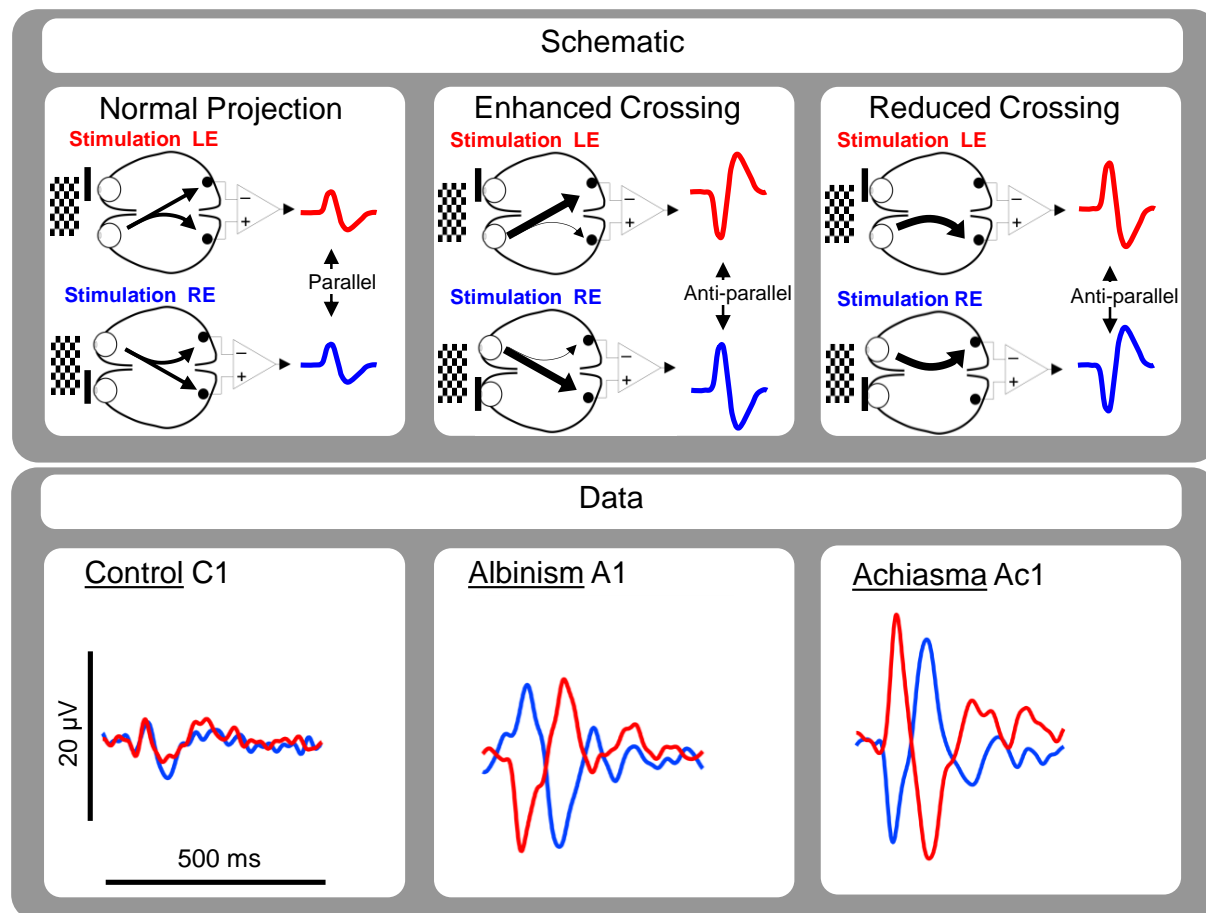
Figure 3.6: **Misrouting VEP paradigm**. Upon left or right eye stimulation interhemispheric VEP differences are determined (schematically depicted by differential amplifier symbol). While the difference traces for stimulation of both eyes are similar in controls, they are inverted in their polarity in albinism and achiasma. The two conditions can be differentiated based on predominant VEP lateralization on the hemisphere contralateral and ipsilateral to the stimulated eye, respectively. Right panels: Examples of interhemispheric activation differences. Upon stimulation of either eye, parallel difference traces are observed for a control (C1) and anti-parallel traces for albinotic (A1) and achiasmatic individuals (Ac1). Adapted from (Hoffmann and Dumoulin 2015).

3.6   Microperimetry

Microperimetry (MP) also known as fundus-related perimetry is a technique to examine retinal fixation, foveal or parafoveal and macular sensitivity (Midena et al., 2004). It allows obtaining an exact correlation between the fundus lesions and functional defects

(Hanout et al., 2015; Midena et al., 2004, 2007; Rohrschneider et al., 2008) and has
been employed in various ocular diseases to measure the effects of the disease and the
therapeutic responses (Arrico et al., 2016; Chen et al., 2009; Grenga et al., 2008; Midena
et al., 2007; Radtke et al., 2008; Vujosevic et al., 2006). Furthermore, microperimetry
incorporates an eye tracker that compensates for eye movements in real time, which not
only detects the fixation loss but also corrects it automatically and provides a good match
between the anticipated position of the stimulus on the retina and the actual projection
position (Midena et al., 2004; Molina-Martin et al., 2015). In this thesis, the Nidek MP-
1 microperimeter (Nidek Technologies, Padova, Italy) was used in 5 out of 6 albinotic
participants to assess the fixation instability. The fundus was imaged by an infrared
camera with a 45° field of view and resolution of 768 x 576 pixels. The fixation target
and stimuli were projected onto the participant retina through a liquid crystal display
(LCD) controlled by NAVIS software. The examiner could view the image of the retina
on another monitor with the stimuli as part of it. Background luminance was set at
$1.27 \, \text{cd m}^{-2}$. Goldmann III stimuli and a 4-2 double staircase strategy were used. The
grid pattern consisted of 33 stimuli (11° x 11°) with intensity values ranging from 0 to
20 in 1 dB (0.1 log) steps. The eye tracker monitored the eye position during stimulus
presentation with the frequency of 25 Hz every 40 ms. Figure 3.7 illustrates unstable
fixation patterns in albinotic and achiasmatic subjects compared to a stable pattern in a
normally sighted individual.
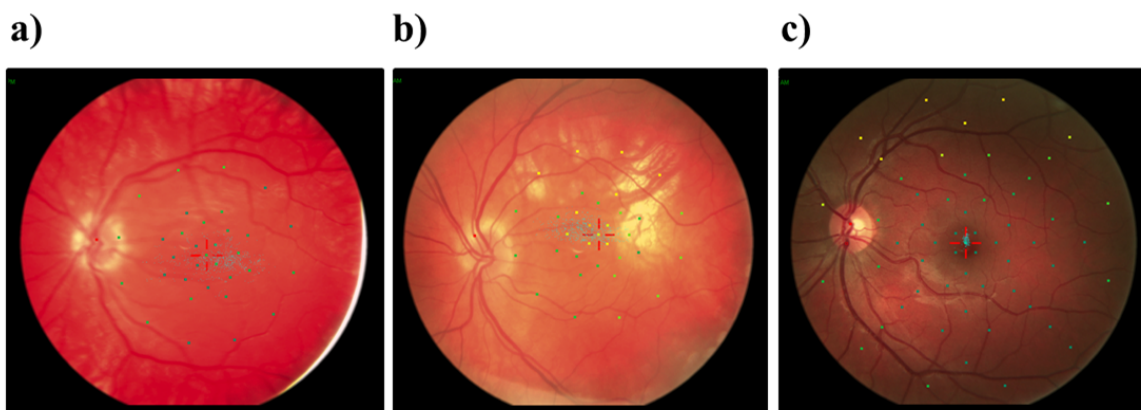
Figure 3.7: **Microperimetric image of the left eye in a) albinism, b) achiasma and
c) control**. Retinal fixation is represented by tiny confluent points revealing an eccentric and
unstable pattern in albinism and achiasma.

3.7   Freiburg Visual Acuity Test

The Freiburg Visual Acuity and Contrast Test (FrACT), (Bach 1996), is a widely used,
freely available and automated visual test battery that can be run on Macintosh, Linux or
Windows operating systems (Bach 2006; http://www.michaelbach.de/fract.html). Lan-
dolt C optotypes in various sizes and eight different orientations are presented on a monitor

to the subject. The examiner records the subject's response on the perceived direction of the C's opening by pressing one of the 8 buttons on the keyboard. Acoustic feedback is given to the correct and wrong replies in the form of two different tones emitted by a loudspeaker. Acuity threshold is estimated using best PEST (Parameter Estimation by Sequential Testing) algorithm based on signal detection theory (Lieberman and Pentland 1982). The algorithm operates on a logarithmic scale and brackets the threshold initially in big but afterwards in smaller steps. The size of the next presented optotype follows an adaptive staircase procedure determined by best PEST on the basis of all previous answers (Bach 1996; Bach and Schäfer 2016; Schulze-Bonsel et al., 2006).

Pixel-discreteness artefacts can limit the presentation of very small stimuli. Through smoothing of the counters by multiple gray levels i.e. anti-aliasing, FrACT improves the spatial resolution by a factor of four (Bach 1997). In this thesis, all the control participants of the studies undertaken in Magdeburg took part in visual acuity assessment using FrACT. The eyes were measured twice at a distance of 5 meters in a counter-balanced mode by the author. Each run comprised of 24 trials. Given the reduced visual acuity, nystagmus and fixation instabilities in albinism and chiasma hypoplasia, visual acuity in these subjects was assessed by a professional optometrist using a different program.

3.8 Stereovision Tests

The individual with chiasma hypoplasia, albinotic and control participants of the studies reported in chapters 7 and 8 were tested with commonly used Lang I, Titmus and TNO stereovision tests that are described in more details below.

The Lang I test (LANG-STEREOTEST AG, Küsnacht, Switzerland) developed by Swiss ophthalmologist, Joseph Lang, in the early 80's is based on principles of random dots and cylinder gratings. The test is performed at a distance of 40 cm. No polarized glasses or red-green filters are required during the examination. A cat, a star and a car is displayed on a card measuring 9.5 cm x 14.5 cm representing retinal disparity of 1200, 600 and 550 seconds of arc (Ancona et al., 2014; Brown et al., 2001; Lang 1983). Failure in the detection of the above-mentioned objects can indicate lack of stereopsis.

The Titmus test (Stereo Optical, Chicago, IL, USA) uses black contoured stimuli. Polarized glasses separate the stimuli presented to each eye. The test consists of three parts. The first component is a fly subtending to 3000 seconds of arc. The subject is required to grab its wings if they appear above the page. The second part comprises circles clustered in 9 groups of four contour circles representing disparity of 800, 400, 200,140,100, 80, 60, 50, 40 seconds of arc. The subject is asked to find the circle which pops up above the level of others. The third component contains three lines of five animals with disparity ranging from 400 to 100 seconds of arc. Here, the task of the subject is to identify the animal which appears to jump off the page (Leske and Holmes 2004).

The TNO test (Lameris Instrumenten, Groenekan, the Netherlands) is based on random dot technique as Lang I test. It consists of 7 plates to be viewed with red-green filters, each of which representing hidden objects that can be seen only when both eyes

are used. The first plate displays two butterflies, one of which is hidden. In the second plate, four discs of which only two can be seen stereoscopically are presented. Plate III shows four hidden geometric shapes. The subject is asked to point the invisible items out if s/he can see them. Following this screening phase, stereoscopic sensitivity measures may be obtained using plates V-VII. In these plates, discs with missing sectors are shown at six different depth levels. The corresponding disparities range from 15-480 seconds of arc. Participants are required to point to the missing part of the discs. Unsuccessful attempts can demonstrate stereo-blindness (Vancleef et al., 2017).

Chapter 4

Research questions

The overarching aim of the present thesis is to relate visual function and perception in disease to cortical activation patterns to uncover the interplay of pathophysiological and plastic mechanisms. For this purpose, two different types of disorders are investigated. First, short-term visual anomalies are assessed in migraine to shed light on the underlying pathophysiology of migraine aura. Subsequently, the consequences of the congenital chiasmal malformations on the visual system are studied in detail to enhance our knowledge of the plastic mechanisms that influence the architecture of the visual cortex. Using the techniques and the analytical methods described in chapter 3, the following questions will be addressed in the next chapters.

1. What are the cortical changes associated with migraine aura?

   - Can the positive and negative aura symptoms be differentiated by corresponding BOLD signal changes?
   - How do the bilateral aura symptoms affect the BOLD signal?

   Thorough answers to the above questions are provided in chapter 5. Five migraineurs with aura were investigated using fMRI in two different sessions. In the first session, they were scanned during the aura attacks while in the second session retinotopic mapping was performed to delineate the visual areas. The data were acquired at the Danish Headache Center in Copenhagen and were analyzed by the author of the present thesis. Due to the highly challenging task of capturing patients during aura inside the MRI scanner, there has been only one previous study reporting BOLD response changes in migraine aura (Hadjikhani et al., 2001), whose results were not yet replicated. In this study, we measured the BOLD modulation in areas V1 to V4 and its relationship with clinically heterogeneous aura symptoms.

2. How are the early visual areas organized in FHONDA?

   - Is the conventional, commonly-used pRF model adequate for characterization of the pRF properties in FHONDA?
   - Do the neural populations have bilateral receptive fields in FHONDA?

- Does the relationship between the pRF size vs eccentricity in FHONDA follow the known pattern in controls?

- Is there a relationship between the mechanisms shaping the organization of the visual cortex in FHONDA and other congenital chiasmal abnormalities?

Detailed answers to these questions are given in chapter 6. FHONDA is a novel entity of the congenital chiasmal abnormalities (Al-Araimi et al., 2013; Poulter et al., 2013), sharing similar symptoms with albinism in the absence of hypopigmentation. In collaboration with Utrecht University, two individuals with FHONDA were studied using ultra-high field fMRI at 7 T. The data were acquired in Utrecht and analyzed by the author of the current thesis. By modeling the pRF properties of the early visual areas, we provide the first evidence on the nature of the cortical organization in this new inherited disorder.

3. Can the visual cortex accommodate more than 2 superimposed maps?

- What kind of projection errors at the optic chiasm results in a third, i.e. extra, input to the visual cortex?

- How are the retinotopic maps organized in the presence of a third input?

- How is the cortical fine-grain structure in the presence of a third input?

These questions are addressed in chapter 7. In a collaborative project, we determined the cortical organization in a rare individual with chiasma hypoplasia, where visual cortex plasticity is challenged to host three hemifield maps. To investigate the mechanisms that incorporate the extra input, the projection errors and the cortical fine-grain structure were assessed using DWI and ultra-high resolution fMRI in Magdeburg. Furthermore, the layout of the visual field maps was determined using pRF mapping data acquired at the University of York. Besides the analysis of the fMRI data, the author of this thesis was also involved in the data acquisition. We demonstrate the first in vivo evidence on the previously unknown extensive scope of the cortical plasticity.

4. What is the detailed organization of the visual cortex in albinism?

- Is the conventional, commonly-used pRF model adequate for characterization of the pRF properties in a cortical region receiving abnormal input from the temporal retina?

- Is the conventional, commonly-used pRF model adequate for characterization of the pRF properties in a cortical region receiving residual normal ipsilateral input from the temporal retina?

- Is there a difference in the size of pRFs stimulated by the left visual hemifield and pRFs derived by the right visual hemifield in albinism?

- Is V1-sampling extent in V2 and V3 of the albinotic individuals similar to the corresponding V1-sampling extents in controls?

These questions are answered in chapter 8. In albinism, a greater number of the temporal retinal fibers cross the midline and project to the contralateral hemisphere and only a small portion of them remain ipsilaterally. Previous studies have demonstrated that the visual cortex in albinism is organized as superimposed retinotopic maps of the ipsi- and contralateral visual hemifields (Hoffmann et al., 2003; Kaule et al., 2014). However, there is no report of pRF and CF properties in albinism. As such, 6 albinotic participants with variable extent of misrouting were studied using fMRI. The data were acquired in Magdeburg. The author of the present thesis contributed to the data acquisition and employed pRF and CF modeling to investigate the topographic organization of the visual cortex and the functional connectivity profiles in albinism.

The following chapters present a series of independent studies in which four conditions associated with transient or congenital changes of the visual system are investigated. The relationship between these conditions is detailed in the last chapter, General discussion.

Chapter 5

Heterogenous migraine aura symptoms correlate with visual cortex fMRI responses

The work presented in this chapter has been published in the following journal article:

5.1   Introduction

Migraine is a highly prevalent and debilitating neurological disease characterized by recurrent and severe episodes of headache. Approximately 10% of the general population suffers from the migraine attacks (Stovner et al., 2007). The annual direct and indirect economic costs of migraine i.e. healthcare and absenteeism expenses have been recently estimated at 18.5 billion Euros in European countries (Gustavsson et al., 2011; Olesen et al., 2012). Thus, mitigation of such a significant public burden necessitates a deeper understanding of its pathogenesis and possible treatment approaches. According to the International Headache Society, the most common types of migraine are migraine without aura and migraine with aura, both of which are identified by intense, throbbing, and unilateral headaches accompanied by nausea, photophobia and phonophobia (of the International Headache Society (IHS) 2013). The later form is the focus of the current study and will be discussed in detail.

5.1.1 Migraine with aura

About one-third of the patients affected by migraine manifest aura as transient, gradually developing neurological symptoms often occurring prior to the headache onset. These symptoms include sight, sensory, motor and speech impairments, typically lasting 5-60 minutes (Lindblad et al., 2017; Russell and Olesen 1996; Vincent and Hadjikhani 2007). Despite tremendous inter- and intra-individual variability in clinical features of the aura, the visual disturbances are the predominant type of aura which are divided into positive and negative subtypes. The positive visual disturbances comprise white flashes of light or bright zig-zag patterns beginning at the center of vision, spreading peripherally in the visual field while the negative symptoms consist of blind regions (scotoma) with similar progression pattern (Hadjikhani et al., 2001; Queiroz et al., 2011). Although the pathophysiological processes triggering the aura is not well understood, the progressive nature of its symptoms may be explained by cortical spreading depression (CSD), a slow self-propagating wave of neuronal and glial depolarization followed by cortical silence and suppression of action potentials (Ayata and Lauritzen 2015; Leo and Morison 1945). There is no direct evidence of CSD in humans nonetheless reduction of cerebral blood flow has been observed using intra-arterial Xenon-133 (Lauritzen and Olesen 1984; Olesen et al., 1981). BOLD signal changes have been also reported in a patient during aura using fMRI (Hadjikhani et al., 2001). However, it was never repeated or confirmed. In fact, conducting systematic studies in patients during aura is notoriously difficult due to the unpredictable and short lasting nature of aura and lack of effective methods in the provocation of aura. In the current study, 5 patients were examined during aura attacks using fMRI. The aura was elicited by hypoxia, sham hypoxia or hard physical exercise combined with photostimulation. It was hypothesized that BOLD signal changes characteristic of CSD would occur during aura and that specific visual symptoms would correspond to different BOLD signal changes.

5.2 Methods

5.2.1 Participants

Five patients (4 females, age 18–46 years) who exclusively suffered from migraine with visual aura and a minimum of 1 attack per month were studied. Exclusion criteria were any other type of headache, any somatic or psychiatric disease, any daily medication except oral contraceptives, smoking and history of mountaineering training (only applied to patients exposed to hypoxia/ sham hypoxia). An overview of the patients' aura characteristics is presented in table 5.1. Patients were recruited from the outpatient clinic at the Danish Headache Center (Rigshospitalet Glostrup, Copenhagen, Denmark) and Danish website for the recruitment of volunteers to health research (www.forsoegsperson.dk). The patients were part of 2 previously published studies (Arngrim et al., 2015; Hougaard et al., 2013). The studies were approved by the ethics committee of the Capital Region of Denmark and the Danish Data Protection Agency. Moreover, the studies were registered at Clinicaltrials.gov (NCT01896167, NCT01388894). In accordance with the Declaration

of Helsinki, written informed consent was obtained from all the patients after the provision of detailed information about the study.

Characteristic	Patient 1	Patient 2	Patient 3	Patient 4	Patient 5
Age	25	27	22	33	46
Years with migraine with aura	12	18	3	1	25
Attacks per month	1	2	1–2	1	1
Negative symptoms (scotoma)	yes	yes	yes	no	no
Positive symptoms	no	Black/white flickering with zigzag border	Black/white flickering with zigzag border	White spots & flickering lines	Black/white flickering with zigzag border
Location in the visual field	Left	Central and peripherally left & right	Right	Right	Left/right
Gradual spreading (min)	10	10	30	30	5
Total duration (min)	20	60	60	60	30
Colors	no	no	no	no	no
Changes whit closed eyes	no	no	no	no	no
Normal central vision	yes	no	yes	yes	yes
Onset of migraine headache in relation to aura	Following	Preceded/accompanied	Often preceded	Following	Following

Table 5.1: Aura characteristics in the patients

5.2.2 Experiment design

Patients underwent fMRI in two separate sessions. In the first session, they were scanned at baseline and during aura (ictal phase). In the second session, retinotopic mapping of the visual cortex was performed (see section 3.2 for details). Aura was provoked in three patients by inhalation of air with reduced oxygen concentration (normobaric hypoxia) resulting in capillary oxygen saturation of 70-75%. In the other two patients, the aura was induced either by exposure to sham hypoxia (atmospheric air) or hard physical activity on an exercise bike combined with photo stimulation. Hypoxia and sham were elicited by an AltiTrainer system (SMTEC, Nyon, Switzerland) through a 7m tube, a 1-way valve, and a tight full-face mask (Hans Rudolph, Shawnee, KS). Furthermore, a fingertip pulse oximeter (Veris Monitor, Medrad; Bayer HealthCare, Whippany, NJ) was utilized to measure the capillary oxygen saturation (SpO2). Patients were required to report the development of any visual disturbances and were immediately placed in the scanner and stimulated with high-contrast motion stimuli. There was some variability in the initiation of the ictal scans (range 8–20 minutes) due to several practical issues such as removal of hypoxia/sham mask, distance to the scanner, placing the patient within the scanner and positioning of goggles for visual stimulation. Upon completion of the scanning, the

patients were interviewed about the aura characteristics and position and if possible, were asked to draw their aura symptoms. In addition, the patients were instructed to complete a validated headache diary until sleep or 12 hours after baseline and were allowed to treat headache with common analgesics and their usual migraine medication. In the second session with a minimum interval of 5 days after the attack (interictal phase), patients were scanned using the traveling-wave paradigm to delineate visual areas (V1 to V4). The experimental design is illustrated in Figure 5.1.
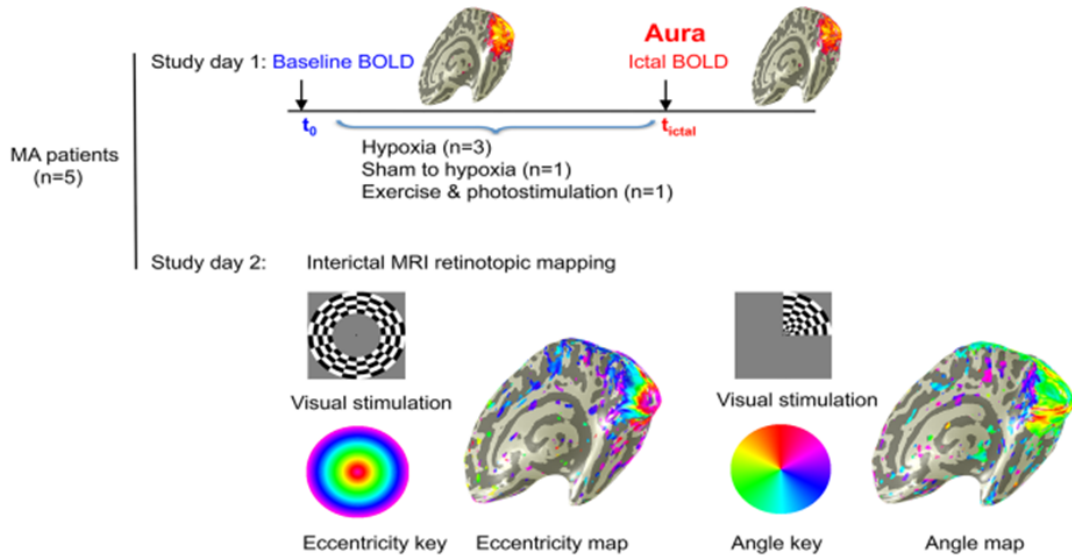
Figure 5.1: **Experiment design**. fMRI was performed on patients in two separate days. On the first day, patients were scanned at the baseline and during aura (ictal phase). On study day 2, patients were scanned during interictal phase using rotating wedge and expanding ring stimuli to define visual areas V1 - V4. Adapted from (Arngrim et al., 2017a).

5.2.3 MRI acquisition

functional and structural images were obtained at a 3 T Philips Intera Achieva scanner (Philips Medical Systems, Best, the Netherlands) using a 32-element phased-array receive head coil. Structural images were acquired using a T1-weighted 3-D turbo field-echo sequence under the following parameters: (TR/TE 9.9/4.6 ms, flip angle: 81° and voxel size: 0.8 x 0.8 x 0.8 mm^3). BOLD fMRI data were obtained using an EPI sequence with 32 slices of 4 mm thickness and in-plane resolution of 2.9 x 2.9 mm. TR and TE were 3000, 35 ms and the flip angle was 90°. Two volumes of each scan were discarded to ensure steady-state longitudinal magnetization. Visual stimulation was presented using OLED video goggles (NordicNeuroLab, Bergen, Norway) with super video graphics array of 800 x 600 pixels, refresh rate of 85 Hz, visual field of 30° x 23° and stimulus luminance of 70–110 cd/m^2. A fiber optic cable connected the system to a control computer outside the scanner room and the onset of visual stimulation was triggered by the scan acquisition.

5.2.4   Visual stimuli

Visual stimulation was presented in a block design mode during the first session. The stimuli consisted of an alternation of high-contrast motion patterns and rest blocks each lasting for 18 seconds. A moving circular black and white dartboard pattern (size = 22° diameter, ring width = 0.6° and spoke width = 15°) was used to elicit neural responses in the visual cortex. Patterns in each spoke moved in opposite directions with random changes of the motion direction approximately every 2 – 3 seconds. The stimuli were generated in Matlab using VISTADISP toolbox (https://github.com/vistalab/vistasoft). Each scan was about 5 minutes in duration, comprising thirty-two blocks. One or more scans were collected for baseline and ictal conditions.

During the second session, phase-encoded retinotopy was employed to define early visual areas. Within a circular aperture of 22° diameter, a high-contrast motion dartboard stimuli stepped either through the polar angles as a rotating wedge or through the eccentricities as an expanding ring to map the polar angle and eccentricity respectively. The wedge was 6 segments and 90° wide, rotating counterclockwise around the center of the visual field. The ring comprised 3 checks, 0.6° wide. Both stimuli passed through a full display cycle over 36 s and 7 cycles were repeated per scan (total duration = 252 seconds). For each patient, two repetitions of both polar angle and eccentricity mapping fMRI scans were collected which were averaged for subsequent analysis.

5.2.5   Data analysis

Gray and white matter were segmented from the T1-weighted image using the recon-all function of FreeSurfer (https://surfer.nmr.mgh.harvard.edu). Hand-editing was performed to lessen the segmentation error (Teo et al., 1997). The cortical surface was reconstructed based on the segmented T1-weighted image and rendered as a smoothed 3-D surface Wandell et al., 2000. Functional runs were corrected for motion artifacts using MCFLIRT function of FSL (https://www.fmrib.ox.ac.uk/fsl). Motion corrected data were subsequently analyzed using mrVista software package (https://github.com/vistalab/vistasoft). For the retinotopic mapping session, functional time series of the same conditions were averaged across repetitions for each patient to increase the signal-to-noise ratio (SNR). Afterwards, the structural image was aligned to the functional scan. For each voxel, a Fourier analysis was applied to the time series to obtain the phase and amplitude values at the stimulus fundamental frequency (f_0 = 7) (Engel et al., 1997). The phase values correspond to the representation of the visual field regions and were projected onto the cortical surface to visualize the eccentricity and polar angle maps used for delineation of the early visual areas. For the baseline and ictal scans, the strength of the stimulus driven activity in each voxel was determined by calculating the coherence, defined as the Fourier amplitude of the BOLD signal at the stimulus fundamental frequency (f_0 = 16), divided by the sum of amplitudes of a range of frequencies around the fundamental (see equation 5.1) (Baseler et al., 2011; Masuda et al., 2008; Smirnakis et al., 2005).

$$C = A(f_0)/(\sqrt{\sum A(f)^2}) \qquad (5.1)$$

In each visual area, only voxels were selected for further analysis whose activation was above a coherence threshold of 0.30 (corresponding to an uncorrected probability value of 0.000012). V1 to V3 were subdivided into dorsal (d) and ventral (v) parts for a separate analysis of the lower and upper visual field. For the sake of consistency, the parts of V4 corresponding to the upper and lower visual field were also termed V4v′ and V4d′, however, this nomenclature does not correspond to the anatomical locations of these V4 ROIs. To identify differences between baseline and ictal scans in each patient, BOLD responses in ventral and dorsal V1 to V4 of both hemispheres were compared in terms of (i) the mean main stimulus parameter estimates (beta values), indicated by the percentage changes from baseline periods to visual stimulation periods; (ii) average single cycle time series; (iii) average time series; and (iv) Fourier transforms of each ROI time series and resultant frequency spectra with associated z scores (Figure 5.2). The
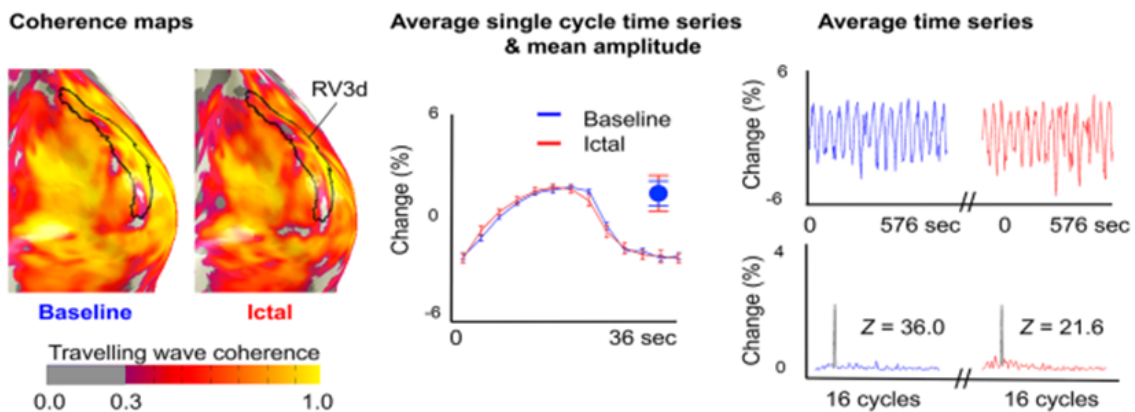
Figure 5.2: **BOLD response comparison between baseline and ictal scans**. Coherence maps were superimposed on inflated cortex at a threshold of 0.3 (left panel). Bold time series were evaluated as average single cycle, mean percentage amplitude changes (round symbols with error bars; the middle panel), average time series (right panel, top row) and Fourier transforms of each ROI, and its spectra with associated z scores(right panel, bottom row). Depicted data are from dorsal V3 of the right hemisphere in patient 1. Adapted from (Arngrim et al., 2017a).

amplitude of the power spectra peaks was compared between baseline and aura (ictal) scans with variance estimated from the rest of the spectrum using an independent test (n = 16 cycles). MATLAB (Mathworks, Natick, MA, USA) was used for all statistical analysis and the data were tested with Bonferroni correction for multiple comparisons, i.e. a significance level of p < 0.0016.

5.3   Results

Five migraineurs underwent fMRI scanning in two sessions. In the first session, they were scanned at baseline and during visual aura (ictal phase) while in the second session they

were scanned in the interictal phase for retinotopic mapping (see Figure 5.1). The aura symptoms and corresponding BOLD changes in each patient are reported below.

Patient 1

After exposure to 170 minutes of hypoxia, the patient developed visual aura and was scanned 15 minutes later. The aura composed of a semicircular central scotoma with a flickering black–white zig-zag border located in the right hemifield spreading gradually to the upper right quadrant and faded after 30 minutes. The mean amplitude of the BOLD signal to visual stimulation decreased in dorsal and ventral visual areas of the left hemisphere specifically in V2 - V4, matching with aura location. There was no ictal drop in response amplitude in the right hemisphere. Detailed comparison of the BOLD response between baseline and aura scans as well as the patient aura drawing are shown in Figures 5.3 and 5.7, 1$^{\text{st}}$ row respectively.

Patient 2

Visual aura was provoked an hour after 3 hours of exposure to sham hypoxia. Due to MRI preparation procedures, the patient was scanned 20 and 35 minutes later. The aura consisted of a central expanding scotoma with a flickering black–white zig-zag border spreading slowly from the center and lower right quadrant to the upper right and left quadrants and vanished after 46 minutes. During the ictal phase, the mean amplitude of the BOLD response to visual stimulation decreased in the left ventral areas and right dorsal and ventral ROIs. No difference was found between baseline and ictal scans in the dorsal areas of the left hemisphere. Bihemispheric changes in BOLD signal correspond with the central location of scotoma, whereas the patient did not experience flickering in the lower quadrant of the left hemifield (see Figure 5.6 and 5.7, 2$^{\text{nd}}$ row).

Patient 3

Following 78 minutes of hypoxia, the patient developed visual and sensory aura and was scanned 12 minutes after the aura onset. The duration of the visual and sensory symptoms was 119 and 40 minutes, respectively. Subsequently, the patient was taken out of the scanner, received proper medication (sumatriptan; 100 mg intramuscular) and was scanned again during the postictal phase. Numbness, prickling and stinging sensation in the right arm constituted the sensory symptoms while visual symptoms contained black and white spots with black-white flickering which began in the right upper quadrant and progressed centrally toward both upper quadrants. The mean amplitude of the BOLD response to visual stimulation was reduced during aura. This reduction was most clear in V1 of both cortices during the first ictal scan. Despite the patient's report on the presence of the visual symptoms in both upper visual quadrants, no remarkable differences were observed between dorsal and ventral areas. In postictal phase, the amplitude increased again in ventral regions of the left hemisphere as well as dorsal and ventral areas of the right hemisphere after sumatriptan injection (see Figures 5.4 and 5.7, 3$^{\text{rd}}$ row).

Patient 4

Visual aura was elicited after 75 minutes of arduous exercise combined with photo-stimulation and the patient was scanned 8 minutes later. The aura began with white spots and flickering lines located peripherally in the left and right visual hemifields progressing slowly to the upper parts and disappeared after 26 minutes. In contrast to the other
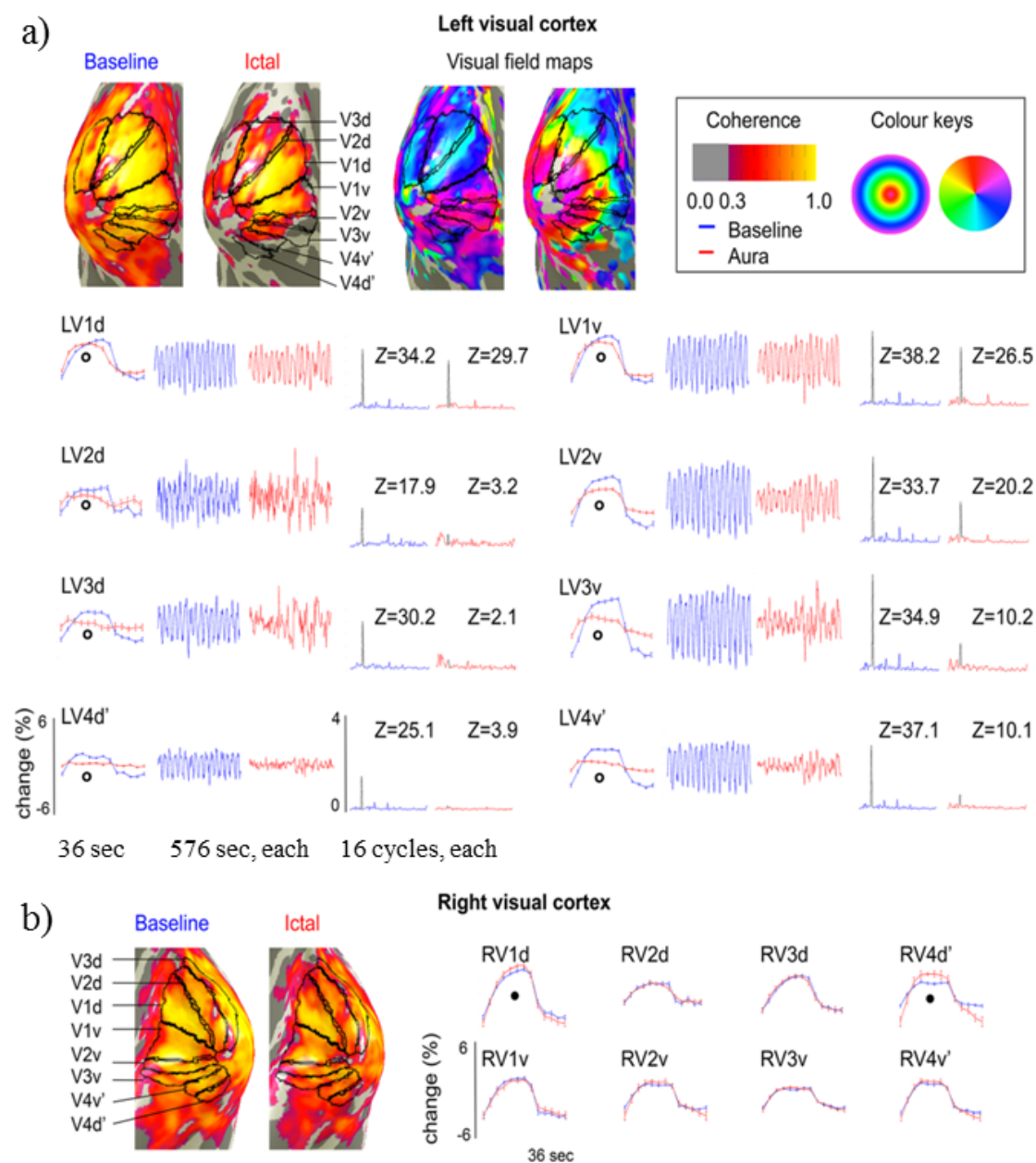
Figure 5.3: **BOLD response alterations in patient 1**. **a)** Left hemisphere. A noticeable difference in BOLD response to visual stimuli was observed between baseline and ictal scans. The coherence maps thresholded at 0.3 (first row, left panel) showed an explicit reduction during ictal phase. In the next rows, the BOLD signal plotted as a function of time (average single cycle and average time series) indicated decreased amplitude in left dorsal and ventral V2, V3, and V4'. Fourier analysis of the average time series revealed no peak signal at the stimulation frequency (z scores < 4.0) in left dorsal V2-V4. In ventral V2 to V4, the spectra showed peaks at the stimulation frequency with lower amplitude and z scores during ictal scan compared to baseline scan. **b)** Right hemisphere. No difference was seen between the baseline and ictal scans in the right visual cortex except for the dorsal V4' indicating a slight amplitude increase in the ictal phase. Probability values < 0.016 for comparison of baseline versus aura scans are shown with empty circles (decrease) and filled circles (increase). Adapted from (Arngrim et al., 2017a).

three patients, the mean amplitude of the BOLD response to visual stimulation revealed bilateral increase during aura in ventral V1 to V3 and dorsal V4 areas. No difference was found in early dorsal areas of both hemispheres, matching with the location of visual symptoms (Figures 5.5 and 5.7, 4th row).
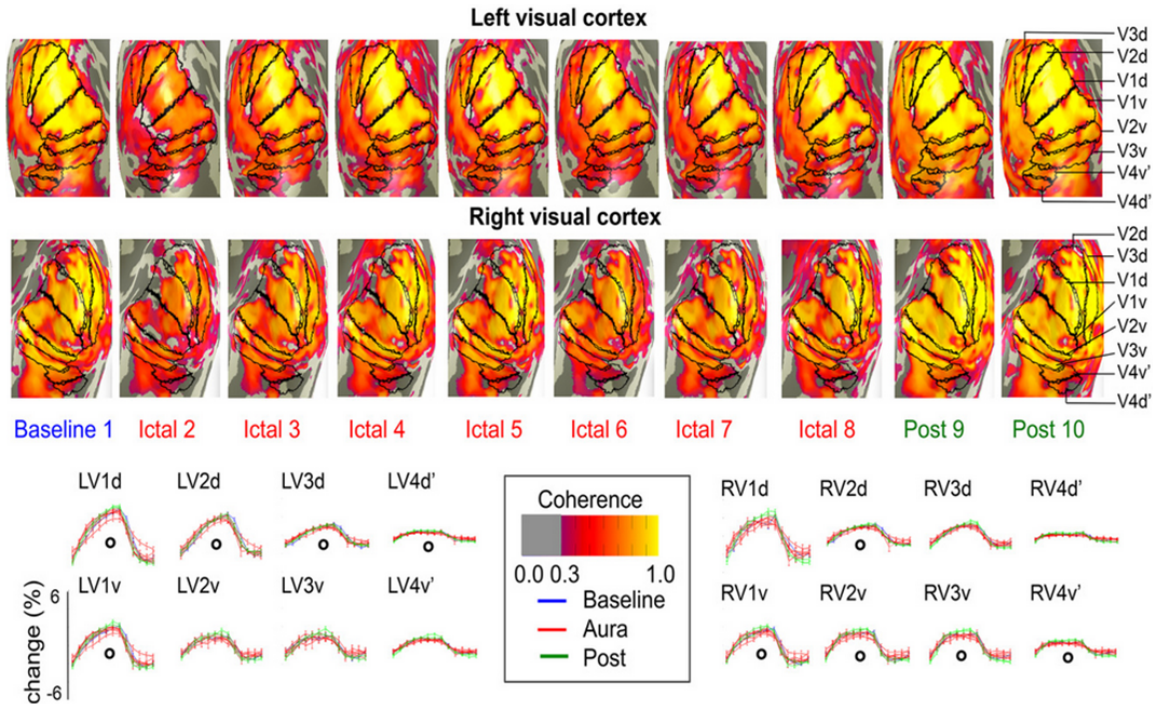

Figure 5.4: **BOLD response alterations in patient 3**. The coherence maps revealed lower coherence in response to stimuli during the ictal scan compared to baseline in all ROIs, most pronounced in the first ictal scan. The BOLD signal plotted as a function of time (average single cycle time series) showed lower amplitude, primarily in the first ictal scan in left dorsal and ventral V1. Furthermore, overall lower amplitudes and z scores were observed in frequency spectra during aura (plots not shown). Probability values < 0.016 for comparison of baseline versus aura scans are indicated with empty circles (decrease). Adapted from (Arngrim et al., 2017a).

Patient 5

The patient developed aura after 130 minutes of breathing in hypoxia and was scanned 15 minutes later. The aura initiated as flickering in the upper quadrants that spread centrally and to the lower quadrants, forming an open circle around the middle of the visual field which lasted for 150 minutes. Afterwards, the patient was taken out of the scanner, received 100 mg of sumatriptan and was scanned again during the postictal phase. The mean amplitude of the BOLD response to visual stimulation increased during aura in all regions of both cortices. The amplitudes were still higher in postictal scans compared to baseline, except for ventral areas of V1 to V3 of the left hemisphere. Detailed information on BOLD signal variations and a schematic drawing of the patient aura have been provided in Figures 5.6 and 5.7 (5th row).
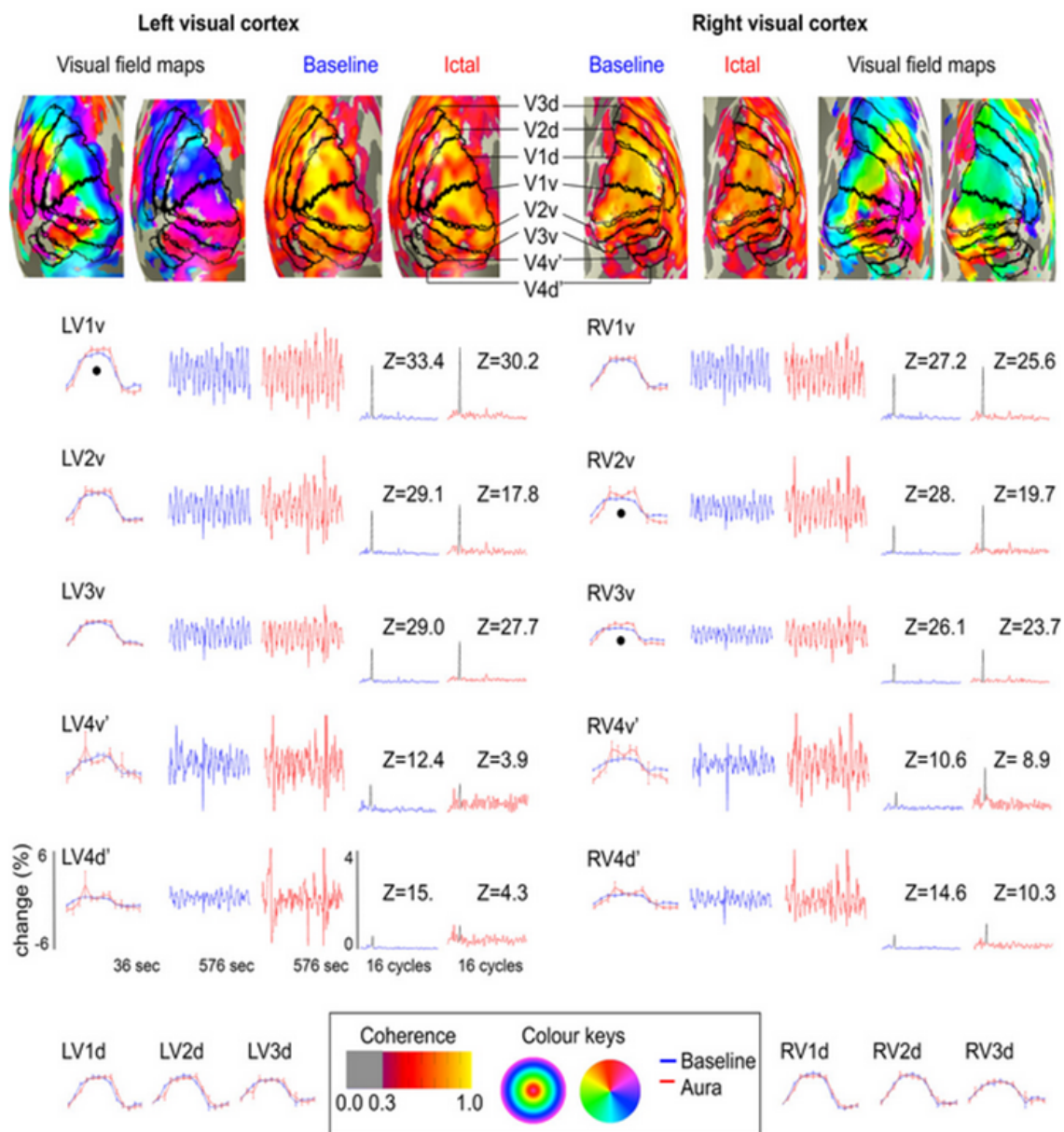
Figure 5.5: **BOLD response alterations in patient 4**. The coherence maps thresholded at 0.3 indicated lower coherence in dorsal and ventral V4' in the left hemisphere during the ictal scan compared to baseline. The BOLD signal plotted as a function of time (average single cycle time series and average time series) showed higher amplitudes in left ventral V1 to V2 and right ventral V2 to V4. In the dorsal areas, no bilateral differences were found in the average single cycle time series. The frequency spectra showed low amplitudes at the stimulation frequency in left ventral and dorsal V4' (z score = 3.9 and 4.3 respectively). The average time series plots revealed no changes in signal amplitude during the aura scan in any ROIs. Moreover, the average time series revealed motion artifacts. Probability values < 0.016 for comparison of baseline versus aura scans are indicated with filled circles (increase). Adapted from (Arngrim et al., 2017a).
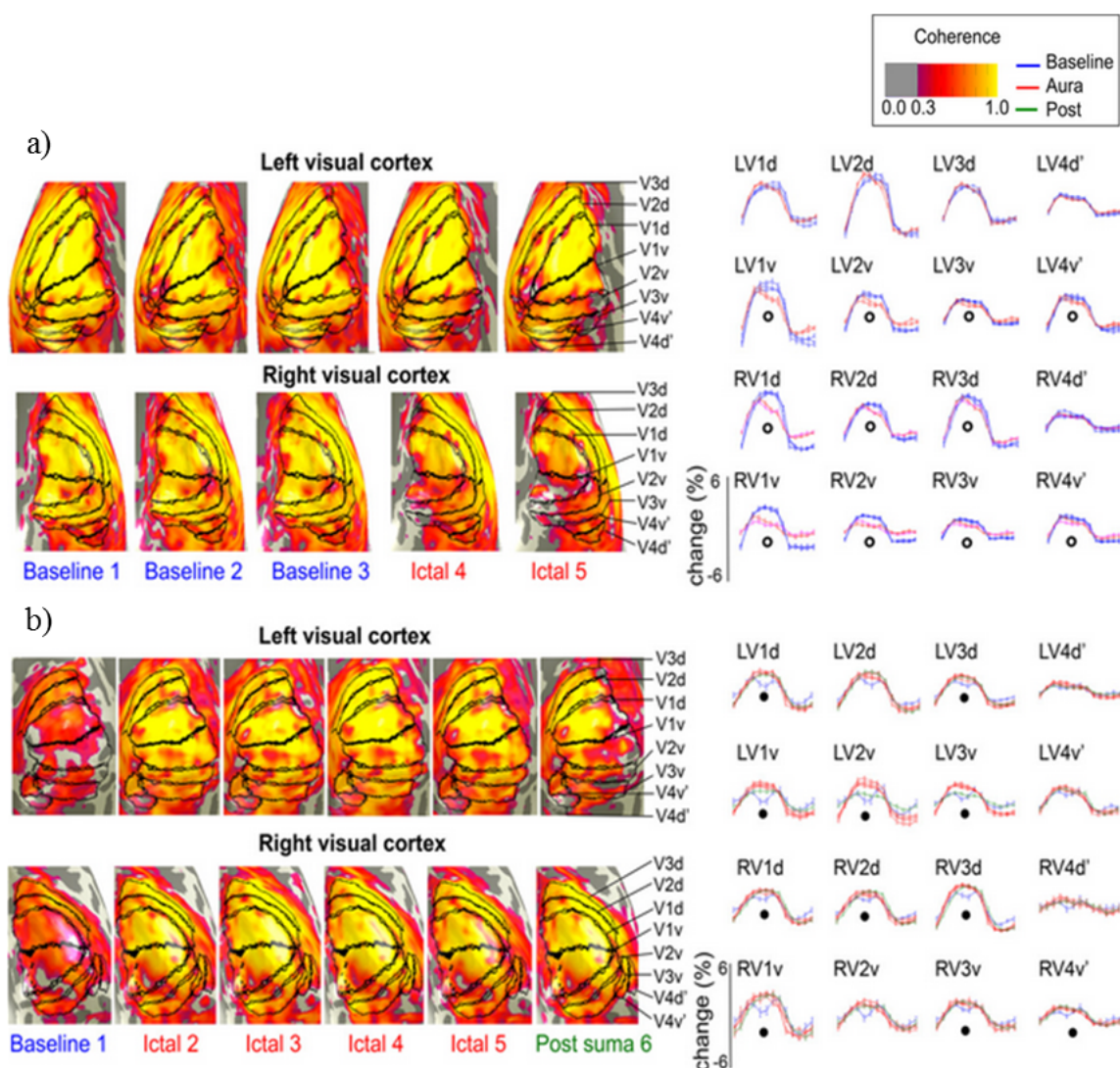
Figure 5.6: **BOLD response alterations in patients 2 and 5**. **a)** patient 2. The coherence maps thresholded at 0.3 manifested lower coherence in response to stimuli during the ictal scan compared to baseline in the ventral regions of both cortices. The BOLD signal plotted as a function of time (average single cycle time series) revealed reduced amplitudes in all areas except the left dorsal ROIs. In addition, the frequency spectra (plots not shown) showed lower amplitudes and z scores in all ROIs except the left dorsal ROIs. The average time series showed a drop in signal amplitude of right ventral V1 and V2 in the first ictal scan which did not recover during the second ictal scan (plots not shown). **b)** patient 5. The coherence maps thresholded at 0.3 exhibited a higher coherence in all ROIs during ictal scans compared to baseline. The BOLD signal plotted as a function of time (average single cycle time series) also showed increased amplitudes at ictal scans. Fourier analysis of the average time series indicated higher peak signal amplitudes at the stimulation frequency with higher z scores at ictal and postictal scans compared to baseline (plots not shown). Probability values < 0.016 for comparison of baseline versus first aura scans are indicated with empty circles (decrease) and filled circles (increase). Post suma indicates post sumatriptan scan. Adapted from (Arngrim et al., 2017a).
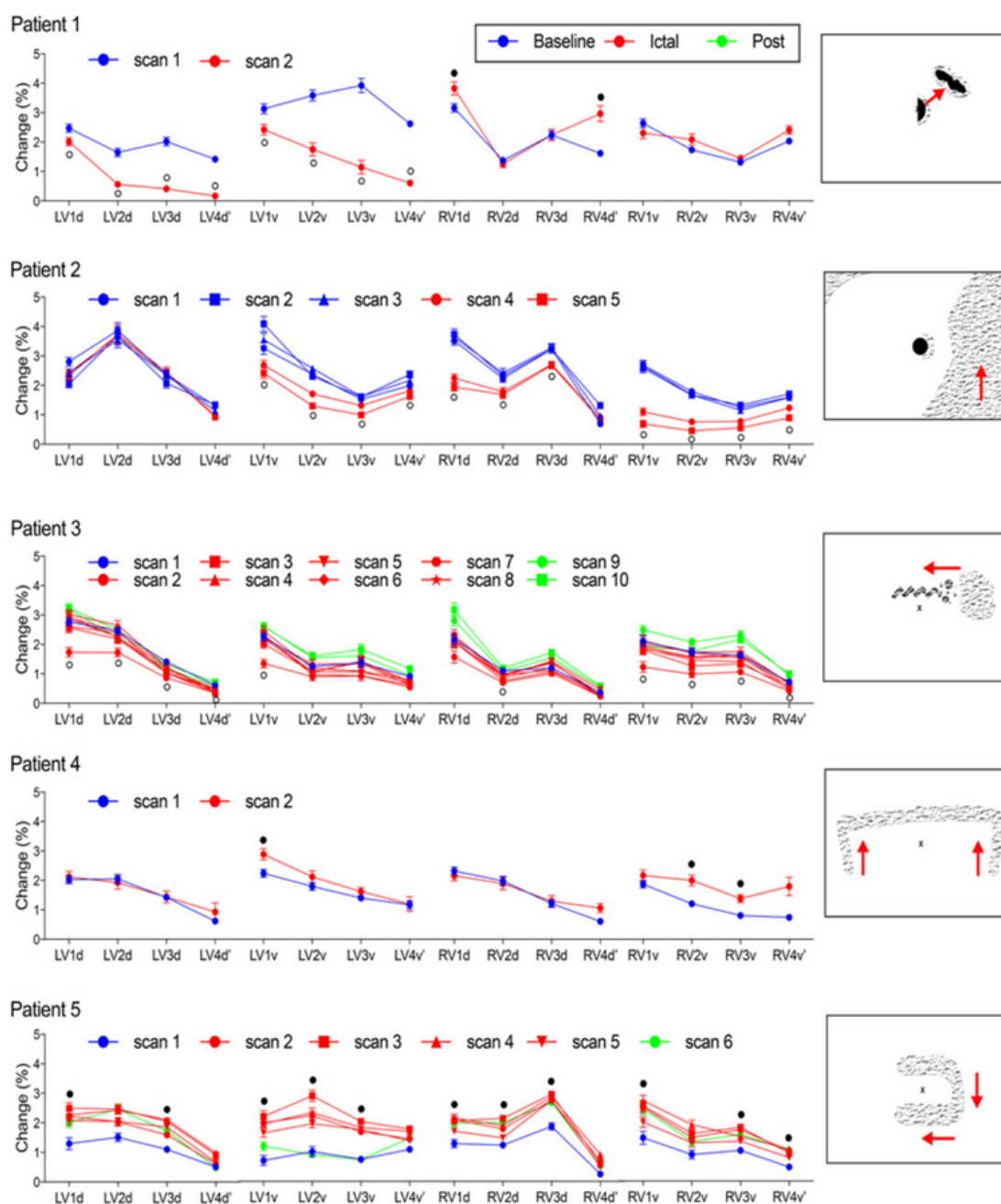
Figure 5.7: **BOLD response alterations and schematic drawings of aura location in patients 1-5**. Average percentage amplitude changes in BOLD response in areas V1-V4′ and drawings of the location of the patients' aura symptoms are presented. Red arrows indicate the direction of symptoms progression. Patients 1 and 2 had visual scotoma and flickering (1st and 2nd rows). Patient 3 had a cluster of black and white spots and flickering (3rd row). In contrast, patients 4 and 5 only experienced positive symptoms (Patient 4: white spots, flickering lines; Patient 5: flickering; see 4th and 5th rows). Probability values < 0.016 for comparison of baseline versus first aura scan are indicated with empty circles (decrease) and filled circles (increase). In Patient 2, the last baseline scan (scan 3) was considered as reference. Reprinted from (Arngrim et al., 2017a).

5.4   Discussion

The current study demonstrates that the clinical heterogeneity of visual aura symptoms correlates with specific heterogeneous responses in the visual cortex. The BOLD signal was decreased in patients experiencing negative aura symptoms i.e. scotoma and increased in patients who had positive symptoms such as flickering flash of light. Moreover, bihemispheric BOLD signal alterations were detected in patients with bilateral auric symptoms. These findings indicate that various visual aura symptoms reflect different dysfunctional processes in the brain that can be measured by fMRI.

Despite growing consensus on CSD as the underlying mechanism of migraine aura, the relationship between the multifaceted phenomenology of aura symptoms and CSD has been rarely studied. In the only previous fMRI study during migraine with aura, Hadjikhani et al., described 3 patients with visual aura symptoms and reported decreased BOLD response during unilateral scintillating scotoma in 1 patient (Hadjikhani et al., 2001). In the present study, however, 5 patients with diverse aura symptoms were scanned. A diminished BOLD signal was observed in Patients 1 and 2 experiencing negative symptoms (scotomas) accompanied by a positive symptom (flickering), as well as patient 3, who probably had both negative (black spots) and positive (white spots, flickering) symptoms. By contrast, patients 4 and 5 who had only positive symptoms (white spots and flickering lines, and flickering, respectively) exhibited an increased BOLD response.

Different effects of CSD on the cerebral blood flow might explain BOLD signal variations during positive and negative symptoms. Empirical studies during aura attacks in humans have shown blood perfusion changes (Olesen et al., 1990, 1981). While some patients exhibit decreased cerebral blood flow (oligemia), others express an initial focal increase (hyperemia). Thus, the reduction of the BOLD response during scotomas can be attributed to the depression of neural activity following CSD. Interestingly, the observed increased BOLD signal during flickering was exclusive to patients 4 and 5 even though the first three patients also experienced flickering with scotoma. A plausible explanation could be that the positive symptoms of the aura which reflect the depolarization wave during CSD often emerge in the border of the longer lasting scintillating scotoma representing electrically silent cortical areas. The predominance of negative symptoms during aura would result in an overall decrease in the BOLD response. An alternative explanation could be that in patients 4 and 5 who only experienced positive symptoms, the hyperexcitable neurons recover expeditiously after CSD-induced depolarization thus producing a greater mean BOLD response, while in patients 1, 2, and 3 who had negative symptoms accompanied by positive symptoms, the neurons are hyperpolarized for several minutes (the duration of scotomas) following depolarization, leading to a net drop in BOLD response.

According to a recent prospective study, almost 35% of migraine patients with aura have bilateral visual symptoms (Viana et al., 2017). Bilateral blood perfusion changes have also been reported in single subjects using single-photon emission computed tomography (SPECT) (Andersen et al., 1988; Lauritzen and Olesen 1984). Four out of five patients participating in the current study had bilateral symptoms with corresponding bihemispheric changes in BOLD response. In patient 4, the symptoms began in the left

and right visual hemifields simultaneously and had the same progression pattern, indicating presence of a wave of CSD in each hemisphere, whereas in the other patients the aura symptoms had an unequal distribution across hemifields spreading gradually over the midline. The mechanism of bilateral CSD is still unclear. Presumably, CSD propagates from one hemisphere to the other through the corpus callosum, analogous to the pathophysiological mechanism of seizure generalization over the corpus callosum in epilepsy. Connectional diaschisis, as described in stroke patients might be another potential mechanism in which functional alterations may occur in intact regions contralateral to the lesioned area (Carrera and Tononi 2014).

In some patients, a mismatch was found between the reported location of the aura symptoms in the visual field and BOLD signal changes in cortical visual areas. This could be due to memory-retrieval problems with respect to aura symptoms. Furthermore, patients may have an unconscious memory bias toward more prominent symptoms. It is also possible that the observed mismatch indicates the silent propagation of CSD. In support of this notion, it has been shown that hypoperfusion extends beyond visual cortex in some patients who only experience visual symptoms (Olesen et al., 1990).

5.4.1 Limitations

There are a few limitations in this study that should be considered. Ideally, the patients should be scanned immediately before the beginning of aura symptoms. Nevertheless, it was not possible due to the unpredictable nature of aura. To avoid recalling difficulties, patients should ideally describe and draw their aura symptoms during the attacks. However, it was postponed because of the higher importance of instant scanning. The similarity of the spontaneous and experimentally provoked aura is another issue which needs to be addressed. Although the triggering factors are different, any kind of aura is provoked by some factors. Furthermore, according to the patients' report, the provoked aura resembled their spontaneous attacks and fulfilled the criteria of International Classification of Headache Disorders (ICHD). Finally, it might be questioned whether the magnitude of BOLD signal is affected by hypoxia. Several lines of evidence indicate BOLD signal reduction during hypoxia (Duong 2007; Rostrup et al., 2005). However, in the current study fMRI was performed after termination of hypoxia. Recently, Arngrim et al., have shown that cerebral blood flow and the BOLD response are normalized after experiencing the same hypoxic challenge in healthy volunteers who were matched in terms of gender and age to a group of patients suffering from migraine with aura (Arngrim et al., 2017b). Moreover, similar BOLD changes were observed in patient 5 who was exposed to hypoxia and patient 4 undertaking demanding physical exercise combined with photo stimulation.

5.4.2 Conclusion

In summary, the present study demonstrates that clinical variabilities in migraine aura symptoms are linked to disparate neurophysiological responses in the visual cortex that can be identified by fMRI. Positive and negative symptoms influence BOLD signal differ-

ently which reflects distinct effects of CSD on the cerebral activity and haemodynamics. Specifying these pathophysiological mechanisms would bring us a step further towards understanding the uncharted terrain of migraine aura. Future studies should assess regional cerebral blood flow alterations along with BOLD response during aura using PET MRI. In addition, it would be compelling to study changes of neurophysiological responses within patients through repetition of provoked auras.

In this chapter, the potential of retinotopic mapping for relating visual functions and cortical signals was highlighted. This potential is in the subsequent chapters applied to the congenital chiasmal abnormalities.

Chapter 6

Altered organization of the visual cortex in FHONDA syndrome

The work presented in this chapter has been published in the following journal article:

Ahmadi, K., Fracasso, A., van Dijk J.A., Kruijt, C., van Genderen, M., Dumoulin, S.O., Hoffmann, M.B. (2019). Altered organization of the visual cortex in FHONDA syndrome. NeuroImage (190), 224-231.

It has also been published in abstract form in the following conference proceedings:

Ahmadi, K., Fracasso, A., van Dijk J.A., Kruijt, C., van Genderen, M., Dumoulin, S.O., Hoffmann, M.B. (2017). Cortical plasticity in FHONDA – a new inherited visual system disorder. European Conference on Visual Perception (ECVP), Berlin, Germany.

Ahmadi, K., Fracasso, A., van Dijk J.A., van Genderen, M., Dumoulin, S.O., Hoffmann, M.B. (2016). Altered retino-cortical connections and visual cortex reorganization in the recently discovered FHONDA syndrome. Society for Neuroscience (SfN), San Diego, USA.

6.1   Introduction

As outlined in chapter 2, topographic representation of the contralateral visual hemifield on each hemisphere is a fundamental organizational principle of the visual cortex, arising from pre-programmed and experience-dependent mechanisms that form the retino-cortical wirings. Investigation of conditions with sizable alteration of these wirings offers a unique opportunity to directly assess the scope of plasticity in the human visual system. Normally, nasal retinal afferents cross the optic chiasm and project to the contralateral hemisphere while temporal retinal axons remain uncrossed and project to the ipsilateral hemisphere. As such, the right visual hemifield is represented on the left hemisphere and vice versa.

This projection scheme is altered in congenital visual pathway abnormalities, as detailed in section 2.2. Absent or reduced crossing of nasal retinal fibers has been observed in achiasma and hemihydranencephaly (Apkarian et al., 1994; Fracasso et al., 2016; Hoffmann et al., 2012; Muckli et al., 2009; Victor et al., 2000), whereas enhanced decussation of temporal retinal axons has been reported as a pathognomic sign of albinism (Apkarian et al., 1983; von dem Hagen et al., 2008). The recent discovery of the FHONDA syndrome, however, has disputed this view and questioned the definition of albinism (Al-Araimi et al., 2013; Poulter et al., 2013).

FHONDA (foveal hypoplasia, optic nerve decussation defects and anterior segment dysgenesis) is a rare and novel entity of the congenital visual pathway disorders, caused by a recessive mutation in the putative glutamine transporter gene SLC38A8. Clinical symptoms of the affected individuals include poorly defined foveal avascular zone, abnormal foveal or macular reflexes and missing foveal pit manifested in optical coherence tomography (OCT) scans. Visual evoked potential (VEP) records display additional crossing of the retinal axons at the optic chiasm. Moreover, Axenfeld's anomaly or posterior embryotoxon have been reported in some cases as anterior segment abnormalities (Al-Araimi et al., 2013; Poulter et al., 2013; van Genderen et al., 2006). Although FHONDA and albinism share common characteristics i.e. underdeveloped fovea and optic nerve decussation defects, presence of albinism is an exclusion criterion for the diagnosis of FHONDA. Lack of hypopigmentation and iris translucency clearly distinguishes FHONDA from albinism.

Due to misrouting of the retino-cortical connections in achiasma, hemihydranencephaly and albinism, the visual cortex receives substantially erroneous input from the ipsilateral visual field in addition to the normal input from the contralateral visual field, resulting in superimposed retinotopic maps of opposing visual hemifields as reported by several fMRI studies (Davies-Thompson et al., 2013; Fracasso et al., 2016; Hoffmann and Dumoulin 2015; Hoffmann et al., 2012, 2003; Kaule et al., 2014). Counterintuitively, this gross anatomical abnormality does not have a profound effect on visual function (Hoffmann and Dumoulin 2015; Klemen et al., 2012). This is taken as evidence for effective developmental mechanisms that make the erroneous visual input available for perception and highlights the importance of these conditions as unique models to assess the scope of plasticity in the human visual system.

The newly described FHONDA syndrome opens up the possibility of probing the

previously reported interplay of geniculo-cortical stability and cortico-cortical plasticity. Therefore, the aim of the present study was to determine the projection abnormality in FHONDA using fMRI-based population receptive field (pRF) mapping at 7 T. Our results provide evidence for large-scale abnormal input to the visual cortex and indicate that despite the difference between FHONDA and other congenital visual pathway disorders, the principles of cortical mapping are identical.

6.2   Methods

6.2.1   Participants

Two individuals with FHONDA [F1 and F2; aged 27 and 33 respectively; decimal visual acuity (left|right): 0.16|0.10 and 0.20|0.16,respectively; nystagmus amplitude of 0.65° (horizontal) and 0.55° (vertical) in F1 (dominant eye: right), no data available in F2 (dominant eye: left); both females] and two controls (C1 and C2, aged 32 and 23 respectively; 1 female) with no neurological and ophthalmological history and normal visual acuity took part in this study. FHONDA participants were sisters who have been described in detail in previous studies (Al-Araimi et al., 2013; Poulter et al., 2013; van Genderen et al., 2006). All participants gave their informed written consent. The study procedure followed the tenets of the declaration of Helsinki and was approved by the ethical committee of the University Medical Center Utrecht.

6.2.2   Visual stimulation

Drifting bar apertures exposing a checkerboard pattern at 100% contrast in four directions were used (Dumoulin and Wandell 2008). Each pass of the bars lasted for 30 s and subsequently a mean luminance block (zero contrast) of 30 s was displayed. Visual stimuli were generated in Matlab programming environment (Mathworks, Natick, MA, USA) using the Psychtoolbox extensions (Brainard and Vision 1997; Pelli 1997) and projected onto a screen with a resolution of 1024 x 538 pixels at the magnet bore. The stimulus radius was 6° of visual angle. The participants viewed the screen at a distance of 35 cm via an angled mirror and their dominant eye was stimulated under three experimental conditions: bilateral, left, and right hemifield stimulation. During stimulus presentation, the participants were instructed to fixate on a small centered disc and to report colour changes of the disc via button press. An illustration of the bilateral stimuli is exhibited in Figure 6.1. Due to the presence of nystagmus in FHONDA participants, an additional stimulation condition ('fixation jitter') was introduced for the controls in which the fixation disc was moving in the same way as recorded for the nystagmus in F1 with an Eyelink II system (SR Research, https://www.sr-research.com) while observing pRF mapping stimuli outside of the MRI-scanner.
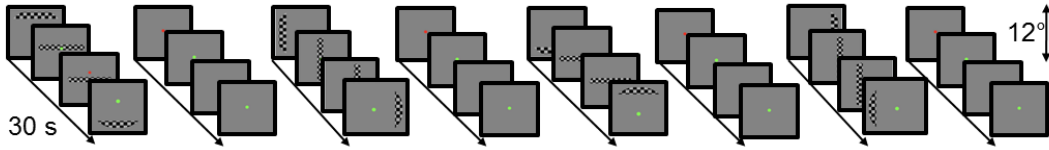
Figure 6.1: **Schematic representation of the visual stimulation sequence for the bilateral pRF mapping**. Each column illustrates screen shots of four blocks of stimulation each of which lasts for 30 s. In every block, bars are moving in one of four different directions. Following each stimulation block, a mean luminance block of 30 s is presented. Adapted from (Ahmadi et al., 2019).

6.2.3 MRI acquisition

Functional and anatomical volumes were acquired at a 7 T Achieva Philips MRI scanner (Best, Netherlands) equipped with a 32-channel head coil (Nova Medical, MA, USA). Foam padding was used to minimize the head motion. Functional $T2^*$-weighted volumes were acquired using a multi-slice EPI sequence at a resolution of 2.5 x 2.5 x 2.5 mm^3 with 25 coronal slices. Repetition and echo time (TR / TE) were 1500 ms / 30 ms respectively, and the flip angle was 70°. Each functional run had 168 time frames, lasting for 252 s. Between 5 to 7 functional runs were performed within the same session for each participant. Each left and right hemifield stimulation conditions were performed once for all of the participants. Bilateral stimulation was repeated four times in F1 and three times in F2. In controls, bilateral stimulation was divided into 'central fixation' and 'fixation jitter'. In C1, two repetitions with central fixation and two runs with fixation jitter were obtained while in C2, three repetitions with central fixation and two runs with fixation jitter were performed. In addition to the functional runs, a whole-brain T1-weighted anatomical volume was acquired at a resolution of 0.8 x 0.8 x 0.8 mm^3 with TR, TE and flip angle of 7 ms, 2.84 ms and 8°.

6.2.4 Preprocessing of MRI data

Motion correction of functional scans and automatic segmentation of the anatomical volume were performed in FSL (https://www.fmrib.ox.ac.uk/fsl). Gray and white matter were further segmented by a custom software and hand edited to minimize the error (Teo et al., 1997). Subsequently, the cortical surface was reconstructed at the white/gray matter border and rendered as a smoothed 3D surface (Wandell et al., 2000). Motion corrected functional data for the same conditions were averaged together for each participant to increase the signal-to-noise (SNR) ratio. Afterwards, the functional scans were aligned to the anatomical volume using mrVista software package for Matlab (https://github.com/vistalab/vistasoft). Due to technical issues associated with the big size of the sinus close to the right occipital cortex in C2, the anatomical volume in this participant was aligned to the functional runs using the 3dAllineate function of AFNI (https://afni.nimh.nih.gov/).

6.2.5   Population receptive field analysis

Delineation of the early visual areas and estimation of population receptive field properties were performed according to the procedure described in section 3.3. Briefly, fMRI time-series of each voxel were predicted by a circular and symmetric Gaussian pRF model characterized by three stimulus-referred parameters i.e. center positions (x and y) and size (σ) of the most responsive part of the voxels to the stimulus. By convolution of the stimulus sequence for the respective pRF model with a canonical hemodynamic response function, the predicted fMRI time courses were generated. The optimal pRF parameters for each voxel were then found by minimizing the residual sum of squares (RSS) between the predicted and the observed fMRI responses (Dumoulin and Wandell 2008). For all subsequent analysis, only the voxels were selected that exceeded 20% of the variance explained. To assess whether a given cortical region in FHONDA contains a single or bilateral pRFs, we extended the conventional pRF model in analogy to previous studies (Fracasso et al., 2016; Hoffmann et al., 2012). The extended models (here referred to as mirror-pRF models) comprise two mirrored 2D Gaussians while the conventional model (here referred to as single-pRF model) is composed of one 2D Gaussian. In contrast to the conventional model, the mirror-pRF models predict that each cortical region responds to two distinct points in the visual field. The extended models were mirrored across (i) the vertical meridian ('mirror-pRF model across VM'), (ii) the horizontal meridian ('mirror-pRF model across HM'), and (iii) fixation ('mirror-pRF model across fixation'). A schematic representation of the mirror-pRF models is shown in Figure 6.2. Since all parameters of the two Gaussians are linked, the mirror-pRF models have the same degrees of freedom as the single pRF model. Thus, the performance of the models can be compared directly, which would have been more complicated for less constrained pRF models.

6.3   Results

We compared the four pRF models in FHONDA and control participants by analysis of the data obtained for bilateral stimulation condition. This comparison was based on the average goodness of fit, i.e. variance explained (VE) within the primary visual cortex. As depicted in Figure 6.3 and 6.4, the mirror-pRF model across VM prevailed in both FHONDA participants whereas the single-pRF model was superior in controls. Inspection of fMRI time-series for a given voxel of V1 revealed that in FHONDA the mirror-pRF model across VM provided a better fit to the observed signal by capturing deflections that were missed by the single-pRF model (VE for single and mirror-pRF models in F1: 50.8% and 71% respectively). Conversely, the single-pRF model explained most of the time-series variance in controls (VE for single and mirror-pRF models in C1: 86.73% and 57.15%; see Figure 6.3 a). It should be noted that for the sake of better visualization of the model differences, only voxels were chosen which represented an extreme difference between the two models in both participants. Another line of evidence confirming the superiority of the mirror-pRF model across VM in FHONDA and supremacy of single-pRF model in controls is presented in Figure 6.3 b, where the cortical topography of the differential variance explained (subtraction of single- from mirror-pRF model across

VM) is shown for both groups. This discrepancy was further supported by quantitative assessment of the mean variance explained for (i) single-pRF model and mirrored-pRF models across (ii) VM, (iii) fixation and (iv) HM, verifying the outperformance of the mirror-pRF model in FHONDA participants (mean VE $\pm$ SEM for the above mentioned models (i–iv) in F1: (i) 58.74% $\pm$ 0.31, (ii) 60.32% $\pm$ 0.30, (iii) 53.16% $\pm$ 0.35, (iv) 52.4% $\pm$ 0.32, and F2: (i) 58.44% $\pm$ 0.24, (ii) 59.15% $\pm$ 0.22, (iii) 51.43% $\pm$ 0.21, (iv) 48.76% $\pm$ 0.21 respectively) and superiority of single-pRF model in control group under central and (jittered) fixation conditions (mean VE $\pm$ SEM for the above mentioned models (i–iv) in C1: (i) 57.01% $\pm$0.18, (46.69% $\pm$0.15), (ii) 43.58% $\pm$ 0.16, (37.91% $\pm$ 0.11), (iii) 30.97% $\pm$ 0.17, (33.43% $\pm$ 0.13), (iv) 46.27% $\pm$ 0.19, (39.8% $\pm$ 0.16 0.16), and in C2 (i) 62.23% $\pm$ 0.21, (60.31% $\pm$ 0.22), (ii) 50.99% $\pm$ 0.18, (49.96% $\pm$ 0.18), (iii) 38.94% $\pm$ 0.18, (38.37% $\pm$ 0.17), (iv) 48.95% $\pm$ 0.20, (47.86% $\pm$ 0.19); Figure 6.4 a).
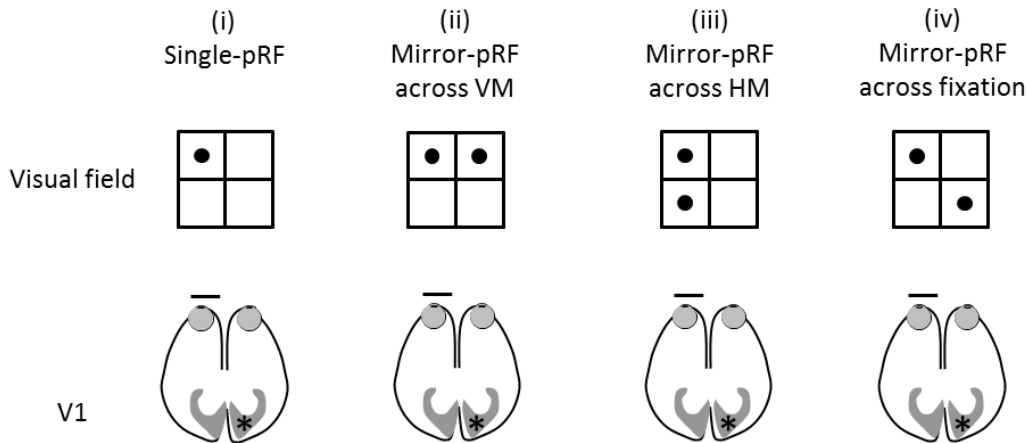

Figure 6.2: **Schematic representation of the pRF models**. A given location in the visual field is shown by a black solid circle ($\bullet$) and the corresponding region of V1 is expressed by an asterisk ($*$). (i) in single-pRF model, a specific point in the visual field is represented on a given region of the contralateral hemisphere. (ii) in mirror-pRF model across VM, two mirror-symmetrical locations in left and right hemifields are represented on a given cortical location. (iii) in mirror-pRF model across HM, mirror-symmetrical locations in upper and lower contralateral hemifield are represented on a given cortical location. (iv) in mirror-pRF model across fixation, two mirror-symmetrical locations across fixation (e.g. left upper and right lower hemifields) are represented on a given cortical location. It should be noted that only mirror-pRF model across VM has been described before (Fracasso et al., 2016; Hoffmann et al., 2012). Albeit theoretically possible, the other mirror-pRF models have not been reported yet. Adapted from (Ahmadi et al., 2019).

Furthermore, the relationship between pRF size and eccentricity plotted in Figure 6.4 b demonstrated that the mirror-pRF model across VM resulted in smaller receptive field sizes in both FHONDA participants. The increase of pRF sizes estimated by the single-pRF model is likely due to the failure of this model to discriminate two mirror-symmetrical locations in the visual field. Consequently, the model has to cover them into

a large single pRF. It is also plausible that the increased pRF sizes of the single model may cause the overall small difference in variance explained between the mirror-pRF model across VM and single-pRF model in FHONA observed in Figure 6.4 a. To assess this
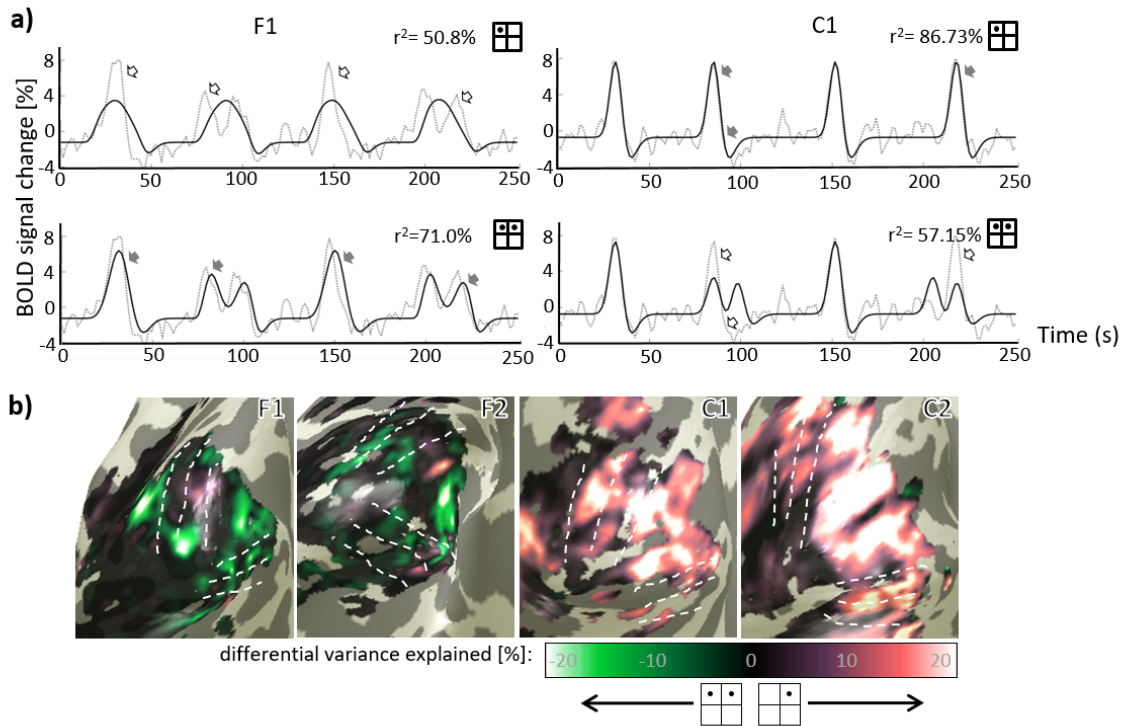

Figure 6.3: **Comparison of the pRF models**. **a)** pRF model fits in a given voxel of V1 in F1 and C1. The fMRI time-series (gray dashed lines) are fitted with single-pRF model and mirror-pRF model across VM (solid black lines). The open black and solid gray arrows indicate missed and captured fluctuations of the BOLD signal by the two models. The mirror-pRF model across VM yields a better fit in F1 and vice versa in C1. **b)** The difference in percent variance explained of the two models projected on the cortical surfaces of F1, F2 and the two controls. The mirror-pRF model across VM outperforms the single-pRF model in both FHONDA patients. In contrast, the single-pRF model prevails in controls. Adapted from (Ahmadi et al., 2019).

assumption, the two models were compared with identical parameters. First, fMRI time series were fitted with mirror-pRF model across VM. Afterwards, the single-pRF model was run based on the pRF parameters i.e. (x, y and σ) extracted from the mirror-pRF model. As depicted in Figure 6.5, the mirror-pRF model across VM exceeded its identical single counterpart in both FHONDA patients (mean VE $\pm$ SEM in F1: 60.39% $\pm$ 0.3053 vs 52.77% $\pm$ 0.3027 and F2: 59.13% $\pm$ 0.2275 vs 54.43% $\pm$ 0.2675). In addition, a single-pRF model was fitted to the time series and then compared to a mirror-pRF model across VM whose parameters were taken from it. Only a marginal decrease in the variance explained by the mirror-pRF model across VM was observed when comparing the two models (mean VE $\pm$ SEM in F1: 58.85% $\pm$ 0.3090 vs 58.44% $\pm$ 0.2990 and F2: 58.41% $\pm$ 0.2426 vs 57.18% $\pm$ 0.2284 0.2284). Taken together, the superiority of mirrored-pRF model across VM in FHONDA is evident for relatively small pRFs.
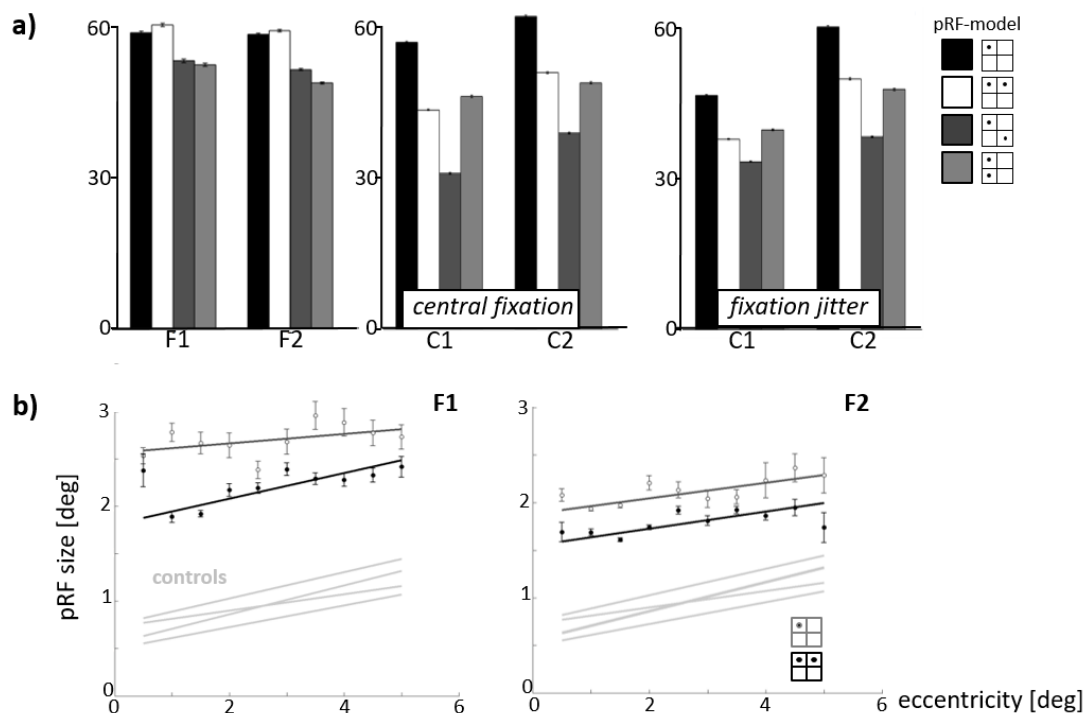
Figure 6.4: **Comparison of the pRF models**. **a)** The explanatory power of all pRF-models. The mean variance explained $\pm$ SEM for fMRI responses in V1 is shown for (i) single-pRF model and mirrored-pRF models across (ii) VM, (iii) fixation and (iv) HM for FHONDA and control participants under static fixation and fixation jitter conditions. While the single-pRF model explains most of the variance in controls, the variance explained is higher for the mirror-pRF model across VM in FHONDA. **b)** The relation between pRF size and eccentricity in V1 for FHONDA (estimated by single- and mirror-pRF model across VM) and controls (estimated by single-pRF model). Increased pRF sizes in FHONDA for the single-pRF model indicates that the inadequacy of this model is compensated by enlargement of pRF size. Adapted from (Ahmadi et al., 2019).
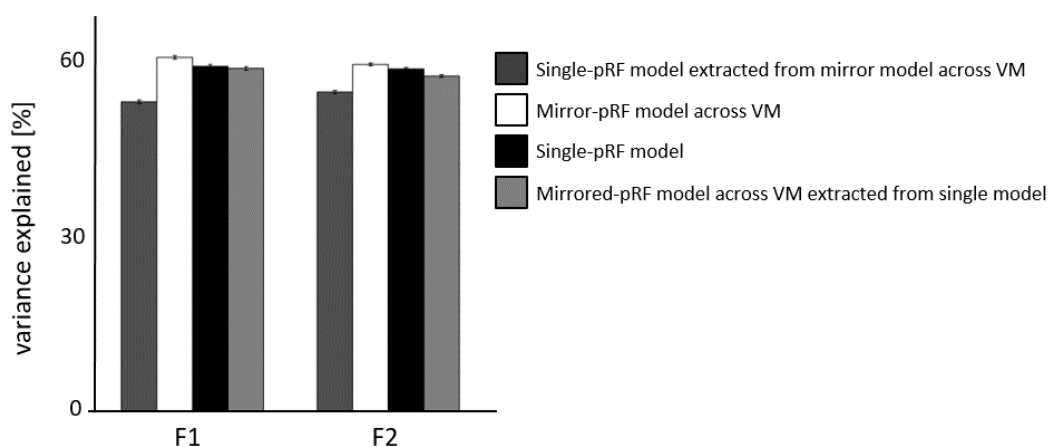

Figure 6.5: **Comparison of the pRF models with identical parameters in F1 and F2**. Mirror-pRF model across VM prevails the single-pRF model whose parameters are extracted from it. In contrast, only a trivial drop in the variance explained is observed when the mirror-pRF model across VM is fed with the parameters of the single-pRF model. Reprinted from (Ahmadi et al., 2019).

The analysis of bilateral pRF mapping also revealed orderly eccentricity and polar angle maps in FHONDA that were confined to the hemisphere contralateral to the stimulated eye, supporting the notion that opposing hemifields were represented as a cortical overlay of mirror-symmetrical positions of the visual field in FHONDA. Figure 6.6 represents the retinotopic maps of early visual areas in the two FHONDA and one control participants. The maps were obtained with the mirror-pRF model across VM for FHONDA and with the single-pRF model for the control. The cortical mapping observed in F2 indicated an eccentric shift of symmetry axis by 1.5°, presumably due to eccentric fixation associated with immature foveal development (see Figure 6.7). As such, the pRF models were re-calculated for F2 to take this shift into account. It should be noted that the data presented in Figures 6.3 - 6.6 and 6.9 for F2 have been corrected for this effect. As a sanity check, the same shift of symmetry axis was applied in controls and the pRF models were recomputed. The single-pRF model still prevailed in controls, verifying that the outperformance of mirror-pRF model across VM in F2 was not due to the shift of the symmetry axis (Figure 6.8).

As for bilateral stimulation, the representations of both the contra- and ipsilateral visual hemifields were organized as orderly eccentricity and polar angle maps confined to the hemisphere contralateral to the stimulated eye (Figure 6.9). It should be mentioned that for hemifield stimulation, only the single-pRF model was utilized in all participants since the voxels are only driven by a single pRF i.e. the stimulated visual hemifield.
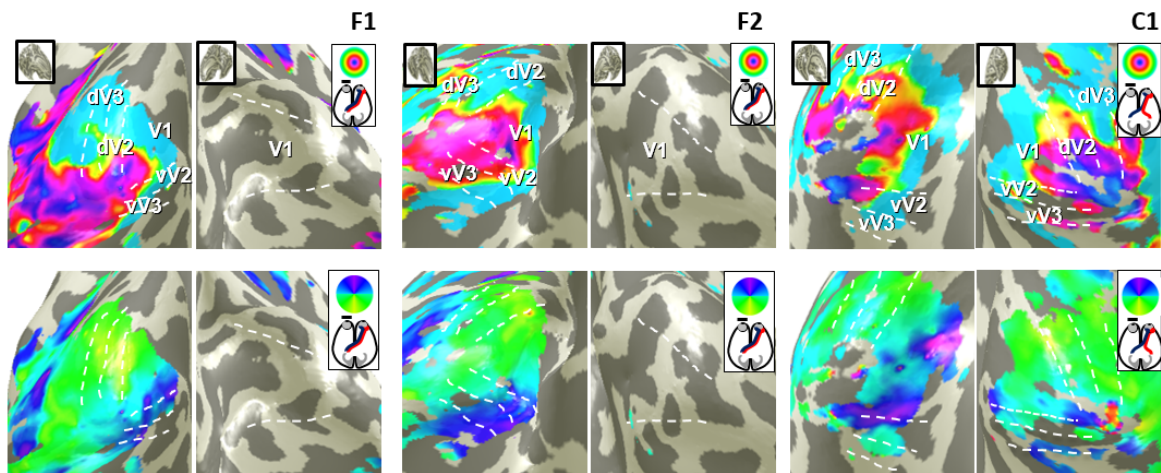
Figure 6.6: **Retinotopic maps on the inflated occipital cortex in the two FHONDA patients and one control participant under bilateral stimulation**. In control participant (C1), bilateral stimulation results in bilateral eccentricity (top row) and polar angle (bottom row) maps while in both individuals with FHONDA (F1 & F2) the maps are confined to the hemisphere contralateral to the stimulated eye. Note that the maps were obtained based on mirror-pRF model across VM in FHONDA and the single-pRF model for the control. Reprinted from (Ahmadi et al., 2019).
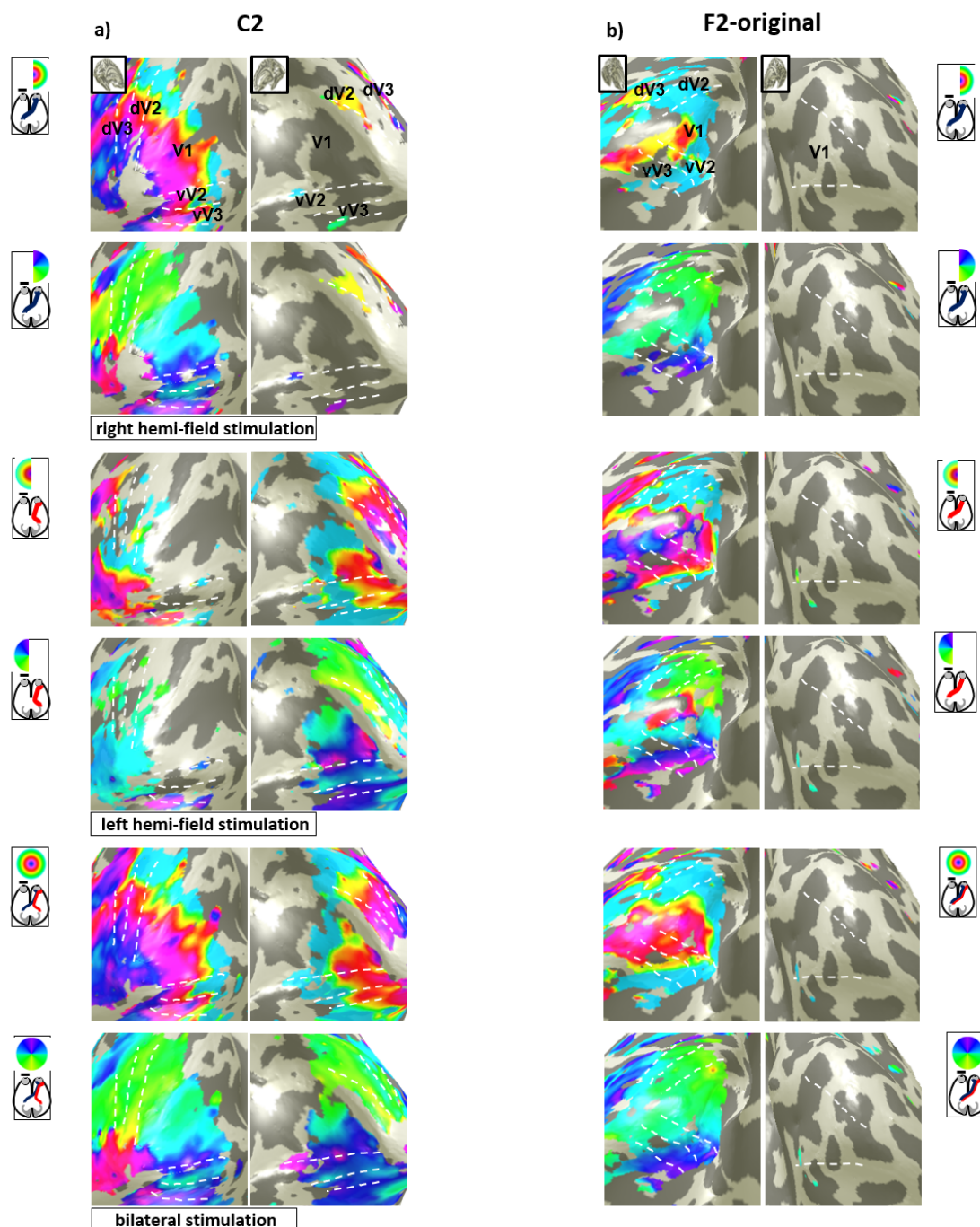
Figure 6.7: **Visual field maps for all three stimulation conditions in second ontrol participant, C2, (a) and F2 without shift (b)**. The systematic asymmetry observed in eccentricity and polar angle maps of F2 is probably due to an eccentric fixation of approximately 1.5° induced by foveal hypoplasia. Except for bilateral stimulation in F2 which was obtained by mirror-pRF model across VM, the rest of the maps were calculated with the single-pRF model (see Methods and Results). Note that although the maps are predominantly projected onto the hemisphere contralateral to the stimulated hemifield (top and middle panels) in C2, some residual bilateral representations (especially of the vertical meridians and fovea) is observed, as reported previously (Hoffmann et al., 2003; Tootell et al., 1998). Reprinted from (Ahmadi et al., 2019).
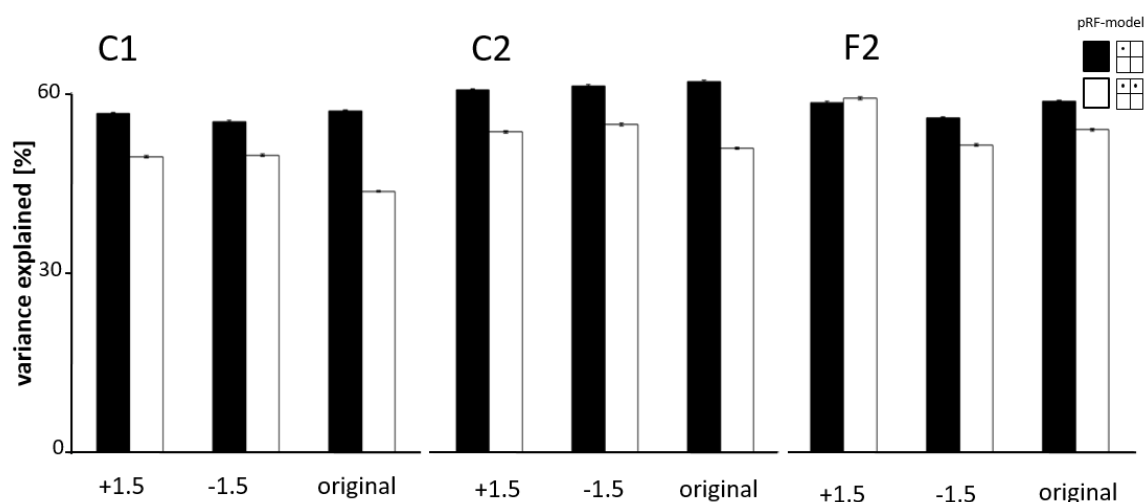
Figure 6.8: **Comparison of mirror-pRF model across VM and single-pRF model in F2 and the two controls (under static fixation) for three different conditions i.e. shifting the stimuli by** $+1.5°$**,** $−1.5°$ **and** $0°$ **('original').** Despite a slight rise in variance explained by the mirror-pRF model across VM in controls, it does not surpass the single-pRF model in any condition. In F2, however, the variance explained by the mirror-pRF model across VM is highest only when the stimuli are shifted by $+1.5°$. Reprinted from (Ahmadi et al., 2019).

Figure 6.9: **Retinotopic maps on the inflated occipital cortex in the two FHONDA patients and one control participant under the right (a) and left (b) hemifield stimulation.** In both FHONDA patients, the eccentricity (1st and 3rd rows) and polar angle (2nd and 4th rows) maps are confined to the hemisphere contralateral to the stimulated eye regardless of

the stimulated hemifield whereas in control participant, the maps are projected onto the hemisphere contralateral to the stimulated hemifield. Despite the predominance of contralateral activation in C1, residual representation of the vertical meridians is observed on the hemisphere ipsilateral to the stimulated hemifield (see also C2 in Figure 6.7). Reprinted from (Ahmadi et al., 2019).

6.4   Discussion

In the present study, the first evidence on the nature of the organization of the visual cortex in FHONDA is provided. Both bilateral and hemifie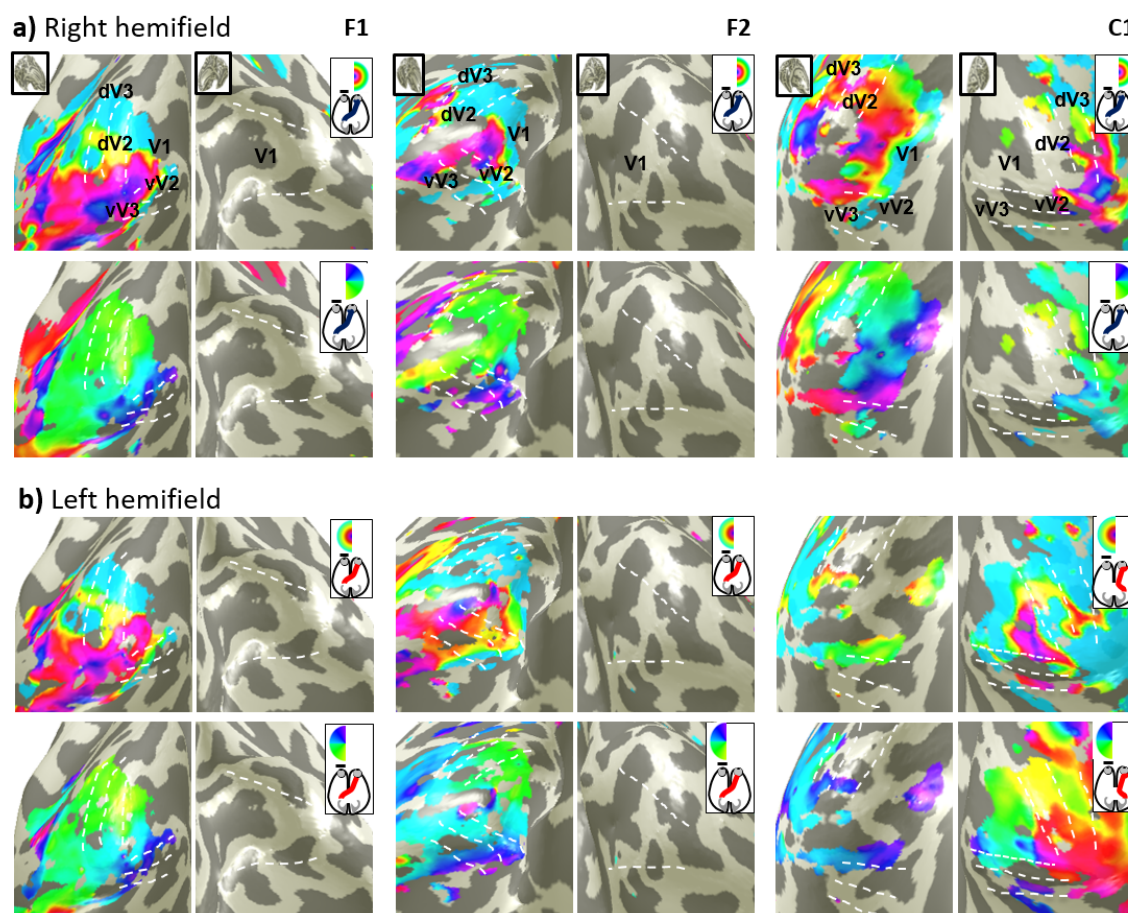ld stimulations in FHONDA participants indicate overlapping visual field maps confined to the hemisphere contralateral to the stimulated eye. As a result, visual field locations that are mirrored along the vertical meridian are co-localized in the occipital cortex.

6.4.1   Comparing FHONDA and other visual pathway abnormalities

The observed mapping in FHONDA implies largely unaltered geniculo-striate connections which has been postulated for other visual pathway abnormalities such as albinism, achiasma, and hemihydranencephaly (Hoffmann and Dumoulin 2015). This conservative projection pattern results in an intermingled representations of the ipsi- and contralateral hemifields in the primary visual cortex which give rise to hemifield dominance domains that are reminiscent of ocular dominance domains in a normal visual system (Guillery et al., 1984; Olman et al., 2016). The resolution of the current study does not allow the differentiation of these domains, rather they are displayed as a retinotopic overlay of opposing hemifields (Hoffmann and Dumoulin 2015). The similarity of the cortical organization in FHONDA and other congenital visual pathway disorders indicate lack of large-scale plasticity of geniculo-striate connections, whereas more sub-cortical plasticity is available in some non-primate animal models (Hoffmann and Dumoulin 2015; Hoffmann et al., 2003).

6.4.2   The difference between FHONDA and albinism

Even though foveal hypoplasia and enhanced crossing of the optic nerve fibers are common characteristics of FHONDA and albinism, there is a fundamental difference between the two disorders. Albinism is associated with hypopigmentation of either the eyes or the eyes, hair and skin caused by abnormal melanogenesis, while the absence of pigmentation deficits is a major criterion in the diagnosis of FHONDA. The misrouting of the optic nerves in albinism is believed to be related to the reduction of melanin formation. Previous studies have shown that retinal level of a melanin precursor known as L-DOPA is decreased during fetal development in albinism. This delays the differentiation of the ganglion cells and leads to underdevelopment of uncrossed projections at the optic chiasm (Hoffmann and Dumoulin 2015; Ilia and Jeffery 1999; Jeffery 2001). Lack of pigmentation deficits in

FHONDA suggests that the underlying mechanisms of optic nerve misrouting might be independent of melanin and L-DOPA levels.

Furthermore, the degree of misrouting in albinism varies between 2° to 15° of eccentricity. Beyond that, the projection of temporal fibers reverts to normal pattern i.e. projecting to the ipsilateral hemisphere. In contrast, our results demonstrate that there is no residual normal representation of temporal fibers in FHONDA (see Figure 6.10). This might, within the limits of stimulus size in the present study (6° stimulus radius), indicate that the uncrossed projections at the optic chiasm are completely blocked in FHONDA. In conclusion, further research is required to determine whether distinctive mechanisms are involved in FHONDA and albinism.
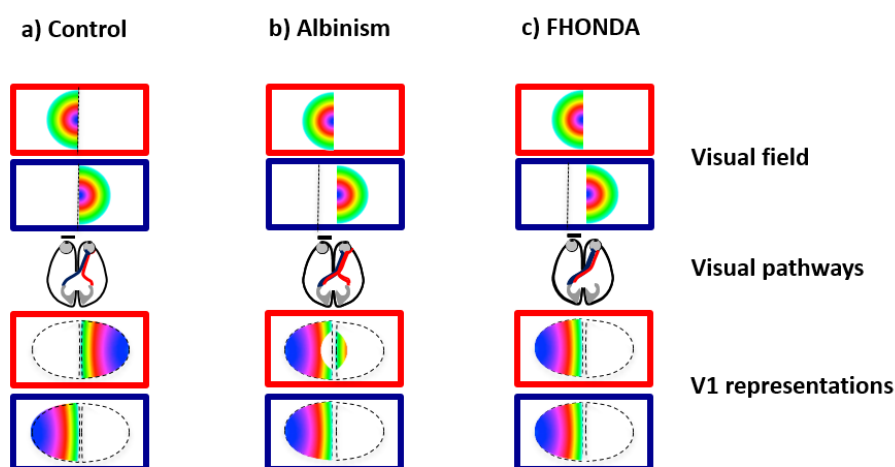

Figure 6.10: **Schematic representation of optic nerve projections and visual field maps in V1 for control, albinism and FHONDA**. **a)** Control. Normally, nasal retinal afferents (blue) of the right eye cross the chiasm and project to the contralateral hemisphere (left hemisphere; middle panel), while temporal retinal axons (red) stay uncrossed and project to the ipsilateral hemisphere (right hemisphere; middle panel). Consequently, the retinotopic maps (only eccentricity maps shown here) are represented on V1 that is contralateral to the respective hemifield. **b)** Albinism. The line of decussation (dotted line) is shifted into the temporal retina instead of coinciding with vertical meridian due to an enhanced crossing of the temporal retinal fibers to the contralateral hemisphere. This leads to the superimposed representation of opposing hemifields for the part of the temporal retina that projects contralaterally, i.e. up to the line of decussation. Beyond that, the representation of temporal fibers reverts to the normal pattern (here, to the right hemisphere). **C)** FHONDA. The enhanced crossing of temporal afferents results in a cortical overlay of both contra- and ipsilateral hemifields on the contralateral V1. However, unlike albinism, no normal residual ipsilateral projection is observed, indicating that the entire temporal fibers might cross the chiasm and project contralaterally. Reprinted from (Ahmadi et al., 2019).

6.4.3 Visual perception

As for other congenital visual pathway abnormalities, both FHONDA participants had reduced visual acuity, nystagmus, strabismus and absent stereopsis. While reduced visual

acuity is related to foveal underdevelopment and nystagmus, lack of stereo vision is linked to the misrouting of the optic nerves that obstructs integration of binocular input. Despite the atypical overlaid representation of the opposing hemifields, major aspects of visual processing remain intact in FHONDA. In line with previous reports in albinism (Klemen et al., 2012) and achiasma (Bao et al., 2015; Hoffmann et al., 2012; Victor et al., 2000), the FHONDA participants of the current study made effective use of their vision in daily life, including reading. Although no behavioral testing was performed, the everyday behavior of the FHONDA participants reveal no inter-hemifield confusion caused by superimposed representation of the opposing hemifields, suggesting that the two mirror-symmetrical pRFs are functionally independent. This suggests the presence of efficient adaptive mechanisms that make the erroneous visual input available for visual perception.

6.4.4 Importance for clinical applications and basic neuroscience

Consistent with previous electrophysiological studies (Al-Araimi et al., 2013; Poulter et al., 2013; van Genderen et al., 2006), our fMRI-results confirm and extend optic nerve misrouting in FHONDA, a syndrome clearly distinct from albinism as there is no deficit in melanin biosynthesis. The enhanced crossing of the optic nerves in FHONDA is of significant clinical importance since it can no longer be considered as exclusive to albinism. Diagnosis of uncertain cases of albinism e.g. with mild hypopigmentation, should therefore not be limited to the detection of misrouted optic nerves via visual evoked potentials (VEPs). Secondary symptoms such as fine pigmentation deficits manifested by iris translucency must also be examined in these cases. Due to the small number of identified patients with FHONDA, the diagnostic problem might seem to be of little importance. Nevertheless, given the novelty of the FHONDA syndrome and the unknown number of previously misdiagnosed patients, the actual number of affected individuals is likely much higher.

In conclusion, our direct evidence of abnormal mapping in FHONDA accentuates the importance of melanin-synthesis independent components required for the development of the human visual system, particularly the optic chiasm. Moreover, the similarity of the cortical organization in FHONDA and other congenital visual pathway abnormalities demonstrates that interplay of subcortical stability and intra-cortical plasticity is a general developmental mechanism in human visual cortex.

Chapter 7

Triple hemifield input to the visual cortex in an individual with chiasma hypoplasia

The work presented in this chapter is currently submitted for publication:

Ahmadi, K., Fracasso, A., Puzniak, R.J., Gouws, A.D., Yakupov, R., Speck, O., Kaufmann, J., Pestilli, F., Dumoulin, S.O., Morland, A.B., Hoffmann, M.B. Triple visual hemifield maps in optic chiasm hypoplasia.

It has also been published in abstract form in the following conference proceedings:

Ahmadi, K., Fracasso, A., Puzniak, R.J., Gouws, A.D., Yakupov, R., Speck, O., Kaufmann, J., Pestilli, F., Dumoulin, S.O., Morland, A.B., Hoffmann, M.B. (2019). Triple hemifield input to the visual cortex in a patient with chiasmal hypoplasia. Organization for Human Brain Mapping (OHBM), Rome, Italy.

Ahmadi, K., Fracasso, A., Gouws, A.D., Morland, A.B., Dumoulin, S.O., Hoffmann, M.B. (2017). Functional organisation of the visual cortex in a unique case of achiasma. Society for Neuroscience (SfN), Washington, D.C., USA.

7.1   Introduction

The two superimposed retinotopic maps of opposing visual hemifields described in chapter 6 and section 2.2 prompt the question of whether the visual cortex is capable of hosting more maps. At the mesoscopic scale, these two superimposed maps are interdigitated in V1, forming hemifield dominance domains that are reminiscent of ocular dominance domains in a normal visual system (Olman et al., 2016). The mechanism of reassigning ocular dominance domains alone would suggest that only two inputs can be accommodated, either two representations of the contralateral visual hemifield via binocular input in normal vision or two representations of opposing hemifields via monocular input in congenital chiasmal abnormalities. Thus, any additional input would necessarily need to engage further plastic mechanisms to establish a useful visual representation. In this chapter, the cortical organization of the visual field maps was determined in an individual with an extremely rare type of chiasma hypoplasia to address the limits of plasticity in V1 and beyond. Three types of investigations were performed using 3 and 7 Tesla MRI: (i) diffusion weighted imaging (DWI) to specify the projection error of the optic nerves at the optic chiasm, (ii) pRF mapping (Ahmadi et al., 2019; Dumoulin and Wandell 2008) to determine the cortical layout of the visual field maps, and (iii) ultra-high resolution fMRI to examine the cortical fine-grain structure. Our results demonstrate that three hemifield maps can be accommodated within a single V1. We propose that mechanisms of developmental plasticity that are exceeding the simple reassignment of ocular dominance domains to hemifield dominance domains enable these three maps to be hosted in V1.

7.2   Methods

The measurements were performed at two sites. The participant with chiasma hypoplasia ('CHP') was first scanned at Magdeburg University, Germany, at the age of 24. In two consecutive days, she underwent ultra-high resolution fMRI at 7 T and DWI scanning sessions at 3 T. Due to the limited availability of CHP, pRF mapping data were acquired two years later at York Neuroimaging Center, UK, at 3 T.

7.2.1   Case description

CHP was a 26-year-old female. Her best-corrected decimal visual acuity was 0.63 for the dominant right eye and 0.25 for the left eye. She had mild vertical nystagmus, strabismus [alternating strabismus, esotropia (5°), and vertical deviation (7°) with alternating suppression of each eye] and no stereoscopic vision. Humphrey-like visual field testing revealed normal visual fields in both eyes. Decussation anomalies were confirmed by VEPs, and T1-weighted MRI at the age of 22. She reported an otherwise normal developmental and medical history and there was no family history of ophthalmological or neurological disorders.

7.2.2   Participants

In addition to CHP, 12 respective control participants were also included in the current study. The first 4 controls (C1 – C4) took part in a pRF mapping session at 3 T while the other 7 controls (C5 – C11) participated in the DWI sessions. The last control participant (C12) underwent both submillimeter fMRI and DWI at 7 and 3 T. All the experiments on controls were conducted in Magdeburg. Informed written consent was obtained from all participants prior to the study initiation. The procedures followed the tenets of the declaration of Helsinki and the respective protocols were approved by the ethical committees of the University of Magdeburg and York Neuroimaging Centre.

7.2.3   Ultra-high resolution fMRI

Visual stimulation

Visual stimuli were presented by back-projection onto a screen with a resolution of 1920 x 1080 pixels and viewed at a distance of 100 cm via an angled mirror. Presentation software package (Neurobehavioral Systems, Berkeley, CA, USA) was used to control stimulus presentation. The stimuli extended $\pm$ 12.9° x $\pm$ 7.4° of visual angle from the center of the screen and comprised bilateral, contrast reversing (8 reversals per second) black and white checkerboards with 24 segments and 26 rings (mean luminance 62 cd/m^2, contrast 99%). A block design, alternating between the two eyes was selected. It consisted of 14 checkerboard presentation blocks (7 blocks per eye), each of which lasted for 12 s and was followed by a rest block (mean luminance gray background) with the same duration. The presentation blocks were preceded by an additional rest block of 12 s for dummy stimulation. Participants wore a custom-made manually operated shutter that allowed monocular viewing through either the left or right eye. They fixated a central fixation cross, which changed its color one second after initiation of each rest block, lasting for 23 s (11 s of the rest block plus 12 s of the next presentation block). The participants were requested to occlude the right eye and view the stimuli with the left eye for a green fixation cross, and vice versa for a red one. An MRI-compatible camera was used to view the dominant eye, to ensure that the participants were doing the task correctly.

MRI acquisition

For functional imaging, T2*-weighted images were acquired using a 2D gradient-echo EPI sequence at a 7 Tesla whole body MRI scanner (Siemens Healthineers, Erlangen, Germany) with a 32 channel head coil (Nova Medical, Wilmington, MA). The acquisition parameters were as following: TR / TE = 3000 / 22 ms, flip angle = 90°, FOV = 169 (right-left) x 130 (anterior-posterior) x 27 (feet-head) mm^3, acceleration factor (r) = 4 with GRAPPA reconstruction, phase-encoding direction = right-left, phase partial Fourier = 5/8, bandwidth (BW) = 1086 Hz/px, echo-spacing = 1.13 ms, and voxel size = 0.65 x 0.65 x 0.65 mm^3. Forty-one oblique axial slices were acquired parallel to the calcarine sulcus for a duration of 348 s with 116 time frames, of which the first four were discarded. Foam padding was used to minimize head motion. Four runs of bilateral stimulation were performed for each participant in a single session. High-resolution anatomical volume was

obtained using a 3D T1-weighted MPRAGE sequence (TR / TE / TI = 2500 / 2.76 / 1050 ms, total duration = 14:14 min, flip angle = 5°, FOV = 350 x 263 x 350 mm^3, and voxel size = 0.65 x 0.65 x 0.65 mm^3). In addition, a proton density weighted volume without the inversion module (identical parameters except for TR = 1820 ms and total duration = 5:33 min) was acquired to correct for receive coil biases (Van de Moortele et al., 2009).

Data analysis

To obtain an inhomogeneity corrected anatomical image, the T1-weighted MPRAGE reference volume was divided by the proton density weighted volume. Gray and white matter (GM/WM) were segmented based on the resulting anatomical volume in MIPAV (https://mipav.cit.nih.gov/) using the TOADS/CRUISE algorithm (Bazin and Pham 2007; Han et al., 2004). Manual editing was performed in ITK-GRAY (https://web.stanford.edu/group/vista/cgi-bin/wiki/index.php/ItkGray) to minimize the segmentation error. An equi-volume distance map was employed (Waehnert et al., 2014) to build a coordinate system along cortical depth, taking the local curvature into account. The functional data were corrected for motion artifacts and spatial distortion using MCFLIRT function of FSL (https://www.fmrib.ox.ac.uk/fsl) and a point spread function (PSF) mapping method (In and Speck 2012) respectively. Motion and distortion corrected data were then analyzed using AFNI (https://afni.nimh.nih.gov/afni). Time series were averaged across repetitions for each participant to increase the signal-to-noise ratio (SNR). Afterwards, the averaged functional volume was aligned to the T1 weighted anatomical volume using an affine transformation. The alignment was performed in three steps: First, the T1-weighted anatomy and the averaged EPI were clipped in the anterior-posterior direction, leaving only the occipito-temporal cortex. A good starting point was provided by centering the functional volume on the anatomy using their respective centers of mass. Next, the averaged functional volume was affinely aligned to the T1 weighted volume via AFNI's `'align_epi_anat.py'` with the local Pearson's coefficient (LPC) cost function (Saad et al., 2009), using the two-pass option. This procedure blurs the functional volume and initially allows for a large rotation and shift, then refines the alignment by an affine transformation. Finally, the resulting alignment was further improved via 3dAllineate, using the one-pass option. In this step, the functional volume is not blurred. Only a small amount of shift and rotation is allowed, using an affine transformation that is obtained by concatenating the transformation matrices generated in previous steps (Fracasso et al., 2018; Klein et al., 2018).
A general linear model (GLM) was used to analyze the functional data. For each voxel, percentage of BOLD signal changes to stimulation of the left and right eye was estimated via 3dDeconvolve function of AFNI. Nuisance regressors were modeled using polynomials up to the second order to remove any linear and quadratic trends. The GLM analysis was performed on the native EPI space. The obtained GLM maps (T-maps and beta-coefficient-maps; T = 1.98, p = 0.05, uncorrected) were interpolated to the T1-weighted space via nearest-neighbor interpolation, using the affine transformation matrix estimated in the alignment step. For each of the cortical layers, a 3D mesh was generated using AFNI's IsoSurface function. To assess the presence of ocular dominance domains

structures in the data throughout the cortical depth, eleven ROIs were selected on the cortical surface of the deep, middle and superficial layers and were mapped back onto volume dataset via '3dSurf2Vol' function for further analysis. The first ROI (ROI_{signal}) was drawn in the banks of calcarine sulcus where the ocular dominance domains should be located. The remaining ten ROIs ($ROIs_{noise}$) were drawn in different regions of the occipito-temporal cortex where there should be no ocular domains. The selectivity index was then derived (Kemper et al., 2018; Olman et al., 2016) from the voxels within these ROIs. It was defined as a measure for eye preference, i.e. the difference between the responses to left ('L')and right ('R') eye stimulation divided by sum of the responses to visual stimuli: $I_{selectivity} = |(L - R)/(L + R)|$. The segregation of the binocular input was quantitatively evaluated by voxelwise comparison of the selectivity between ROI_{signal}, and each ROI_{noise}, using receiver operating characteristic (ROC) analysis. Furthermore, the selectivity of ROI_{signal} was compared to the average selectivity of the ten $ROIs_{noise}$ with identical analysis.

7.2.4 Diffusion-weighted imaging

MRI acquisition

DWI data were acquired using a 3 Tesla Magnetom Prisma scanner (Siemens Healthineers, Erlangen, Germany) with the 64 channel head coil. MRI acquisition was initiated by a localizer scan, followed by a T1-weighted MPRAGE scan and two diffusion-weighted scans. All data were collected during a single scanning session. The T1-weighted volume was collected in sagittal orientation using a 3D-MPRAGE sequence (TE / TR = 4.46 / 2600 ms, TI = 1100 ms, flip angle = 7°, resolution = 0.9 x 0.9 x 0.9 mm^3, FoV = 230 x 230 mm^2, image matrix: 256 x 256 x 176, acquisition time (TA) = 11:06 min). The first Diffusion-weighted scan was acquired with Echo-Planar Imaging (EPI) sequence with the following parameters: b-value = 1600 s/mm^2, voxel size = 1.5 x 1.5 x 1.5 mm^3, phase-encoding direction = anterior to posterior, FoV = 220 x 220 mm^2, TR / TE = 9400 / 64.0 ms and TA = 22:24 min. Scanning was performed with 128 gradient directions, thus the obtained diffusion-weighted data can be described as High Angular Resolution Diffusion Imaging (HARDI) data (Tuch et al., 2002). Gradient tables were generated using E. Caruyer's tool (http://www.emmanuelcaruyer.com/q-space-sampling.php) for q-space sampling (Caruyer et al., 2013). Diffusion-weighted volumes were evenly intersected by 10 non-diffusion weighted volumes for the purpose of motion correction. The second diffusion-weighted scan was acquired with identical parameters except for reversed phase-encoding direction in comparison to previous scan i.e. posterior to anterior direction. Acquisition of two diffusion-weighted scans with opposite phase-encoding directions enhances correction of geometrically induced distortions (Andersson et al., 2003) and improves the SNR of the total DWI data.

Data analysis

Denoising of the DWI data and removal of Gibbs ringing were performed with MRtrix 3.0 (http://www.mrtrix.org/). FSL (https://fsl.fmrib.ox.ac.uk/fsl/fslwiki) was employed for the correction of susceptibility-induced geometric distortions, eddy current distortions,

and motion artifacts. The bias field in the DWI data was corrected using ANTS (http://stnava.github.io/ANTs/). Afterwards, DWI data were co-registered to the T1-weighted volume, which was aligned beforehand to Anterior Commissure – Posterior Commissure line, via mrDiffusion (https://github.com/vistalab/vistasoft/tree/master/mrDiffusion). The T1-weighted volume was automatically segmented using FIRST function of FSL. Subsequently, manual editing was performed to mitigate segmentation errors in the region of the optic chiasm. Each voxel of the preprocessed DWI data was modelled using Constrained Spherical Deconvolution (CSD) approach (Tournier et al., 2008), which is particularly sensitive when resolving populations of crossing fibers, similar to those observed in the optic chiasm, and benefits from the high angular resolution of HARDI data. The application of the CSD model involved the estimation of single fiber response function with Tournier's algorithm (Tournier et al., 2013) for maximum harmonic order (Lmax = 6) and the estimation of fiber orientation distribution functions (Jeurissen et al., 2014) or 3 different maximum harmonic orders i.e. Lmax = 6, 8 and 10. Four regions of interest (ROIs) were manually drawn on the T1-weighted volume, two covering cross-sections of the two optic nerves, and the other two covering cross-sections of the two optic tracts. The ROIs were placed as close to the optic chiasm as possible, but did not intersect it. Each ROI had a width of 3 voxels (anterior-posterior) to assure proper streamline termination during tractography. Fiber tracking was performed between the ROIs of the two optic nerves as seeds and the ROIs of the two optic tracts as targets, resulting in 4 connectivity pairs (2 ipsilateral and 2 contralateral fiber bundles). Tracking was done in two directions i.e. from seed to target ROI and backwards to ensure the indifference of the results to direction of tracking. The corresponding generated connectivity pairs were subsequently merged together. The tracking employed an ensemble tractography (ET) framework (Takemura et al., 2016), where tracking is performed several times, each time for a different set of parameters. As such, the bias in the outcome tracts, caused by parameter selection, is avoided. The tracking was performed with the probabilistic tracking algorithm iFOD2 (Tournier et al., 2010) using unique combinations of 2 different fractional anisotropy (FA) thresholds (FA = 0.04 and 0.08), 3 maximum curvature angles (30°, 45°, 60°) and 3 CSD models estimated for different maximum harmonic orders (L_{max} = 6, 8, 10) for each of 139000 seeding attempts. Additionally, tractography employed an anatomically-constrained tractography (ACT) approach (Smith et al., 2012), which constrains tractography with anatomical priors derived from the anatomical image using white/gray matter, subcortical gray matter and CSF masks obtained with FSL's FIRST function. As a result of the tractography, 4 streamline groups corresponding to 4 distinct connectivity pairs were obtained. The proportion of streamlines in each group were subsequently used as an estimate of the connectivity strength in the optic chiasm.

7.2.5   pRF and CF modeling

Visual stimulation

Visual stimuli consisted of drifting bar apertures (stimulus size in York and Magdeburg = 11° and 9.5° radius, respectively), exposing a moving high-contrast checkerboard pattern (Dumoulin and Wandell 2008) at four different directions i.e. upward, downward, left and

right. The bars were presented to each eye separately within a mask, covering either the left or the right hemifields for stimulation of either the nasal or the temporal retina in separate experiments. Width of the bars subtended one-quarter of the stimulus radius. Each pass of the bars lasted for 30 s, followed by a mean luminance block (zero contrast) of 30 s. The stimuli were generated in Matlab (Mathworks, Natick, MA, USA) using the Psychtoolbox (Brainard and Vision 1997; Pelli 1997) and rear-projected onto a screen inside the magnet bore. In York, the participants viewed the screen at a distance of 57 cm via an angled, front-silvered mirror whereas the eye to screen distance in Magdeburg was 35 cm. Participants were required to fixate a centered dot and to report colour changes between red and green by means of a button press.

MRI acquisition

Identical 3 Tesla Prisma scanners (Siemens Healthineers, Erlangen, Germany) were used at both sites. At York neuroimaging center, functional T2*-weighted images were acquired with a 64 channel head coil (Nova Medical, Wilmington, MA). A total of 30 EPI slices were obtained within a FOV of 192 mm, with 3 x 3 x 3 mm^3 voxels (TR / TE = 1500 / 26 ms and flip angle = 80°). Each functional scan comprised 168 time frames, lasting for 252 s. The first eight time-frames (12 s) were removed to allow magnetization to reach a steady-state. Foam padding was used to minimize head motion. Additionally, a T1-weighted anatomical volume was acquired at a resolution of 1 x 1 x 1 mm^3 (TR / TE = 2500 / 42.26 ms and flip angle = 7°). Eight functional scans were obtained in a single session (4 per eye). The right eye was stimulated during the first 4 runs while the left eye was patched. The stimulation of each of the left and right hemifields was repeated twice in a counterbalanced manner. After a short break in the scanning, the left eye was stimulated while the right eye was occluded. The same stimulation procedure was performed for the left eye.

At Magdeburg University, functional images (TR/ TE = 1500 / 30 ms and flip angle = 70°) were acquired at a resolution of 2.5 x 2.5 x 2.5 mm^3 with 54 axial slices, using a 64 channel head coil. Every functional scan had 168 time frames (252 s). In addition, a high resolution whole-brain anatomical image (voxel size = 0.9 x 0.9 x 0.9 mm^3, TR / TE = 2600 / 4.46 ms, and flip angle = 7°) was obtained. Foam padding limited the head movements. In each session, left and right hemifield stimulation conditions were performed monocularly and repeated six times (three repetitions per hemifield).

Data analysis

The same analysis pipelines were used for data sets acquired in both sites. The T1-weighted anatomical volume was automatically segmented using the recon-all function of FreeSurfer (https://surfer.nmr.mgh.harvard.edu). The cortical surface was reconstructed at the white/gray matter boundary and rendered as a smoothed 3D mesh (Wandell et al., 2000). The MCFLIRT function of FSL was used for motion correction of the functional data. Motion corrected data were then analyzed using freely available Vistasoft software package for MATLAB (https://github.com/vistalab/vistasoft). Time series for the same conditions were averaged together for each participant to increase the SNR ratio. Afterwards, the averaged functional volume was co-registered to the

anatomical scan using a combination of Vistasoft and Kendrick Kay's alignment tools (https://github.com/kendrickkay/alignvolumedata). Visual areas were mapped using the pRF modeling (Dumoulin and Wandell 2008) which has been described in detail in sections 3.3 and 6.2.5. For all subsequent analysis including the derivation of the polar angle and eccentricity maps, required for the delineation of the visual areas, and the visualization on the inflated cortical surface, only the voxels were included whose pRF fits exceeded 15% of the variance explained.

The connective field parameters were estimated from the fMRI time-series, using CF modeling that predicts the neuronal activity in one brain area with reference to aggregate activity in another area (Haak et al., 2013). A detailed description of the model has been provided in section 3.4. Briefly, the BOLD response in each voxel of a target ROI, i.e. V2 or V3 was predicted with a symmetrical, circular 2D Gaussian CF model folded to follow the cortical surface of the source ROI, i.e. V1. The CF model was defined by two parameters i.e. Gaussian position and spread across the cortical surface. The optimal CF parameters were determined by minimizing the RSS between the predicted, and the observed time-series. For this purpose, many fMRI time-series predictions were generated by changing the CF positions across all voxel positions and Gaussian spread values on the surface of the source ROI. Best models were selected when the explained variance in the fMRI time-series survived a threshold of 15%.

7.2.6   Visual field testing

We simulated the Humphrey visual field testing based on Psychopy (https://www.psychopy.org/) on a calibrated CRT monitor (22-inch Mitsubishi 2070SB at 85 Hz). Background luminance was set to 10 cd/m^2, equal to 30 dB. Goldmann size III stimuli i.e., white circular patches (0.43° diameter) were displayed for 235 ms and placed at 54 locations according to the Humphrey 24-2 standard test. In addition, four stimuli were placed at 12, 15, 18, and 21 degrees into the temporal field along the horizontal meridian in order to capture the blind spot. The detection threshold was tested in both eyes with one-up-one down staircase procedure with a minimum of 30 trials per location. CHP was requested to respond within 800 ms of stimulus presentation. An initial adaptive staircase with 4dB / 2dB step sizes was used to coarsely estimate the threshold at 16 locations in the visual field (4 in each visual quadrant), starting at the maximum gun value. Subsequently, a second adaptive staircase with finer step sizes (minimum 0.25 dB) was used to more accurately find the threshold starting at a gun value of 25% of the maximum (35 cd/m^2).

7.3   Results

7.3.1   Atypical lateralization pattern revealed by ultra-high resolution fMRI data

Ultra-high resolution fMRI at 7 T was used to evaluate the cortical lateralization pattern in response to bilateral contrast reversing black and white checkerboards presented to

each eye separately. In a neurotypical visual system, bilateral stimulation of each eye leads to bihemispheric activation (Figure 7.1). In CHP, however, bilateral stimulation of the left eye yielded predominant responses on the ipsilateral occipital cortex i.e. on the left hemisphere, and only a marginal activation was observed on the contralateral hemisphere. In contrast, considerable bilateral activation was found during bilateral stimulation of the right eye, indicating that part of the nasal afferents decussate at the chiasm and project to the contralateral hemisphere i.e. left visual cortex (Figure 7.2). This revealed that the misrouting pattern in CHP is distinct from complete achiasma where bilateral stimulation results in complete ipsilateral activation.
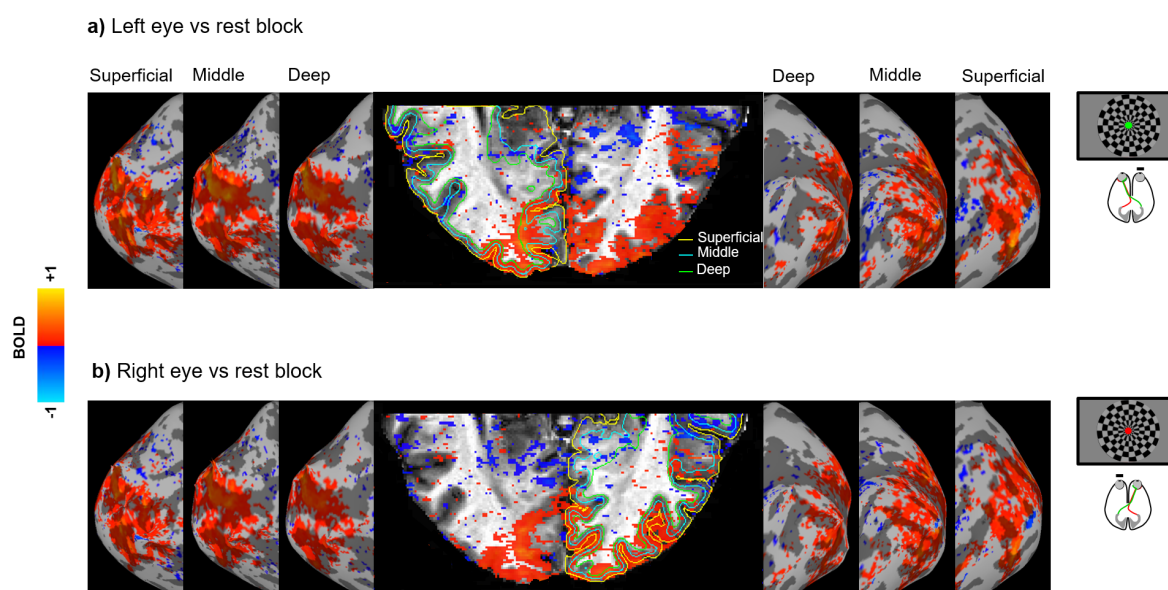

Figure 7.1: **Cortical response lateralization during bilateral stimulation of each eye in a control participant**. The cortical activation is projected onto a clipped anatomical volume and inflated cortical surfaces representing deep, middle and superficial layers. Both left **(a)** and right eye **(b)** stimulation vs rest elicit bilateral activation. The activation maps consist of signal amplitude expressed as β coefficient from the general linear model thresholded by cluster size and mean Student's T statistic (cluster = 20, threshold by T = 1.98, p = 0.05, uncorrected).

7.3.2 Optic nerve misrouting revealed by DWI

The above findings predicted that the proportion of crossing fibers of the right eye exceeds that from the left eye. We confirmed this prediction by the analysis of the DWI data obtained at 3 T for CHP and a cohort of 8 controls for comparison. The macro-structural properties of the optic nerves were quantified by computing the proportion of streamlines. Four ROIs were selected, one in each of the two optic nerves and one in each the two optic tracts, to identify streamlines connecting each optic nerve with the (i) ipsilateral and (ii) contralateral optic tract. The proportion of the streamlines projecting from the ipsilateral optic nerve to the ipsilateral optic tract was similar for the right and left optic nerve in both CHP (42% vs 58%) and controls (53% vs 47%). In contrast, the proportion of
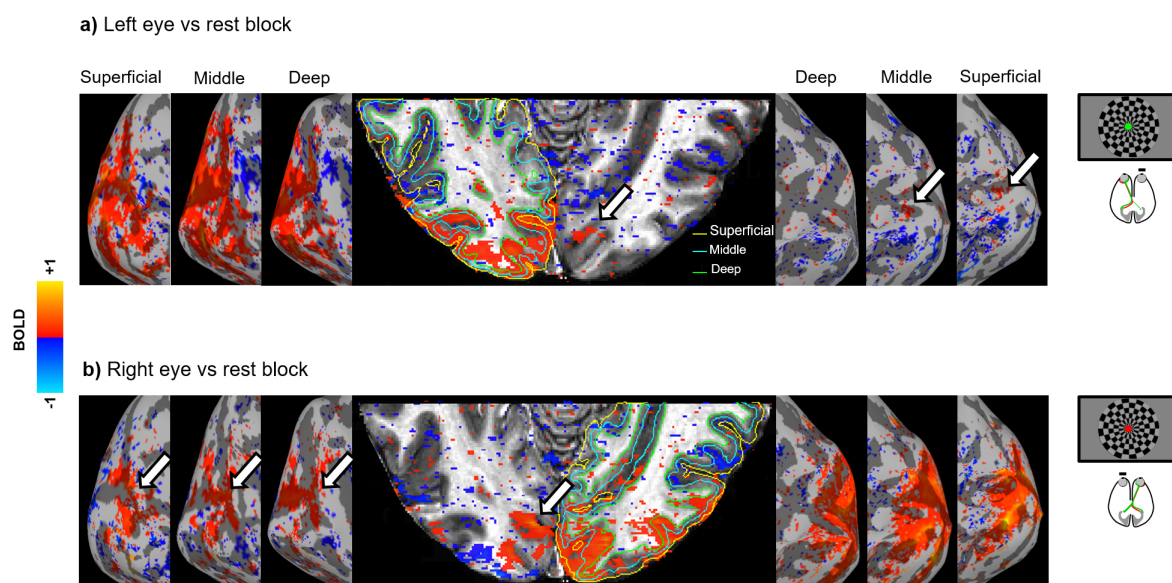
Figure 7.2: **Cortical response lateralization during bilateral stimulation of each eye in CHP**. The cortical activation is projected onto a clipped anatomical volume and inflated cortical surfaces representing deep, middle and superficial layers. **a)** Left eye stimulation vs rest elicits predominantly unilateral activation on the ipsilateral hemisphere with a small residual activation on the contralateral hemisphere, indicated by white arrows. **b)** Right eye stimulation vs rest elicits bilateral activation, i.e. on the ipsilateral hemisphere and also on part of the contralateral hemisphere (white arrows). Conventions as for Figure 7.1.

contralaterally projecting streamlines from the right optic nerve exceeded that from the left by a factor of three in CHP (73% vs 27%) but was balanced in the controls (49% vs 51%). This underscores the asymmetrical distribution of crossing afferents at the optic chiasm in CHP. A 3D rendering of the tracked streamlines is illustrated in Figure 7.3.

7.3.3 Three overlaid hemifield representations revealed by pRF mapping

Based on the response lateralization pattern observed in ultra-high resolution fMRI data, we speculated that a significant part of the visual cortex on the left occipital lobe receives triple input from three hemiretinae, from the two hemiretinae of the ipsilateral, i.e. left, eye and from one, the nasal, hemiretina of the contralateral, i.e. right eye.. To test this hypothesis and to determine the specific mapping of the three inputs, pRF mapping (Dumoulin and Wandell 2008) was performed at 3 T for each eye and each hemifield separately (see section 7.2.5). In the control participant, visuotopic maps of each hemifield were found on the contralateral hemisphere (Figure 7.4). Remarkably, stimulation of the left eye in CHP revealed orderly organized eccentricity and polar angle maps of both ipsi- and contralateral hemifields on the left hemisphere across the three early visual areas (V1-V3; Figure 7.5 a & b). Left and right hemifield representations were superimposed in a mirror-symmetrical manner, in accordance with previous reports of achiasma (Hoffmann et al., 2012; Kaule et al., 2014). There was a small normal representation along the
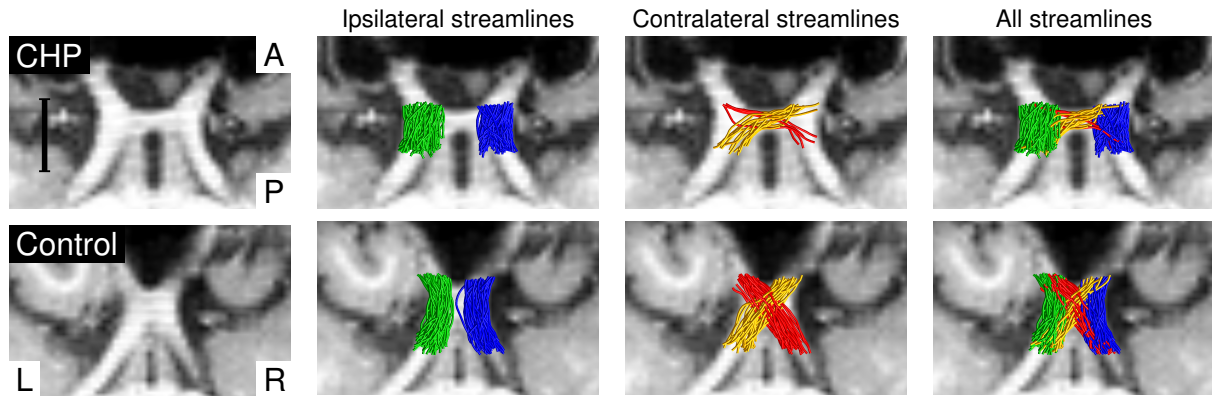
Figure 7.3: **Tractography of the optic chiasm**. Axial slices without and with tractography overlay. The scale bar represents 1 cm. L-R and A-P indicate left-right and anterior-posterior directions, respectively. **top row)** In CHP the ipsilaterally projecting streamlines (blue and green for right and left optic nerve, respectively) are largely symmetrically distributed, while there is a predominance of contralaterally projecting streamlines for the right compared to the left optic nerve (yellow and red, respectively). **bottom row)** In the control both ipsi- and contralaterally projecting streamlines of the right and left optic nerves are largely symmetrically distributed. For clarity, only 0.25% of the generated streamlines are rendered.

horizontal meridian on the contralateral, i.e. right, hemisphere. For hemifield mapping of the right eye in CHP, a similar picture was obtained, i.e. mirror-symmetrical super-positions of orderly visuotopic maps of opposing hemifields (Figure 7.5 c & d). However, in accordance with the above fMRI and DWI results, the residual normal representation was much more widespread than for the left eye. Importantly, this residual normal representation appears to be superimposed onto the other two maps from the left eye as described earlier. As shown in Figure 7.5 d, the residual normal representation of the right hemifield spanned the entire polar angle range, from the lower vertical meridian in the dorsal portion of V1, through the horizontal and to the upper vertical meridian in the ventral portion of V1 and thus followed the normal retinotopic pattern. The observed retinotopic pattern of this residual input was not restricted to V1 and partially spread to V2 and V3. In conclusion, we found a superposition of three retinotopic representations in the left V1 of CHP, i.e., two maps from both visual hemifields mediated by the left eye plus an additional map of the contralateral hemifield from the right eye. A summary of this finding is provided in Figure 7.6 demonstrating the co-localization of three retinotopic representations in the left visual cortex of CHP. This prompted the question of the functional characteristics and the fine-structure of these maps in V1 and beyond.

7.3.4 Responsivity of the visual cortex receiving triple hemifield input

To compare the activation of the early visual cortex across the three hemifield-mapping conditions and to assess how the activation is propagated from V1 to V2 and V3 we determined the area of activated cortex in the early areas of the left hemisphere. As a reference,
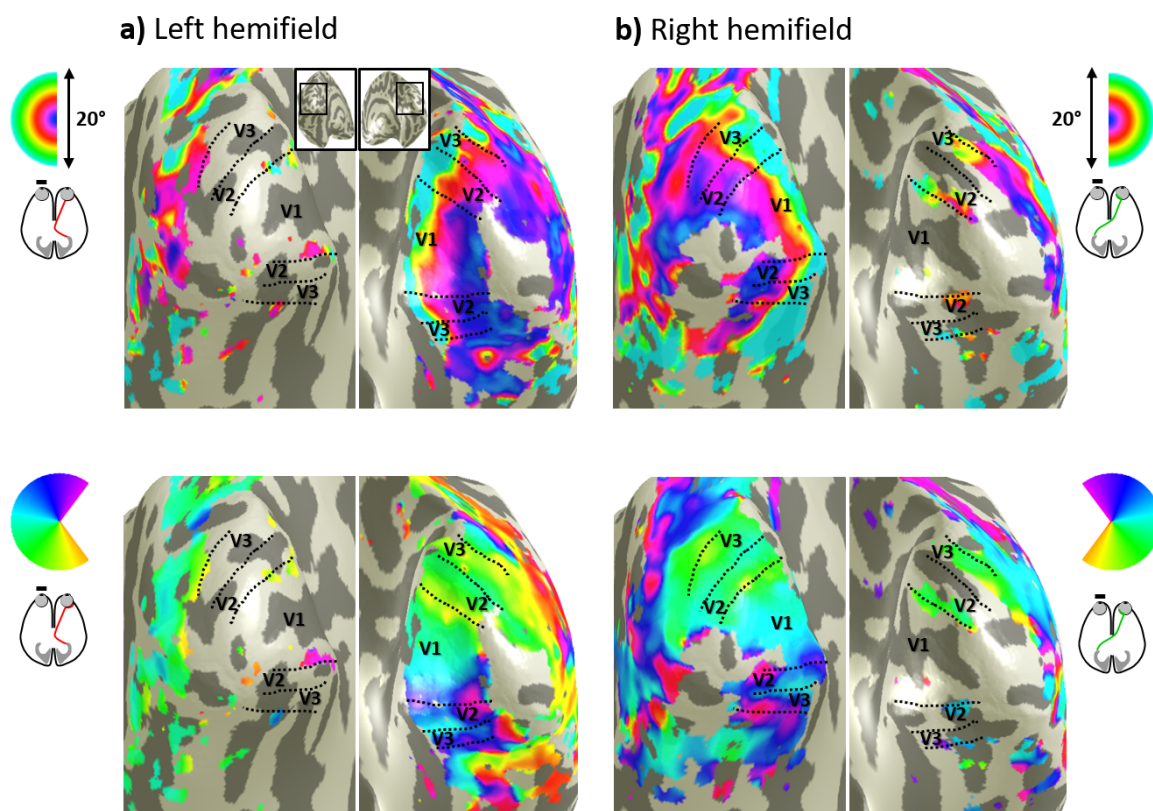
Figure 7.4: **Visual field representations for unilateral stimulation of the right eye in a control participant**. Eccentricity (top row) and polar angle maps (bottom row) on the inflated occipital cortex for **a)** left and **b)** right hemifield stimulation. In both cases, orderly eccentricity and polar angle maps were obtained predominantly on the hemisphere contralateral to the stimulated hemifield. Only, residual representations of the vertical meridians and fovea were observed on the ipsilateral hemisphere, as reported previously (Hoffmann et al., 2003; Tootell et al., 1998).

we used the condition of contralateral hemifield mapping via the left, i.e. ipsilateral, eye (normal input) for normalization and thus determined the relative activated area for both ipsilateral hemifield mapping via the left eye (abnormal input) and contralateral hemifield mapping via the right eye (residual normal input). The abnormal input from the left eye appeared to map over very similar areas of V1, V2 and V3 as the normal input from the left eye. For the residual normal input from the right eye, the pattern was different. Overall, this input mapped to smaller areas of V1, V2 and V3 than the normal input from the left eye. The reduction in the activated area was most marked for V2 and least marked for V3 (Figure 7.7 a). To estimate the response strength in the ROIs with the overlay of the three hemifield representations (ROI$_{3maps}$), we determined the goodness of fit of the pRF model, i.e. mean variance explained (VE), for each condition (Figure 7.7 b). Although the area of cortex mapping the residual contralateral input of the right eye was smaller, the VE associated with this input did not appear to be markedly reduced compared to those driven by the normal and abnormal inputs of the left eye. These findings thus indicate propagation of the triple hemifield input to the extrastriate cortex.
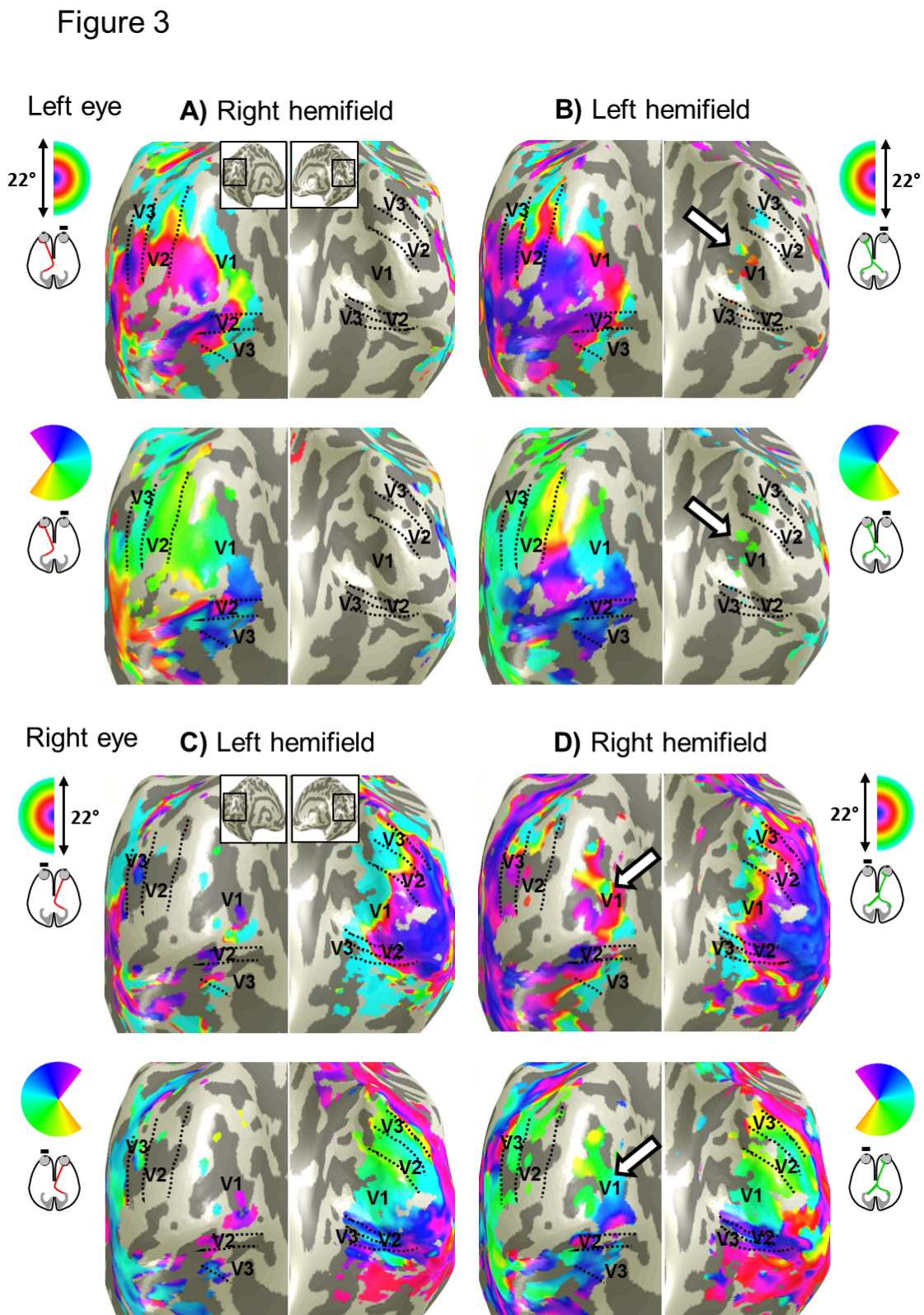
Figure 3

Figure 7.5: **Visual field representations for hemifield pRF mapping in CHP for right and left eye stimulation**. Eccentricity (top row in each panel) and polar angle (bottom row in each panel) maps are depicted on the inflated occipital cortex of CHP. For left eye stimulation, orderly eccentricity and polar angle maps are obtained on left hemisphere for both right and left hemifield stimulation (a & b) and vice versa for right eye stimulation (c & d). In addition, there is normal input to the hemisphere contralateral to the stimulated eye (white arrows). It is small for left eye stimulation and sizable for right eye stimulation, where it spans the entire polar angle range.
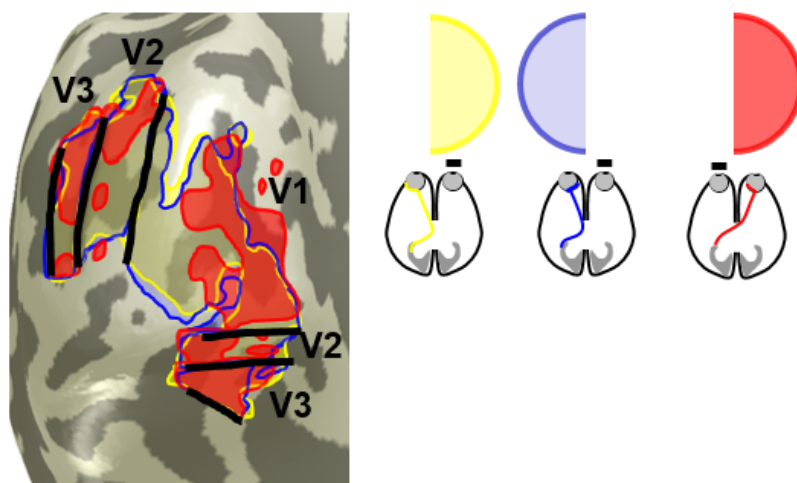
Figure 7.6: **Overlapping representation of the input from three hemifields in the left hemisphere of CHP based on the data shown in Figure 7.5**. The portions of the visual cortex activated by stimulation of the left and right hemifield via the left eye (as typical for complete achiasma), colored yellow and blue, and of the right hemifield (as specific to the present case of CHP), colored red, are arranged as transparent overlays and combined into a single inflated representation of the occipital lobe.
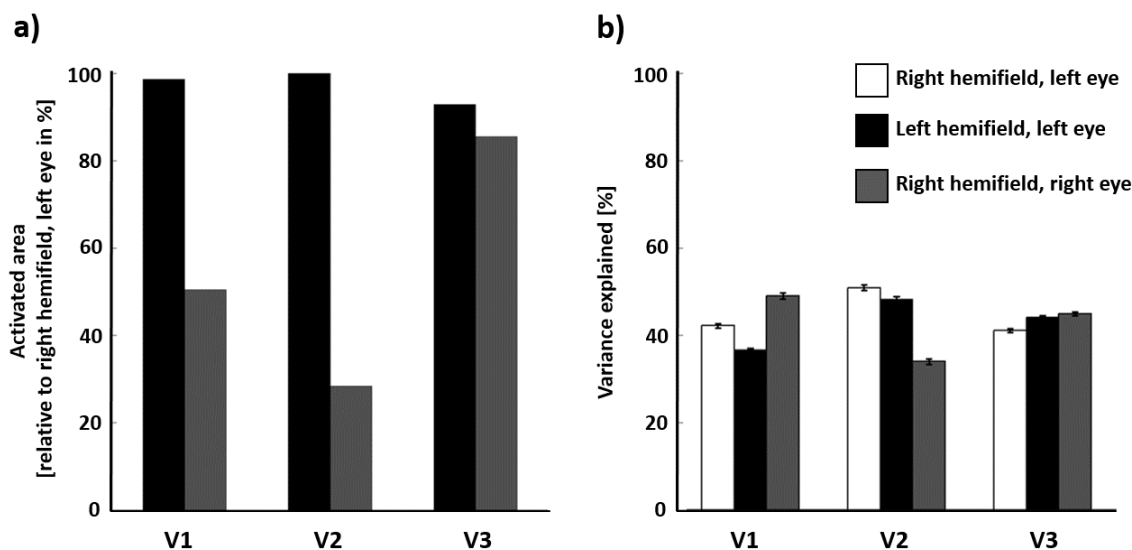

Figure 7.7: **Responsivity of the visual cortex and goodness of the pRF model fit**. **a)** Activated area (normalized with respect to right hemifield, right eye stimulation condition) of left V1-V3 for left hemifield stimulation of the left eye (black bars) and right hemifield stimulation of the right eye (gray bars). For left hemifield stimulation of the left eye, the activated area of the left V1-V3 does not decrease below 92%. For the right hemifield stimulation of the right eye, the relative activated area of V1, V2 and, V3 is smaller, covering 50%, 28%, and 85%, respectively. **b)** Comparison of the explanatory power, i.e. mean variance explained (VE) ± SEM, of the pRF model between right and left hemifield stimulation of the left eye (white and black bars) and right hemifield stimulation of the right eye (gray bars) in V1-V3 restricted to the overlapping areas of the three maps (ROI$_{3\text{maps}}$). The VE for all three maps is relatively similar in V1 and V3 ranging from (49 - 37%) and (41 - 45%), respectively. Variation of VE is observed between the three maps in V2, where the VE is slightly reduced to 34% for right hemifield map of the right eye.

7.3.5   pRF and CF size estimates of the visual cortex receiving triple hemifield input

We scrutinized the pRF size properties of the left V1-V3 restricted to ROI_{3maps}. Similar to controls, the pRF size of each area increased with eccentricity for all three representations. Moreover, there was an increase in the pRF size across visual hierarchy for both left and right hemifield maps of the left eye. This enlargement was most pronounced from V1 to V2 and V1 to V3, whereas the difference of pRF sizes in V2 and V3 was minimal (Figure 7.8 a, middle panels). For the right hemifield map of the right eye, a similar trend was observed for the pRF sizes in V1 and V3. However, unlike the controls and both maps of the left eye in CHP, the pRF size of V2 was smallest (Figure 7.8 a, right panel). This counterintuitive finding might be associated with lower VE and lower relative activated area in V2 for right hemifield mapping of the right eye (see Figure 7.7 a & b). Despite a high degree of similarity of the pRF size vs eccentricity relationship between CHP and the controls, the pRF sizes of V1-V3 for all three maps for PAC were generally larger than for the controls, which might be associated with fixation instabilities in CHP.

Additionally, we estimated the V1-referred CF sizes V2 and V3 in CHP for ROI_{3maps} and compared them to those obtained in controls. We plotted the CF size as a function of eccentricity after adjusting for pRF laterality, indicating the extent to which a pRF overlaps with the ipsilateral visual field (Haak et al., 2013). This yielded V1 sampling extent which is roughly constant across eccentricity but increases through the visual hierarchy in controls. For all three maps of CHP, however, V1 sampling extent in V3 was smaller than that in V2 (Figure 7.8 b, middle and right panels). This alteration might suggest a reduction in the spatial coupling between regions of V1 and V3 which receive triple hemifield input.

7.3.6   Distinct neuronal populations with preference to left or right eye revealed by laminar analysis

To assess the fine-grain structure of the left V1 in CHP, which receives triple input from both visual hemifields, we revisited the ultra-high resolution 7 T data. The differential responses to left and right eye stimulation were visualized on an anatomical image and across the cortical surface at multiple sampling depths. Alternating patches were observed in an anterior ROI, (ROI_{signal}), drawn in the banks of the calcarine sulcus, demonstrating a differential preference for the left or the right eye (Figure 7.9 a). To test the reproducibility, the data were split into two halves i.e. odd and even scans and the analysis was repeated for each half. Similar clustered patterns were observed for both halves, demonstrating scan-to-scan consistency (Figure 7.10). Furthermore, to quantitatively assess the presence of ocular dominance domains, the selectivity index ($I_{selectivity}$) was compared between ROI_{signal} and each ROI_{noise} using ROC analysis across superficial, middle and deep layers (see section 7.2.3). An additional comparison was also performed between the selectivity in ROI_{signal} and the averaged selectivity of all the ten ROI_{noise}. As illustrated in Figure 7.9 b, the average selectivity index for all three layers was above the chance level (area under curve (AUC) for deep layer = 0.5527, AUC for middle layer = 0.5689, and AUC for superficial layer = 0.5835), suggesting segregation of two neuronal
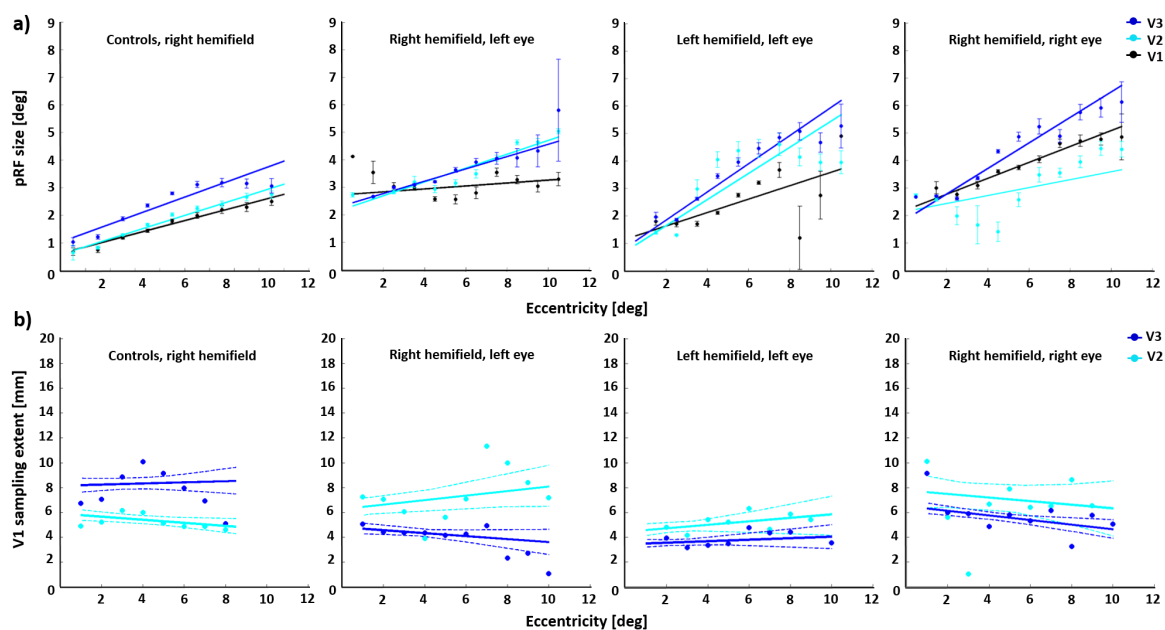
Figure 7.8: **Dependence of pRF size and CF size on eccentricity**. **a)** Comparison of the pRF sizes in V1-V3 between the three maps of CHP and the average pRF size estimates from 4 controls, obtained under right hemifield mapping. For both maps from the left eye (middle panels), the pRF sizes increase as a function of eccentricity and through the visual hierarchy. A similar pattern is observed for the right hemifield map of the right eye (right panel), except for V2 where the pRF size is not increased across visual hierarchy (i.e., pRF size in V2 < pRF size in V1). **b)** Comparison of V1-referred CF sizes in V2 and V3 between three maps of CHP and the average V1-referred CF size estimates from 4 controls, obtained under right hemifield mapping. The CF size is plotted as V1 sampling extent. In contrast to controls, the V1 sampling extent for all three maps of CHP does not increase across visual hierarchy (i.e., V1 sampling extent in V3 < V1 sampling extent in V2). Eccentricity is binned in intervals of 1°. Each dot indicates the mean of the pRF / V1 sampling extent for every eccentricity bin. Solid lines demonstrate the linear fits for the dots and the dashed lines correspond to the 95% bootstrapped confidence interval of the linear fits.

populations with preference to the left or the right eye, predominantly in the vicinity of the calcarine sulcus. Due to the unavailability of CHP for further scanning, no data are available contrasting left and right hemifield representations to test for hemifield domains as described before in complete achiasma (Olman et al., 2016).

7.4   Discussion

In the case of chiasma hypoplasia examined here, three hemifield maps converge onto the same cortical area. This puts a critical challenge on the organization of the visual cortex, which normally comprises a retinotopically aligned overlay of only two maps, i.e. binocular input representing the contralateral visual field. The current study, therefore, provides novel insight into the scope and mechanisms of human visual system development and
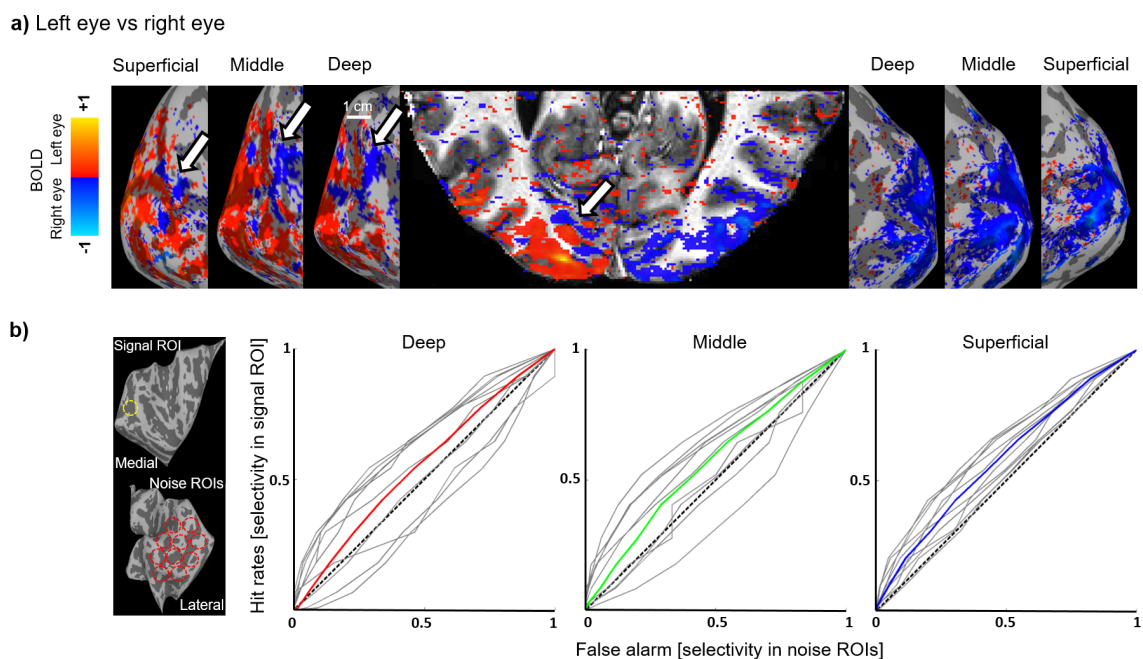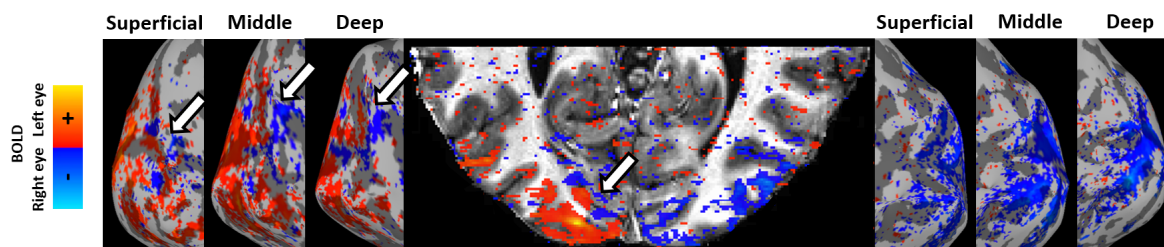
a) Left eye vs right eye

b)

Figure 7.9: **Response to left vs right eye stimulation**. **a)** The cortical activation (signal amplitude expressed as β coefficient from the generalized linear model thresholded by cluster size and mean Student's T statistic (cluster = 20, threshold by T = 1.98, p = 0.05, uncorrected) is projected onto a clipped anatomical image of the occipital cortex and onto the inflated cortical surfaces of the deep, middle, and superficial layers. Right eye preference observed in the anterior region of the left calcarine sulcus is indicated by white arrows. **b)** Comparison of $I_{\text{selectivity}}$ between signal and noise ROIs across lamina via ROC analysis. Hit rates depict the selectivity in the signal ROI, and false alarms outline the selectivity in the ten noise ROIs. The dashed line represents bisection, where the selectivity indices of the signal and noise ROIs cannot be distinguished. The average selectivity indices for all three cortical layers are above the reference line.

a) Even runs; left eye vs right eye
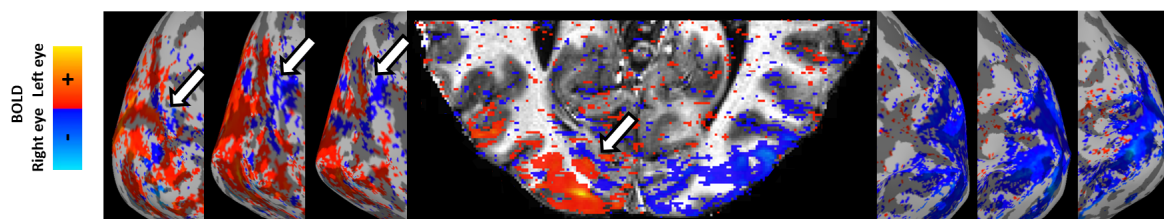

b) Odd runs; left eye vs right eye

Figure 7.10: **Visualization of the differential response to stimulation of the left and the right eye on the split data (even and odd runs)**. Similar patterns were observed for both halves of the data. Conventions as for Figure 7.9.

plasticity. Using ultra-high resolution fMRI at 7 T, DWI and fMRI-based pRF mapping at 3 T, we report uneven numbers of crossing nasal fibers of the two eyes that result in three overlaid representations of opposing hemifields on the left visual cortex with segregation of two neuronal populations in the vicinity of the calcarine sulcus with different ocular preference. These findings demonstrate that the scope of cortical plasticity in the human visual system is sufficient to accommodate three hemifield representations.

The overlaid representation of visual hemifields is a key property of the primary visual cortex. Remarkably, this is not only observed in the neuro-typical visual system, where these two maps comprise the binocular input of the contralateral visual hemifield, it also holds for conditions with abnormal predominantly monocular input, as achiasma, albinism or FHONDA (Ahmadi et al., 2019; Hoffmann et al., 2012, 2003). While the two maps segregate into ocular dominance domains in the former, i.e., the neuro-typical case, they segregate into hemifield domains (Guillery et al., 1984; Olman et al., 2016) for the latter conditions with chiasmal malformations. This is taken as evidence for largely unaltered geniculo-striate connections despite congenitally abnormal input to the LGN (Hoffmann and Dumoulin 2015). The present case of chiasma hypoplasia deviates from the above conditions, as the left primary visual cortex receives triple hemifield input. In the presence of unaltered geniculo-striate projections, such triple hemifield input is expected to result in a combination of the normal organization, i.e. ocular dominance domains (Figure 7.11 a), and the organization found in complete achiasma, i.e. hemifield domains (Figure 7.11 b). Consequently, in the present case of chiasma hypoplasia the abnormal ipsilateral input from the left nasal hemiretina and the residual normal input from the right nasal hemiretina are expected to converge into the same domain (Figure 7.11 c). In the absence of geniculo-striate rewiring, the resulting cortical organization pattern is a retinotopic representation of the contralateral visual hemifield, via the left eye, that is interleaved with combined retinotopic representations of the ipsilateral and contralateral hemifield, via the left and right eye respectively. Consequently, this is termed, in analogy to the nomenclature introduced in (Hoffmann and Dumoulin 2015), 'Interleaved Combined Representation'. Such a pattern would predict the cortical mapping we observed in the left occipital lobe. Moreover, it would predict at the mesoscopic scale regions that are more strongly activated by one eye than the other, and vice versa. This is in accordance with our ultra-high-resolution fMRI findings of ocular dominance domains on the left hemisphere. It should be noted though that the domain receiving input from the right visual hemifield, receives input from both eyes, thus reducing the differential activation via the two eyes. Further, we can, at present, not tell whether the neuronal populations representing the right hemifield input from both eyes segregate into distinct neuronal populations, due to the unavailability of data with sufficient resolution.

Remarkably, the triple hemifield input to the left hemisphere affects only, albeit extensively, part of the primary visual cortex. In fact, another part of the visual cortex receives largely exclusive input from both hemi-retinae of the left eye, as typical for complete achiasma. As a consequence, there is a coexistence of the 'Interleaved Representation' (Figure 7.11 b) and 'Interleaved Combined Representation' (Figure 7.11 c), occupying different regions of the left primary visual cortex. This is in accordance to reports of animal models

of albinism with mixed organization patterns in the primary visual cortex (Cooper and Blasdel 1980). Taken together, this suggests that the relevant adaptive developmental mechanisms can act locally.
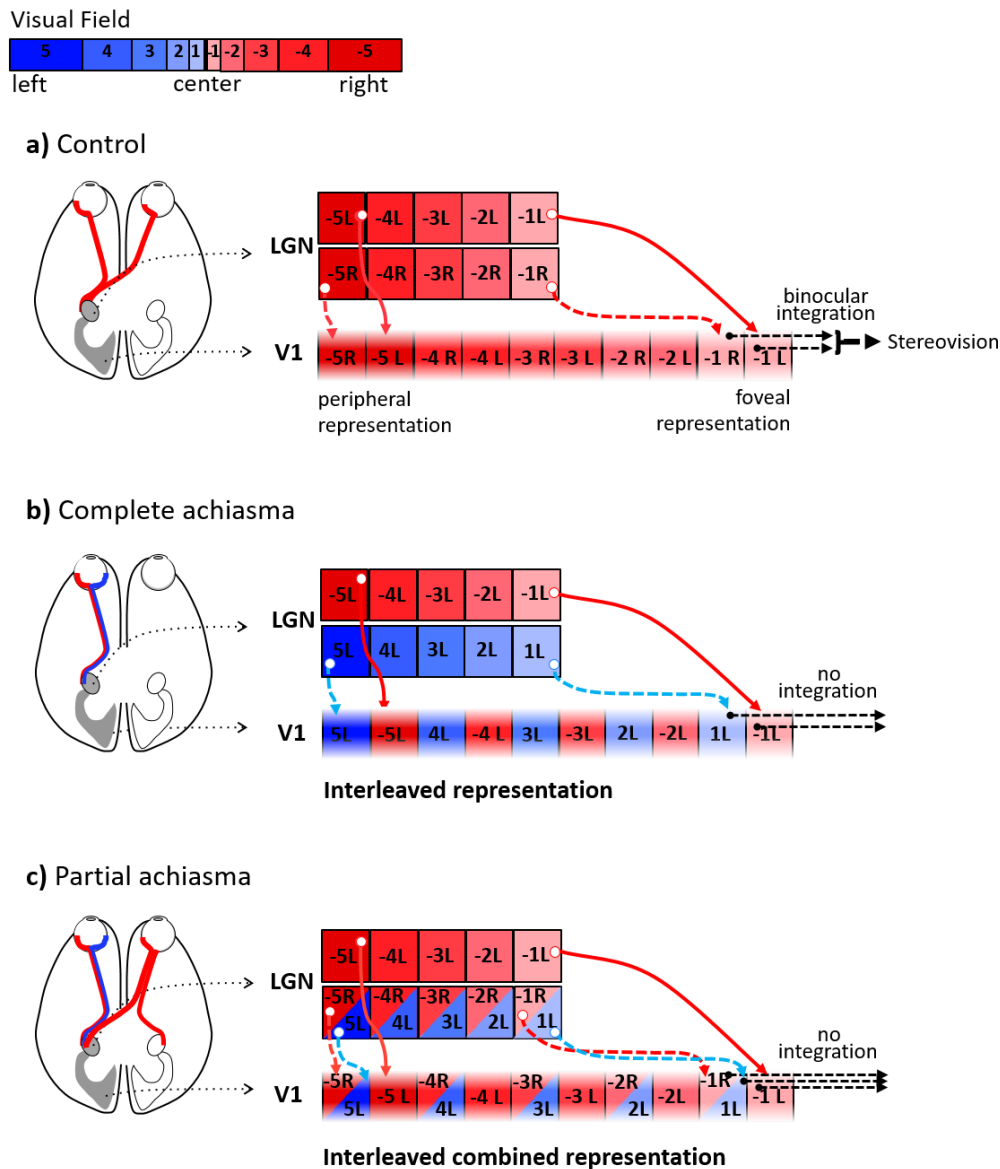
Figure 7.11: **Schematic of visual field representations in primary visual cortex for control, complete achiasma and chiasma hypoplasia**. **a)** Control. The binocular input to the left LGN is organized in retinotopic maps of the right visual field (color coded red; negative numbers) that are separate for each eye (subscript indicates L – left, R – right eye input; the LGN is schematized as only two LGN layers with input from either eye). The geniculo-striate projections (solid red arrows for the left and dashed red arrows for the right eye input) result in interleaved retinotopic representations of the two eyes in V1. Note that the integration of binocular input from corresponding locations in the contralateral visual field leads to stereovision. **b)** Complete achiasma. The left LGN receives monocular input from the nasal

(blue) and from the temporal (red) hemiretina of the ipsilateral eye (i.e. left eye, indicated by the subscript L). Consequently, there is in addition to the normal input from the contralateral visual field (red fields with negative numbers) input from the ipsilateral visual field (blue fields with positive numbers). This leads to the interleaved representation pattern with an interleaved representation of opposing hemifields in V1, which is associated with a conservative, i.e. unchanged, geniculo-striate projection despite the abnormal LGN input (dashed cyan arrows).The absence of integration of the monocular input from opposing visual hemifields counteracts cross-talk of information between the hemifield. **c)** Chiasma hypoplasia. The left LGN receives binocular input from the contralateral visual field (red fields with negative numbers) as well as ipsilateral input (blue fields with positive numbers) only from the left eye. The triple hemifield input to left LGN is organized as interleaved representation of the contralateral visual field from the left eye (red fields with negative numbers in separate boxes) and combined representation of opposing hemifields from both eyes (red fields with negative numbers and blue fields with positive numbers in shared boxes). A conservative geniculo-striate projection, to V1 would result in an interleaved combined representation pattern, obtained by the combination of cortical organization schemes for the control (a) and complete achiasma (b). Specifically, while the contralateral input of the left eye is incorporated via a separate domain, the contralateral input of the right eye together with the ipsilateral input of the left eye are assumed to be accommodated within a shared domain. Similar to complete achiasma, no integration is expected to occur across the three hemifield representations, supporting independent processing of the three maps.

Consistent with the reports on complete achiasma (Davies-Thompson et al., 2013; Hoffmann et al., 2012; Olman et al., 2016; Victor et al., 2000), the participant of the present study also makes effective use of vision in daily life, including sport activities, and reading. This suggests that general aspects of visual function are also preserved in the current case of chiasma hypoplasia, apart from reduced binocular/stereo-vision, strabismus, and nystagmus. Despite the binocular input to the left visual cortex, the disruption of binocular and stereo-vision is expected in CHP due to vertical and horizontal deviations between the two eyes. This indicates that there is no relevant interaction of the three representations in the left visual cortex. In fact, although the independence of perception in opposite hemifields was not quantitatively tested here, the every-day behavior of CHP does not show any confusion between the left and right hemifields. As a consequence, it is, in analogy to findings in other conditions with chiasmal abnormalities (Klemen et al., 2012; Olman et al., 2016; Victor et al., 2000), concluded the three representations of the hemifields in the left primary visual cortex independently drive visual perception. Accordingly, no integration of information across the ocular dominance and/or across the hemifield dominance domains is expected to occur in CHP. Thus, the plasticity of the intracortical microcircuitry appears instrumental to cope with the abnormal visual input and to support independent processing of the three superimposed hemifields (Figure 7.11). Akin to other visual pathway abnormalities, it is therefore assumed that the aberrant representation in CHP is made available for relatively normal visual perception through the interplay of subcortical stability and cortical plasticity. The cortical plasticity might not be confined to changes in the intra-cortical connectivity and, in addition, affect the cortico-cortical connectivity as suggested by changes in pRF and connective

field (CF) size estimates (see Figure 7.8). It therefore appears that the extra-input from the right eye impacts on the cortico-cortical connectivity of the early visual areas in CHP.

7.4.1   Conclusion

Congenital visual pathway abnormalities are powerful models to further our understanding of the scope of developmental stability and plasticity in the human visual system, which may impact on novel therapeutic approaches. Here, we demonstrate that the gross topography of the geniculo-striate projections in CHP remain chiefly unaltered resulting in triple representations in the visual cortex. This reflects the unaltered geniculo-cortical axonal guidance by chemoaffinity gradients (Cang et al., 2005; McLaughlin and O'Leary 2005) even in the face of erroneous input to LGN. The additional input to the left visual cortex is likely incorporated by sharing the same domain between the abnormal input of the left eye and normal input of the right eye. This underlines that intra-cortical plasticity provides sufficient scope to accommodate abnormal visual input for comparatively normal visual processing.

Chapter 8

Population receptive field and connectivity properties of the early visual cortex in human albinism

The work presented in this chapter is currently submitted for publication:

Ahmadi, K., Herbik, A., Wagner, M., Kanowski, M., Thieme, H., Hoffmann, M.B.. Population receptive field and connectivity properties of the early visual cortex in human albinism.

It has also been published in the following preprint server:

Ahmadi, K., Herbik, A., Wagner, M., Kanowski, M., Thieme, H., Hoffmann, M. B. (2019). Population receptive field and connectivity properties of the early visual cortex in human albinism. bioRxiv, 627265.

8.1 Introduction

Albinism is a genetically heterogeneous disorder characterized by abnormal melanogenesis. The lack or reduction of melanin results in several ocular symptoms and misrouting of the optic nerves which have been detailed in section 2.2.1. Due to this mis-projection, a greater extent of the temporal retinal fibers project to the contralateral hemisphere (Apkarian et al., 1983; Creel 1971; Guillery et al., 1975). This leads to superimposed retinotopic maps of opposing hemifields (Hoffmann et al., 2003; Kaule et al., 2014), which disrupts the integration of input from the two eyes and consequently binocular and stereo-vision (Hoffmann and Dumoulin 2015). An electrophysiological investigation in an albino green monkey has shown that at higher spatial resolution these superimposed maps form hemifield dominance domains that are reminiscent of ocular dominance domains in a normal visual system (Guillery et al., 1984). Despite the large-scale aberrant input to the visual cortex, major aspects of visual function remain intact (Eick et al., 2019; Hoffmann and Dumoulin 2015; Klemen et al., 2012; Wolynski et al., 2010). This indicates the presence of plastic mechanisms that make the erroneous visual input available for perception and highlights the importance of albinism as a powerful model to study the foundation of visual pathway formation. The aim of the present study was to determine the consequences of atypical visual projections on pRF and CF profiles in albinism. Our results provide evidence for unaltered geniculo-striate connections and the absence of large-scale reorganization. We suggest that alterations of intra-cortical and cortico-cortical connectivity of the visual system compensate for the gross mis-wiring of the retinal fibers in albinism.

8.2 Methods

8.2.1 Participants

Six albinotic participants (3 females, mean age = 35, range = 18 - 60 years) were recruited for this study. Prior to the study initiation, they were first seen by an optometrist to evaluate their visual acuity and refractive errors. Afterwards, an ophthalmologist determined the degree of iris transillumination, foveal hypoplasia and hypopigmentation of the retinal epithelium. VEPs revealed hemispheric lateralization that is typical of chiasmal misrouting in albinism. All albinotic participants failed to demonstrate stereovision when tested with Lang I, Titmus, and TNO tests (see section 3.8 for details). Fixation stability was assessed as part of the microperimetric examination described in section 3.6 and was performed by an MP-1 microperimeter (Nidek, Padova, Italy). Detailed characteristics of the albinotic participants are summarized in table 8.1. In addition, four controls (2 females, mean age = 31, range = 25 - 49 years) with normal visual acuity, normal stereo-vision and no history of ophthalmological or neurological disorders took part in this study. All participants gave their informed written consent. The study was approved by the ethics committee of the University of Magdeburg and the procedure adhered to the tenets of the declaration of Helsinki.

8.2.2   VEP recording

Conventional pattern-onset VEP was recorded in a dimly lit room for all albinotic partic-
ipants. Left and right eye were stimulated in separate blocks in a counter-balanced design
(a-b-b-a scheme) while the fellow eye was occluded. The recording was conducted using
gold-cup electrodes positioned in OL, Oz, OR (approximately, 4 cm left and right from
Oz), referenced to Fz. The signal was amplified with a physiological amplifier (50,000;
Grass Instruments, Quincy, MA), filtered in the range of 0.3 to 100 Hz and digitized
at the rate of 1 kHz with 12-bit resolution. The EP2000 Evoked Potentials System
(https://www.michaelbach.de/ep2000/html) running on a G4 Power Macintosh was used
for stimulus delivery and electrophysiological recordings. This program presented the
stimuli while stepping through the check size sequence, acquired and displayed the signals
online, checked for and discarded artefacts (using an amplitude window of generally ±50
µV) and saved the records for offline processing. Participants viewed black and white
checkerboard patterns (mean luminance 110 cd/m^2) at a distance of 114 cm in pattern
onset-offset mode (40 ms on, 440 ms off) and were instructed to maintain fixation at a
central target (3° diameter). The central visual field (19° x 15°) was stimulated with a
checkerboard using three different check sizes that were presented in an interleaved man-
ner (2.0°, 1.0°, and 0.5°). The recordings were performed for 98% stimulus contrast twice
for each eye in an interleaved sequence and then repeated at 20% stimulus contrast, again
twice for each eye (Hoffmann et al., 2011). The analysis was performed using technical
graphing and data analysis software (IGOR 5.0; WaveMetrics, Inc., Lake Oswego, OR).
The difference of VEPs (OL minus OR) for each eye was digitally low-pass filtered and
correlated with each other using a time window from 50 to 250 ms to obtain Pearson's
correlation coefficient (Hoffmann et al., 2005). As such, the normal and abnormal pro-
jections of the optic nerves can be distinguished. A positive correlation indicates that
both eyes project to the same cortical regions. In contrast, a negative correlation demon-
strates that both eyes project to opposing hemispheres verifying the misrouting of the
optic nerves (see section 3.5.1).

8.2.3   MRI acquisition

Functional T2*-weighted echo-planar volumes were acquired using a 3 T Magnetom
Prisma scanner (Siemens Healthineers, Erlangen, Germany) with the 64 channel head
coil. The data were obtained at an isotropic resolution of 2.5 x 2.5 x 2.5 mm^3 with 54
axial slices covering the whole brain (TR / TE = 1500 / 30 ms, flip angle: 70°, FOV = 210
mm, multi-band and inplane acceleration factors = 2). Each functional scan was 168 time
frames (252 s) in duration. A total of 9 functional scans were acquired in a single session
[three repetitions per experimental configuration (see below, Visual stimulation)]. Foam
padding was used to minimize the head motion. Additionally, a T1-weighted anatomical
volume was collected using MPRAGE sequence at the beginning of each session (voxel
size = 0.9 x 0.9 x 0.9 mm^3, TR / TI / TE = 2600 / 1100 / 4.46 ms, and flip angle = 7°).

8.2.4 Visual stimulation

Drifting bar apertures (9.5° in radius), exposing a moving high-contrast checkerboard pattern (Dumoulin and Wandell 2008) were displayed at four directions i.e. upward, downward, left and right. The bar moved across the stimulus window in 20 evenly spaced steps and its width subtended 1/4th of the stimulus radius. Each pass of the bar lasted for 30 s, followed by a mean luminance block (zero contrast) of 30 s. The stimuli were generated in Matlab (Mathworks, Natick, MA, USA) using the Psychtoolbox (Brainard and Vision 1997; Pelli 1997) and projected onto a screen with a resolution of 1140 x 780 pixels at the magnet bore. Participants viewed the screen at a distance of 35 cm via an angled mirror and their dominant eye was stimulated under three experimental configurations similar to that reported in section 6.2.2, i.e. (i) bilateral, (ii) left, and (iii) right hemifield stimulation (Ahmadi et al., 2019). They were required to fixate a centered dot and to report color changes between red and green via button press.

Participant	Sex	Stimulated eye	Visual acuity (decimal)	Fixation stability [%]	Misrouting extent
A1	M	Left	0.1	65%	> 9°
A2	F	Left	0.16	83%	> 9°
A3	M	Left	0.12	50%	> 9°
A4	M	Left	0.16	79%	8.2°
A5	F	Left	0.32	-	5.2°
A6	F	Left	0.4	95%	3.1°

Table 8.1: **Characteristics of the albinotic participants**. As a measure for the fixation stability along the horizontal axis, the percentage of eye positions in a horizontal window of ± 3° from the fovea is given, as determined with the MP1 during a fixation task. The misrouting extent was determined from the fMRI data as detailed in section 8.3.1. Note that the maximal that could be determined was, due to the stimulus size, 9.5°.

8.2.5 Data preprocessing and analysis

The T1-weighted anatomical volume was automatically segmented using FreeSurfer (https://surfer.nmr.mgh.harvard.edu). The cortical surface was reconstructed at the white/gray matter boundary and rendered as a smoothed 3D mesh (Wandell et al., 2000). FSL (https://www.fmrib.ox.ac.uk/fsl) was used for the correction of motion artefacts in the functional data. Motion-corrected data for each experimental configuration were then averaged together for every participant to increase the SNR. Afterwards, the functional data were aligned to the anatomical volume using a combination of Vistasoft tools (https://github.com/vistalab/vistasoft) and Kendrick Kay's alignment toolbox (https://github.com/kendrickkay/alignvolumedata). All the subsequent analyses including the estimation of pRF and CF properties, delineation of the visual areas and visualization on the smoothed mesh surface were performed in Vistasoft. A detailed description of the pRF modeling has been provided in sections 3.3 and 6.2.5. Only those voxels

were retained for further analyses for which the pRF model explained at least 15% of the variance. To assess the presence of bilateral pRFs in V1 to V3, the conventional pRF model was extended according to the approach described in section 6.2.5 and compared with mirror-pRF models across (i) vertical meridian and (ii) horizontal meridian (here termed as mirror-pRF models across VM and HM respectively). While the conventional pRF model consists of one circularly symmetric 2D Gaussian, the mirror-pRF models comprise two 2D Gaussians that are mirrored across the vertical or horizontal meridians. Because all parameters of the two Gaussians are linked to each other, mirror-pRF models have the same degrees of freedom as the conventional pRF model. Consequently, the model performance can be compared directly. Unlike the conventional pRF model, mirror-pRF models predict that each cortical location responds to two distinct regions in the visual field.

It has been shown that the pRF model is prone to biased estimates of the receptive fields when the visual stimulus is masked as compared to when a full-field stimulus is presented. This particularly affects the pRFs that are located at the edge of the stimulus space (Binda et al., 2013; Lee et al., 2013; Papanikolaou et al., 2015). To avoid this problem, the representations of the vertical meridian (coinciding with the edge of the hemifield stimuli) were excluded from each ROI for every participant. In addition, the ROIs were restricted to the regions with the overlap of both hemifields for the albinotic participants.

The CF parameters were estimated from the fMRI time-series, using CF modeling method that has been described in detail in sections 3.4 and 7.2.5. As for the pRF-modeling, only model fits were selected whose explained variance exceeded a threshold of 15%. The V1 sampling extent was obtained in V2 and V3 by adjusting the V1-referred CF size in those areas for pRF laterality i.e. the extent to which a pRF overlaps with the ipsilateral visual field (Haak et al., 2013).

8.2.6   Statistical analysis

One-sample t-tests were performed to compare (i) the difference of the pRF sizes of V1 to V3 between the two stimulated hemifields and (ii) the difference of the V1-sampling extent between V3 and V2 in each of the albinotic and control groups. When applicable, multiple comparisons were corrected using the Bonferroni-Holm procedure (Holm 1979) and the adjusted alpha level for each comparison was denoted as (p_α). Additionally, a linear regression model was used to assess the dependence of the V1-sampling extent on eccentricity.

8.3   Results

The functional properties of the early visual areas of the albinotic participants were investigated in two steps. First, the pRF-properties of the visual field maps were detailed based on bilateral and hemifield pRF mapping. Afterwards, the V1-sampling extent was determined in V2 and V3.

8.3.1 Visual field maps and pRF properties in albinism

The visual field maps are presented in Figure 8.1. Here the eccentricity and polar angle maps obtained for hemifield pRF mapping are juxtaposed for a control and two individuals with albinism (all stimulated via the left eye). The left hemifield was represented as an orderly eccentricity and polar angle map on the contralateral, i.e. right hemisphere, in both controls and albinism, confirming the normal projection of the nasal retina for all conditions. In contrast, misrouting of the temporal retinal fibers was evident for the representation of the right hemifield in both albinotic participants. Orderly eccentricity and polar angle maps were found on the right hemisphere, i.e., ipsilateral to the stimulated hemifield. In one of the depicted individuals with albinism (Figure 8.1 b), this abnormality was extensive, indicating a larger shift of the line of decussation into the temporal retina than for the other individual (Figure 8.1 c). This confirmed the well-known variability of misrouting in albinism (Hoffmann et al., 2005, 2003; Von Dem Hagen et al., 2007). In Table 8.1, the extent of misrouting is provided, as determined from the mean eccentricity value of an ROI covering the anterior activated margin of the abnormal representation of the horizontal meridian in the right V1. All in all, these findings demonstrate the mirror-symmetrical retinotopic cortical overlay of normal and abnormal representations of the contralateral and ipsilateral visual hemifield respectively in albinism (Hoffmann et al., 2003; Kaule et al., 2014). This was independently confirmed by the bilateral pRF mapping data: In analogy to previous studies on FHONDA, hemihydranencephaly, and achiasma (Ahmadi et al., 2019; Fracasso et al., 2016; Hoffmann et al., 2012), the goodness of fit, i.e. variance explained (VE), was compared between (i) the conventional single-pRF model and the mirror-pRF models, (ii) across VM, expected to reflect the mirror-symmetrical overlay of opposing hemifields in albinism, and (iii) across HM, as a reference model. As illustrated in Figure 8.2 a, the mirror-pRF model across VM performed worst in the controls, while it performed better in the two albinotic participants with below average misrouting [8° as determined in (Hoffmann et al., 2005)], i.e., misrouting (MR) < 8°, and best in those with above average misrouting, i.e., MR > 8°. Remarkably, this does not only apply to V1, but also to V2 and V3, and thus confirms overlaid representations in these three early visual areas in albinism.

Furthermore, to check the presence of bilateral pRFs in the areas receiving residual normal ipsilateral input, the same analysis was performed on the left V1 to V3 of the albinotic participants with below average misrouting and controls. Note that this analysis cannot be applied to the albinotic group with above average misrouting, since there are only few responsive voxels in the early visual areas of the left hemisphere. As depicted in Figure 8.2 b, the conventional pRF model explained most of the variance in both groups for all three visual areas, demonstrating the predominance of unilateral pRFs in areas which receive normal ipsilateral input. Afterwards, the results of the hemifield stimulation conditions were examined to test the functional equivalence of the two superimposed hemifield representations in albinism. Specifically, the pRF sizes for both hemifield representations were compared. The average pRF sizes of the albinotic participants increased as a function of eccentricity and through visual hierarchy for both hemifield representations (Figure 8.3 a). Note that despite the overall similarity of the pRF size vs eccentricity relationship between the albinotic and control participants, the average pRF sizes in albinotic

Left hemifield

a) Control   **b)** Albinism-A1   **c)** Albinism-A6
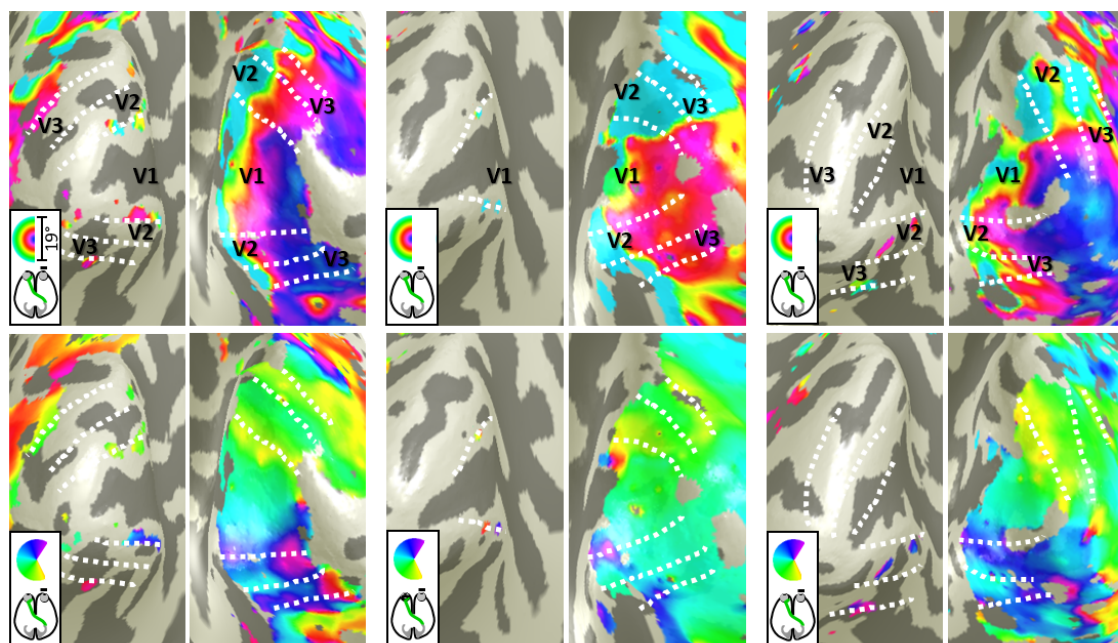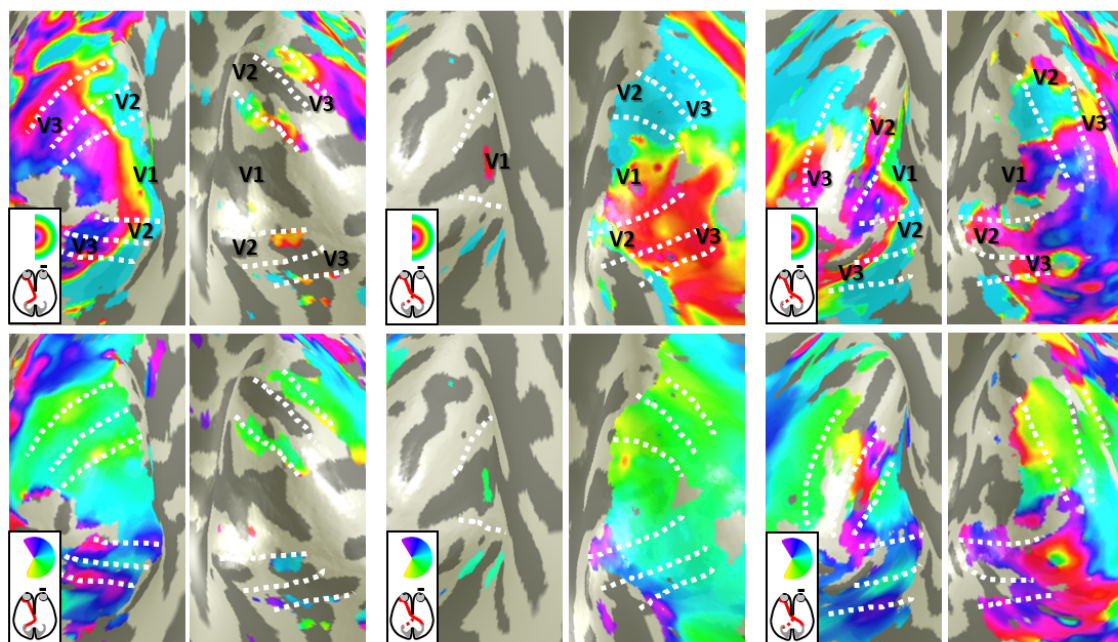

Right hemifield

Figure 8.1: **Hemifield pRF mapping**. Eccentricity and polar angle maps (top and bottom rows in the two panels, respectively) are shown on the inflated occipital cortex under left (nasal retina; top panel) and right (temporal retina; bottom panel) hemifield stimulation conditions. In control **(a)**, stimulation of each visual hemifield elicits orderly eccentricity and polar angle maps predominantly on the hemisphere contralateral to the stimulated hemifield. Only, residual representations of the vertical meridian and fovea are observed on the ipsilateral hemisphere, as reported previously (Hoffmann et al., 2003; Tootell et al., 1998). However, in albinism **(b & c)** there is in addition to the representation of the contralateral (left) visual hemifield, a representation of the ipsilateral (right) hemifield on the right hemisphere, i.e. contralateral to the stimulated eye. While this is extensive for A1, it is smaller for A6 (see Table 8.1), where, as a consequence, a residual normal right hemifield representation is evident on the left hemisphere.

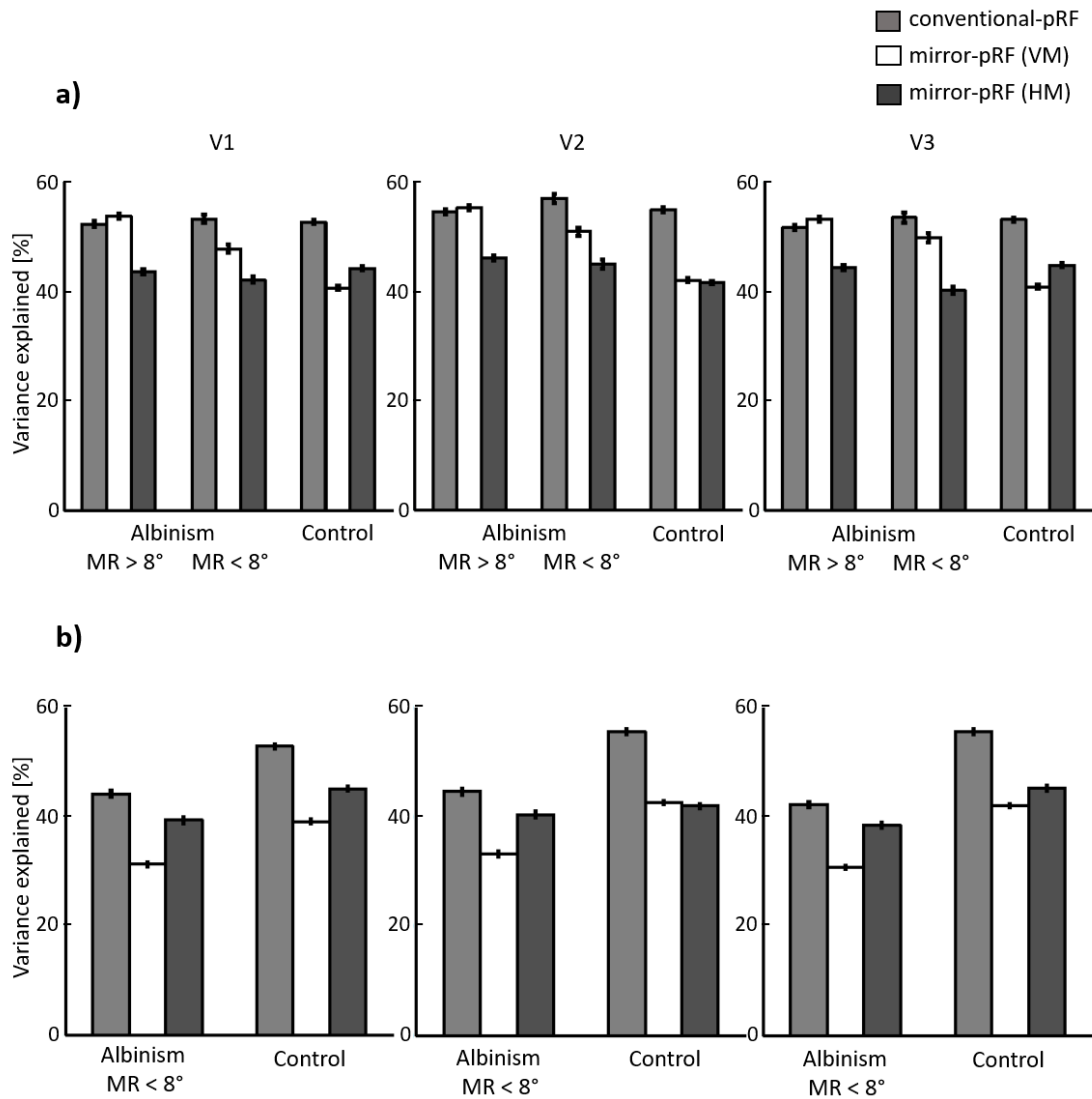individuals exceeded those of controls, likely due to fixation instabilities.

Figure 8.2: **Comparison of the explanatory power of different pRF-models across participant groups and visual areas**. The mean VE $\pm$ SEM is depicted for the conventional pRF model (light gray bars), mirror-pRF models across VM (white bars) and HM (dark gray bars) in V1 to V3. **a)** right hemisphere. The mirror-pRF model across VM performs worst in the controls, better in albinism with MR $< 8°$ and best in albinism with MR $> 8°$ in all three visual areas. **b)** Left hemisphere. The analysis is replicated for the ROIs which receive normal ipsilateral input. The conventional pRF model prevails in both controls and the albinotic group with MR $< 8°$.

Subsequently, to assess the equivalence of the pRF sizes for the two hemifield representations, the average pRF sizes of each area for the left hemifield was subtracted from the corresponding average pRF sizes of the right hemifield representation (Figure 8.3 b). Although a small trend ($< 0.5°$) was observed for larger pRF sizes in V1 and V2 in albinism for the abnormal, i.e. right hemifield, there was no significant difference of the pRF sizes

of V1, V2, and V3 between the two hemifield representations on the same hemisphere in albinism, (t (5) = -1.46, $p_{0.025}$ = 0.20; t (5) = -2.84, $p_{0.017}$ = 0.04; t (5) = 0.17, $p_{0.05}$ = 0.87, respectively). Similarly, in controls no significant pRF-size differences were evident in V1 to V3 for the two hemifields represented on separate hemispheres (t (3) = 1.77, $p_{0.025}$ = 0.17; t (3) = -2.02, $p_{0.017}$ = 0.14; t (3) = 1.66, $p_{0.05}$ = 0.20, respectively). Taken together, in albinism, V1, V2, and V3 comprise functionally equivalent superimposed maps of both the contra- and ipsilateral visual hemifield.
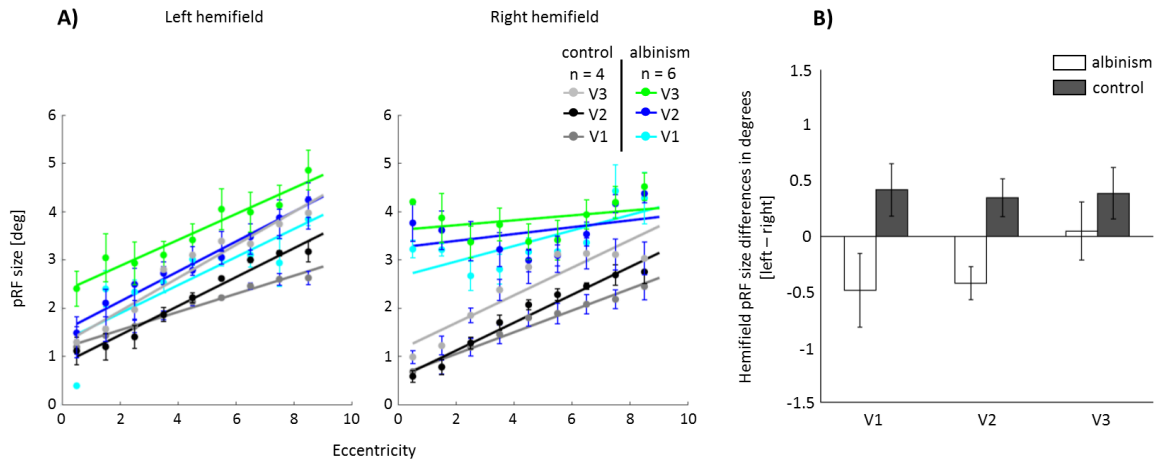

Figure 8.3: **Eccentricity dependence and differences of pRF size between the left and right hemifield representations across participant groups and visual areas**. (a) Similar to controls, the average pRF sizes of all albinotic participants increase as a function of eccentricity and through visual hierarchy for both hemifield stimulations. (b) No significant pRF-size differences were evident neither in the albinotic group nor in the controls. The difference of the pRF sizes between the two hemifields was first calculated in every eccentricity for each participant and subsequently grouped across participants. The bars represent the mean pRF size difference in each group and error bars indicate SEM.

8.3.2   CF-properties in albinism

Generally, the superimposed maps from opposing hemifields in V1 in albinism are taken as evidence for largely stable geniculo-striate connections and a reassignment of ocular dominance domains to hemifield domains. Likewise, the propagation of this mapping-scheme to V2 and V3 suggests largely conservative cortico-cortical connections (Hoffmann and Dumoulin 2015). However, due to the binocular nature of cells in extrastriate areas of the neuro-typical visual system, beyond V1 no simple reassignment of ocular dominance domains is available as a mechanism to accommodate the extra-map of the ipsilateral visual field in albinism. This could reflect on the V1-sampling extent in these areas. As such, the V1-sampling extent of V2 and V3 averaged across the participant groups and the two hemifield representations were compared for the same ROIs also used for the pRF assessments. For the controls, the average V1-sampling extent in V2 and V3 was, in accordance with previous reports (Haak et al., 2013), roughly constant across eccentricity (R^2 = 0.10, p = 0.43, and R^2 = 0.28, p = 0.17, respectively), and increasing through

the visual hierarchy. Similar independence from eccentricity was evident for albinism V2 (R^2 = 0.13, p = 0.37), while a potential dependence on eccentricity was observed for V3 (R^2 = 0.93, p < 0.00001; see Figure 8.4 a). This deviation of V3 from the neuro-typical condition was further supported by the comparison of the difference of V1-sampling-extent observed for V2 and V3 (Figure 8.4 b). While it increased from V2 to V3 in controls (t (3) = 3.24, p = 0.04) as reported previously (Gravel et al., 2014; Haak et al., 2013), no increase was evident for albinism (t (5) =1.1, p =0.32). Taken together, these findings indicate a largely unaltered V1-V2 connectivity in albinism, but suggest an alteration of the functional connectivity for V3.
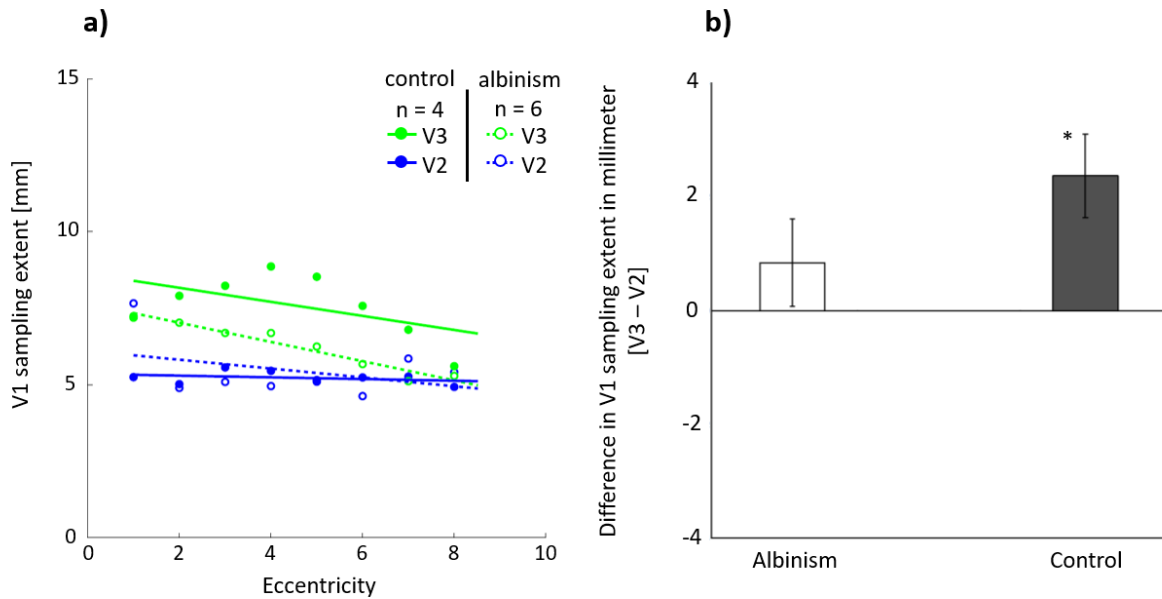

Figure 8.4: **Comparison of V1-sampling extent in V2 and V3 across participant groups**. **(a)** Eccentricity dependence of V1-sampling extent grouped across participants and stimulated hemifields. Akin to the controls, the average V1-sampling extent in V2 remains relatively constant across eccentricity in albinism. However, there is a trend for a decreasing eccentricity dependence of the average V1-sampling extent in V3. Eccentricity is binned in intervals of 1°. Each dot indicates the mean size of V1-sampling extent for every eccentricity bin, and solid lines demonstrate the linear fits for the dots. **(b)** The difference of V1-sampling extent between V3 and V2. The difference of V1-sampling extent in V3 and V2 was averaged across eccentricity and subsequently across hemifields in albinotic participants (white bar) and across hemispheres in controls (gray bar). The bars and error bars indicate the mean difference in V1 sampling extent ± SEM. While in controls the mean difference is significant and exceeds 2 mm, in albinotic participants this difference (0.84 mm) does not reach significance, indicating alterations in the functional connectivity between V1 and V3.

8.4   Discussion

The current study confirms and extends the previous reports on visuotopic organization in human albinism. Using pRF mapping and CF modeling methods, we demonstrate

that in albinism the superimposed maps of opposing visual hemifields in V1, V2, and V3 have similar pRF-sizes and that the cortico-cortical connectivity, as reflected by the V1-sampling extent, appears to be unaltered for V2, but altered for V3. This provides specific insights into the interplay of stability and plasticity supporting visual function in congenital visual pathway abnormalities.

8.4.1   pRF mapping demonstrates equivalent superimposed retinotopic maps of opposing hemifields in albinism

We used pRF mapping to detail the cortical organization in V1 to V3. In accordance with previous findings, we demonstrated that the extent of the projection abnormality in albinism varies between individuals (Hoffmann et al., 2005; Von Dem Hagen et al., 2007) and that the abnormal input is mapped as a retinotopic overlay onto the normal input (Hoffmann et al., 2003; Kaule et al., 2014). As a consequence, mirror-symmetrical visual field positions are represented on similar cortical regions (Hoffmann and Dumoulin 2015). In fact, voxels comprising these two hemifields can be modeled with bilateral receptive fields, as demonstrated in the present study for albinism and earlier for FHONDA, hemi-hydranencephaly and achiasma (Ahmadi et al., 2019; Fracasso et al., 2016; Hoffmann et al., 2012). This prompts the question of whether both representations are processed in the same manner. Unequal pRF-sizes for both representations would serve as an indicator of hemifield-specific processing differences. Remarkably, pRF sizes were equal for both hemifields, which provides physiological support for previous psychophysical reports on equivalent visual perception in both hemifields in albinism (Hoffmann et al., 2007; Klemen et al., 2012). These studies demonstrated similar sensitivities for visual perception mediated via the nasal or the, abnormally projecting, temporal retina, and a lack of cross-talk of information between the two hemifields. Thus, converging evidence is provided that both the contralateral and the additional ipsilateral hemifield representations in the early visual cortex are processed in a similar manner and independently of each other.

8.4.2   Conservative geniculo-striate and cortico-cortical projections

As outlined in chapter 7, the superimposed maps of opposing hemifields reported for V1 in albinism and other congenital chiasmal abnormalities are taken as macroscopic evidence for a cortical organization pattern termed "interleaved representation" which appears to be the only organization pattern available to primates with albinism (Guillery 1986; Guillery et al., 1984). Here the former ocular dominance domains are reassigned to hemifield dominance domains to accommodate the abnormal input from the ipsilateral visual field in albinism. Importantly, this cortical representation can be explained by largely stable, geniculo-striate projections. In turn, independent visual functioning of the two hemifield representations is assumed to be due to adaptations of the intra-cortical micro-circuitry in V1 (Hoffmann and Dumoulin 2015; Sinha and Meng 2012). The propagation of this pattern beyond V1 indicates, as reported here and in previous studies (Hoffmann et al., 2003; Kaule et al., 2014), a largely stable cortico-cortical connectivity. This stability is further supported by the similarity of V1-sampling extent in

V2 for controls and albinism. Remarkably, the V1-sampling extent is altered beyond V2. In fact, while an unaltered gross-connectivity serves the propagation of the retinotopic maps through the hierarchy of the early visual cortex, the altered sampling of V3 from V1 might be a specific adaptation to the abnormal cortical input in albinism. This is suggested by the comparison of the mechanisms available to accommodate the 'extra-map', i.e. from the ipsilateral hemifield, in striate vs extrastriate cortex: At the level of extrastriate cortex, the accommodation of the representation of the ipsilateral visual field is much more demanding, since, at this stage, most neurons normally receive binocular input (Felleman and Van Essen 1987; Kaule et al., 2014; Maunsell and van Essen 1983; Tanabe et al., 2005). While in albinotic V1 the obsolete ocular dominance domains can be simply reassigned to hemifield dominance domains, in extrastriate cortex no such spare resources appear to be available. Consequently, part of the neural resources normally allocated for processing the contralateral visual field must be made available for processing the additional input from the ipsilateral visual field. This is expected to result in an – at the mesoscopic scale – altered representation of the visual information from V2 onwards. As a result, the sampling by V3 is expected to be altered. Accordingly, our results for the V1-sampling extent in V3 might, therefore, reflect these extrastriate adaptations in albinism. Further studies are needed to elucidate this process and to identify the underlying adaptive mechanisms. Taken together, our findings highlight the dominance of conservative developmental mechanisms in human albinism, but at the same time indicate that plasticity shaping the input to V3 contributes to tuning the cortico-cortical connectivity to the altered visual input.

8.4.3 Conclusion

Albinism has a profound effect on the structure and function of the visual system, providing a compelling model to study plastic mechanisms in humans. Our findings demonstrate the absence of extensive reorganization and gross stability of geniculo-striate and cortico-cortical projections. The adjustments of the cortico-cortical connections at the level of V3 might be critical to support the independent processing of two opposing hemifields within the same hemisphere.

Chapter 9

General discussion

Over the past few decades, the use of noninvasive neuroimaging techniques, particularly fMRI in conjunction with the advancements in neuro-computational approaches have drastically broadened our knowledge of the functional architecture of the human visual cortex. Multiple visual field maps have been identified by the application of retinotopic mapping methods. These methods have a profound potential to investigate the effects of visual dysfunctions on cortical visual responses. The present chapter provides a brief overview of the current developments in the field of retinotopy, followed by applications to the pathologies of the visual system as described in chapters 5 – 8, and concludes with suggestions for future research directions.

9.1   Retinotopy: from its infancy to current progress

The first in vivo retinotopic maps of the human visual cortex were determined in the 1990s by a series of publications from independent research groups (DeYoe et al., 1996; Engel et al., 1997, 1994; Sereno et al., 1995). They used stimuli that create a travelling wave of activity in the brain when a fixating observer is presented with two types of stimuli, i.e. expanding/contracting rings to measure the eccentricity maps, and rotating wedges to measure the angle maps (see section 3.2 for further details). Despite its success in identifying several visual field maps, this method, also known as phase-encoded retinotopy, has a number of limitations. First, it does not interpret all the information in the time series, instead, it only estimates the visual field locations that produce the largest fMRI signal in each voxel. Second, the method is not optimal to map the areas with large receptive field sizes (Wandell et al., 2007). These limitations were addressed by the advent of population receptive field (pRF) modeling in 2008 (Dumoulin and Wandell 2008). This model-based approach revolutionized the field of visual neuroscience by measuring the neuronal properties that were previously available only via invasive electrophysiological experiments (Keliris et al., 2019). Using a single circular symmetric Gaussian, the model estimates visual field maps, pRF center positions, size and laterality (see also section 3.3). Several complex models have been built based on the conventional pRF model. The complexity of these new models concerns two main aspects: a variety of pRF shapes and additional computations on the visual image (Wandell and Winawer 2015). For instance, the conventional single-Gaussian pRF model has been extended to mirror-pRF models

with two Gaussians (Ahmadi et al., 2019; Fracasso et al., 2016; Hoffmann et al., 2012). Additionally, instead of a Gaussian, a broader class of allowable shapes can be used to estimate the pRF properties (Keliris et al., 2019; Lee et al., 2013). Other recent models have been constructed that employ a wide range of band-pass filtered images containing large amounts of second-order contrast (spatial variation in the contrast), rather than the binary representation of the image contrast (Kay et al., 2013). These models predict responses that depend on the stimulus pattern, rather than its location per se (Wandell and Winawer 2015). The newer generations of pRF model would further advance our understanding of the pRF characteristics within the visual cortex.

9.2 Investigating disorders of the visual system

Understanding the mechanisms of cortical reorganization often requires invasive experimental manipulations and has therefore long been dominated by animal studies. Nature, however, has provided pathological cases where the normal development of the visual system is altered. Consequently, reorganization can be studied directly in humans without experimental manipulations of the neural substrate. Combined with fMRI-based retinotopic mapping methods this provides a powerful approach to study the scope of reorganization in visual system pathologies. Pioneering examples for these applications (Baseler et al., 2002; Hoffmann et al., 2003; Morland et al., 2001) stimulated the field efficiently as reflected by recent reviews on the nature of the interplay of stability and plasticity in the human visual system (Hoffmann and Dumoulin 2015; Morland 2015; Wandell and Smirnakis 2009). The current notion among the neuroscientists is that plastic mechanisms are available in the human visual system(Plank et al., 2014; Rosengarth et al., 2013), but limited for acquired disorders (Baseler et al., 2011) and greater for congenital disorders (Baseler et al., 2002; Kaule et al., 2014). In the following sections, the cortical changes associated with transient visual anomalies or congenital abnormal development of the visual system are discussed.

9.3 Neural correlates of migraine aura

Patients suffering from migraine with aura often report visual discomfort prior to the headache attacks. The aura is characterized by multifaceted symptoms, ranging from negative symptoms e.g. scintillating scotoma to positive ones (flickering or wavy patterns). Although cortical spreading depression (CSD) is considered as the underlying aetiology of the aura (Leo and Morison 1945), the correlation between the heterogeneous aura symptoms and CSD has been rarely studied. As described in chapter 5, we used different fMRI-paradigms, including retinotopic mapping for the identification of the early visual areas to study the effects of migraine aura on the cortical signals. We found reduced BOLD responses following negative symptoms and increased BOLD responses following positive symptoms. Furthermore, we observed bihemispheric BOLD changes in patients experiencing bilateral symptoms. This study takes the only preceding fMRI investigation of migraine aura (Hadjikhani et al., 2001) a step further and serves as an example of the power of retinotopic mapping assisted fMRI investigation of abnormal perceptual intervals

in transient visual pathway dysfunction. The BOLD changes during positive and negative symptoms reflect different effects of CSD on the neuronal activity and neurovascular coupling in the human brain. Identifying these different pathological changes in future studies may have potential implications for prognosis and treatment of migraine.

9.4 Congenital chiasmal abnormalities

As outlined in section 2.1, the topographic representation of the visual field is a predominant organizational principle of the visual cortex thought to be vital for its functionality. The establishment of such a topographic organization requires a succession of pre-programmed developmental mechanisms as following: i) contralateral projection of the nasal retinal axons at the optic chiasm, and ipsilateral projection of the temporal retinal axons, ii) termination of the binocular projections in alternation in the 6 corresponding topographically organized layers of LGN, iii) two overlaid representations of the contralateral visual hemifield, one from each eye, organized in alternating ocular dominance domains in V1 (Muckli et al., 2009). Investigating the consequences of changes to these retino-cortical connections can uncover the interplay of developmental plasticity to preserve normal visual function. While in humans experimental changes cannot be applied, there are cases in which this normal topographic scheme is disrupted.

Prime examples are congenital chiasmal abnormalities where the typical projection of the optic nerves is severely altered. Consequently, the visual cortex receives monocular input not only from the contra- but also from the ipsilateral visual field. At the macroscopic scale, this leads to superimposed retinotopic maps of opposing hemifields with bilateral pRFs on each hemisphere. Remarkably, at the mesoscopic scale, these maps give rise to hemifield dominance domains (Guillery et al., 1984; Olman et al., 2016) that replace ocular dominance domains in a neurotypical visual system.

Using an integrated approach of functional and structural imaging, we investigated the cortical organization associated with enhanced crossing of the temporal retinal axons in FHONDA and albinism, as well as reduced crossing of the nasal axons in chiasma hypoplasia, described in chapters 6 – 8.

9.4.1 Stability of geniculo-striate projections – a general feature?

The observed overlay of opposing hemifields for enhanced crossing of the optic nerves is a natural consequence of unaltered geniculo-striate connections in the presence of the abnormal input to LGN (Hoffmann and Dumoulin 2015). Remarkably, this is not specific to the pigmentation deficits in albinism and also applies to FHONDA that is associated with the absence of any hypopigmentation, as demonstrated in the present thesis (chapter 6; Ahmadi et al., 2019). Furthermore, evidence for unaltered geniculo-striate connections has also been provided for reduced crossing, i.e. achiasma, as demonstrated in (Hoffmann et al., 2012; Kaule et al., 2014) and the current thesis (section 2.2). This underlines the importance of the stability of geniculo-striate connections in the presence of a variety of abnormalities. It, therefore, suggests that this subcortical stability is a general feature in

human visual system development. Interestingly, the stability of geniculo-striate connections is not limited to conditions with two superimposed maps, rather it also holds true even in the presence of triple inputs to the visual cortex as observed in chiasma hypoplasia (see chapter 7). As a result of such stable projections, the organization of V1 follows the 'interleaved representation' scheme in albinism, FHONDA and complete achiasma. In the case of chiasma hypoplasia with triple hemifield maps, however, the 'interleaved combined representation' scheme is expected. It results from the combination of the cortical organization in a normal visual system and complete achiasma as depicted in Figure 9.1. Taken together, it appears that despite distinct types of misrouting, similar mechanisms shape the organization of the visual cortex in congenital chiasmal abnormalities.

9.4.2   Plastic mechanisms in V1 and beyond

To preserve relatively normal visual function in different types of congenital chiasmal abnormalities, the stability of the geniculo-striate connections needs to be combined with plastic mechanisms. Changes to the intra-cortical circuitry appear to serve this purpose. While information integration across ocular dominance domains yields binocular- and eventually stereo-vision in a normal visual system, integration of the inputs from hemifield dominance domains in congenital chiasmal abnormalities would cause confusion between left and right hemifields. Notably, no evidence for inter-hemifield transfer of adaptation to oriented lines (tilt after-effect) was found in previous studies using behavioral or fMRI paradigms (Bao et al., 2015; Klemen et al., 2012). Thus, subtle alterations of the intra-cortical circuitry within V1 are required to selectively eliminate those integrative processes to avoid cross-talk of information from one hemifield to another (Hoffmann and Dumoulin 2015; Hoffmann et al., 2012). The lack of binocular and stereo-vision in congenital chiasmal abnormalities raises another fundamental question on whether the visual input viewed by one eye would be to available to the other eye. A recent study revealed that interocular transfer of visual memory successfully occurs in participants with albinism providing evidence for the plasticity of inter-hemispherical information flow (Eick et al., 2019). Analogous findings are, although not explicitly tested yet, expected for achiasma, FHONDA and chiasma hypoplasia. Importantly, the cortical plasticity may not be restricted to the intra-cortical connections in V1 and might impact the cortico-cortical connectivity in extrastriate areas as demonstrated by changes of the V1-sampling extent in V3 for chiasma hypoplasia and albinism (see chapters 7 and 8). In conclusion, stable geniculo-striate projections in combination with fine intra- and cortico-cortical plasticity provide sufficient scope to support independent processing of the opposing hemifields and make the abnormal input available for relatively normal visual perception.

9.4.3   Relevance and practical consequences

Congenital chiasmal abnormalities offer a unique opportunity to study the dynamics of developmental plasticity in the human visual system. Therefore, comprehensive investigations of these conditions might influence the optimization of vision restoration strategies in congenital and acquired blindness (Ashtari et al., 2011; Striem-Amit and Amedi 2014).
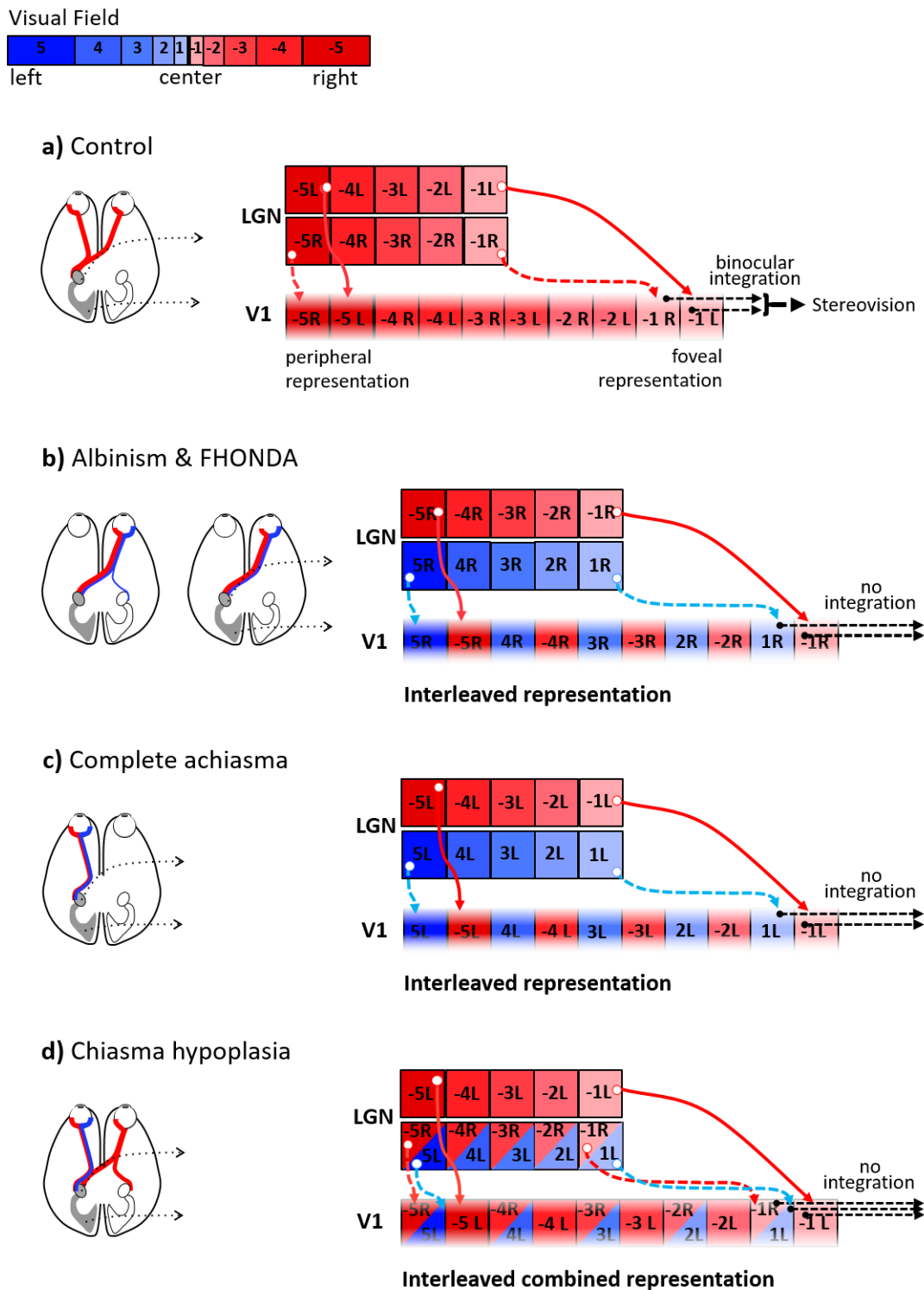
Figure 9.1: **Schematic of the organization of V1 in normal visual system and congenital chiasmal abnormalities extending the previous account by Hoffmann and Dumoulin 2015**. **a)** Control. The binocular input to the LGN is organized in retinotopic maps of the right visual field (color coded red; negative numbers) that are separate for each eye (subscript indicates L – left, R – right eye input; the LGN is schematized as only two LGN layers with input from either eye). The geniculo-striate projections (solid red arrows for the left and dashed red arrows for the right eye input) result in interleaved retinotopic representations of the two eyes in V1. Integration of the binocular input leads to stereovision. **b)** Albinism & FHONDA. The LGN receives monocular input from the nasal (red) and from the temporal (blue) hemiretina of the contralateral eye.

This leads to the interleaved representation of opposing hemifields in V1, which is associated with an unaltered geniculo-striate projection despite the abnormal LGN input (dashed cyan arrows). Cross-talk of information between the hemifield is prevented by the absence of integration of the monocular inputs. **c)** Complete achiasma. The LGN receives monocular input from the nasal (blue) and from the temporal (red) hemiretina of the ipsilateral eye. Akin to albinism and FHONDA, this yields an interleaved representation of opposing hemifields in V1. The absence of integration of the monocular inputs counteracts cross-talk of information between the hemifield. **d)** Chiasma hypoplasia. The LGN receives binocular input from the contralateral visual field (red fields) as well as ipsilateral input (blue fields) only from the left eye. The triple hemifield input to LGN is organized as interleaved representation of the contralateral visual field from the left eye (red fields in separate boxes) and combined representation of opposing hemifields from both eyes (red and blue fields in shared boxes). The stable geniculo-striate projections result in an interleaved combined representation pattern, obtained by the combination of cortical organization schemes for the control (a) and complete achiasma (c). Similar to other congenital chiasmal abnormalities, no integration is expected to occur, supporting the coexistence of the three maps.

Furthermore, the relation of congenital chiasmal abnormalities and the clinical symptoms may lead to therapeutic initiatives in the affected individuals (Hoffmann and Dumoulin 2015). In this regard, a potentially beneficial topic is the origin of the nystagmus. Although congenital foveal dysfunction has been regarded as the primary cause of infantile nystagmus syndrome, it might not be the only cause in congenital chiasmal abnormalities. for example, nystagmus occurs in achiasma in the absence of foveal hypoplasia and in some animal models of albinism without a fovea (Hoffmann and Dumoulin 2015). In these conditions, the nystagmus might be associated with miswiring of the optic nerves (Chen et al., 2014). As a result, studying the subcortical components of the visual system in congenital chiasmal abnormalities may reveal the underlying mechanisms of nystagmus.

9.5   Outlook

The current thesis stimulates further research in migraine aura and congenital chiasmal abnormalities. Multimodal studies using PET MRI are expected to be of use to assess regional cerebral blood flow changes along with BOLD responses during the aura. Moreover, identification of the characteristic profiles of neurotransmitter receptors or ion channels may lead to the development of new pharmacological treatments for migraine with aura.

Future studies in congenital chiasmal abnormalities promise to increase our understanding of human visual system development and plasticity as detailed below. Specific research targets comprise the investigation of the impact of chiasmal abnormalities on (i) interhemispherical cortical connectivity, (ii) laminar cortical activation profiles, (iii) functional and anatomical measures of the extent of misrouting, and (iv) its relevance for the development of advanced pRF models.

(i) The plasticity of interhemispherical cortico-cortical connectivity is a rewarding target. According to a recent report, there is an increased functional inter-hemispherical connectivity of the primary visual cortices in albinism (Welton et al., 2017). This find-

ing prompts two major questions on whether the connectivity increase is specific to the abnormal visual field representation and whether the increase in functional connectivity propagates through the visual hierarchy. These questions can be addressed by the application of advanced fMRI-based functional connectivity analyses to discern the plastic mechanisms operating at different tiers of visual processing.

(ii) The investigations of laminar activation profiles might help to uncover the adaptation of feed-back connections in the visual cortex in chiasmal abnormalities. It has been shown that the abnormal representation of the ipsilateral hemifield in congenital chiasmal abnormalities contributes to visual perception (Bao et al., 2015; Klemen et al., 2012). It is therefore expected that top-down connections are also adapted. As such, the equivalence of these modulations should be studied using ultra-high field fMRI at submillimeter resolution across cortical laminae to differentially assess bottom-up and top-down mechanisms.

(iii) fMRI estimates of the degree of misrouting in albinism reported in chapter 8 (see table 8.1) can be used for cross-validation of the misrouting estimates obtained by DWI data. Inspired by a recent diffusion tensor imaging study reporting a higher streamline decussation index (percentage of total tractography streamlines decussating at the chiasm) in albinism (Ather et al., 2019), we correlated the fMRI estimates of the degree of misrouting with the DWI estimates of the same albinotic participants that were modeled using constrained spherical deconvolution (CSD). There was a significantly positive correlation indicating the precision of DWI in the detection of structural abnormalities of the optic chiasm. The results are presented in a recent conference contribution (Puzniak et al., 2019) and submitted for publication.

(iv) Congenital chiasmal abnormalities provide an efficient test-bed for further improvement of the pRF model. In an ongoing collaborative project with the group of Prof. Cornelissen (the University of Groningen, the Netherlands), a novel framework termed micro-probing was pursued that overcomes the limitations of the mirror-pRF models. The dependence of these models on prior assumptions i.e. mirror symmetrical positioning of the pRFs within a voxel poses a significant challenge to uncover unpredictable pRF properties (Lee et al., 2013). Our new approach, however, samples the entire visual space with micro-probes i.e. tiny fixed-size Gaussian models that make minimal prior assumptions. We have validated the method by applying it to the albinism dataset described in chapter 8 and show that it successfully captures the bilaterally fragmented pRF characteristic in albinotic participants without prior knowledge of the shape and distribution of the pRFs. The results are also presented in a recent conference contribution (Carvalho et al., 2019) and are in preparation for submission.

9.6 Concluding Remarks

During the last 25 years, fMRI-based retinotopic mapping methods have generated a wealth of information about the human visual field maps. These methods are particularly useful to relate visual dysfunction to the underlying cortical response changes. In the present thesis, transient visual abnormalities in migraine with aura and the altered development of the visual system in congenital chiasmal abnormalities were examined.

On the one hand, the findings indicate that different aura symptoms correspond to different cortical changes in migraine. On the other hand, they demonstrate the importance of the interplay of subcortical stability and cortical plasticity in congenital chiasmal abnormalities. The current thesis thus enhances our knowledge of the organization of the human visual system and has major immediate and future implications in the diagnosis and treatment of a wide range of visual abnormalities. Further advances in MR instrumentation such as MR spectroscopy and MR relaxometry combined with improvements in neuro-computational models would yield more insight into the molecular and cellular architecture of the visual cortex guiding the development of novel therapeutic interventions.

List of Figures

References are listed when the figures are not from the author's unpublished dataset.

List of Tables

List of Abbreviations

fMRI   functional Magnetic Resonance Imaging

BOLD   Blood Oxygen Level Dependent

FHONDA   Foveal Hypoplasia, Optic Nerve Decussation defects, Anterior

                       segment dysgenesis

pRF   population Receptive Field

DWI   Diffusion-Weighted Imaging

V1-V4   Visual areas 1-4

CF   Connective Field

CSD   Cortical Spreading Depression

VEP   Visual Evoked Potential

CBF   Cerebral Blood Flow

CSF   Cerebrospinal fluid

EEG   Electroencephalography

MEG   Magnetoencephalography

EPI   Echo Planar Imaging

TR   Repetition Time

TE   Echo Time

TA   Acquisition Time

FOV   Field Of View

MPRAGE   Magnetization-Prepared Rapid Acquisition with Gradient Echo

MP   Microperimetry

FrACT	Freiburg Visual Acuity and Contrast Test
RGCs	Retinal Ganglion Cells
LGN	lateral geniculate nucleus
TO1 / TO2	Temporal-Occipital areas 1-2
LO1	Lateral-Occipital area 1
RSS	Residual Sum of Squares
SNR	Signal-to-Noise Ratio
ROI	Region Of Interest
PET	Positron-Emission Tomography
OCT	Optical Coherence Tomography
VM	Vertical Meridian
HM	Horizontal Meridian
CHP	Chiasma Hypoplasia
PSF	Point Spread Function
GLM	General Linear Model
ROC	Receiver Operating Characteristic
AUC	Area Under Curve
CSD	Constrained Spherical Deconvolution
ET	Ensemble Tractography
ACT	Anatomically-Constrained Tractography

Bibliography

Adrian, E. D. & Matthews, B. H. (1934). The Berger rhythm: potential changes from the occipital lobes in man. *Brain, 57*(4), 355–385.

Ahmadi, K., Fracasso, A., van Dijk, J. A., Kruijt, C., van Genderen, M., Dumoulin, S. O., & Hoffmann, M. B. (2019). Altered organization of the visual cortex in FHONDA syndrome. *NeuroImage, 190*, 224–231.

Amano, K., Wandell, B. A., & Dumoulin, S. O. (2009). Visual field maps, population receptive field sizes, and visual field coverage in the human MT+ complex. *Journal of neurophysiology, 102*(5), 2704–2718.

Ancona, C., Stoppani, M., Odazio, V., La Spina, C., Corradetti, G., & Bandello, F. (2014). Stereo tests as a screening tool for strabismus: which is the best choice? *Clinical ophthalmology (Auckland, NZ), 8*, 2221.

Andersen, A. R., Friberg, L., Olsen, T. S., & Olesen, J. (1988). Delayed hyperemia following hypoperfusion in classic migraine: single photon emission computed tomographic demonstration. *Archives of neurology, 45*(2), 154–159.

Anderson, E. J., Tibber, M. S., Schwarzkopf, D. S., Shergill, S. S., Fernandez-Egea, E., Rees, G., & Dakin, S. C. (2017). Visual population receptive fields in people with schizophrenia have reduced inhibitory surrounds. *Journal of Neuroscience, 37*(6), 1546–1556.

Andersson, J. L., Skare, S., & Ashburner, J. (2003). How to correct susceptibility distortions in spin-echo echo-planar images: application to diffusion tensor imaging. *Neuroimage, 20*(2), 870–888.

Apkarian, P., Bour, L., Barth, P., Wenniger-Prick, L., & Verbeeten Jr, B. (1995). Non-decussating retinal-fugal fibre syndrome: An inborn achiasmatic malformation associated with visuotopic misrouting, visual evoked potential ipsilateral asymmetry and nystagmus. *Brain, 118*(5), 1195–1216.

Apkarian, P., Bour, L., & Barth, P. G. (1994). A Unique Achiasmatic Anomaly Detected in Non-albinos with Misrouted Retinal-fugal Projections. *European Journal of Neuroscience, 6*(3), 501–507.

Apkarian, P., Reits, D., Spekreijse, H., & Van Dorp, D. (1983). A decisive electrophysiological test for human albinism. *Electroencephalography and clinical neurophysiology, 55*(5), 513–531.

Al-Araimi, M., Pal, B., Poulter, J. A., van Genderen, M. M., Carr, I., Cudrnak, T., . . . Bradbury, J. et al., (2013). A new recessively inherited disorder composed of foveal hypoplasia, optic nerve decussation defects and anterior segment dysgenesis maps to chromosome 16q23. 3-24.1. *Molecular vision, 19*, 2165.

Arngrim, N., Hougaard, A., Ahmadi, K., Vestergaard, M. B., Schytz, H. W., Amin, F. M.,
    . . . Ashina, M. (2017a). Heterogenous migraine aura symptoms correlate with visual
    cortex functional magnetic resonance imaging responses. *Annals of neurology*, *82*(6),
    925–939.

Arngrim, N., Hougaard, A., Schytz, H. W., Vestergaard, M. B., Britze, J., Amin, F. M.,
    . . . Ashina, M. (2017b). Effect of hypoxia on BOLD fMRI response and total cere-
    bral blood flow in migraine with aura patients. *Journal of Cerebral Blood Flow &*
    Metabolism, 0271678X17719430.

Arngrim, N., Schytz, H. W., Britze, J., Amin, F. M., Vestergaard, M. B., Hougaard, A.,
    . . . Secher, N. H. et al., (2015). Migraine induced by hypoxia: an MRI spectroscopy
    and angiography study. *Brain*, *139*(3), 723–737.

Arrico, L., Giannotti, R., Fratipietro, M., & Malagola, R. (2016). Fascicular visual field
    defects in open-angle glaucoma: evaluation with microperimetry. *Journal of oph-*
    thalmology, *2016*.

Ashtari, M., Cyckowski, L. L., Monroe, J. F., Marshall, K. A., Chung, D. C., Auricchio,
    A., . . . Shindler, K. S. et al., (2011). The human visual cortex responds to gene
    therapy–mediated recovery of retinal function. *The Journal of clinical investigation*,
    121(6), 2160–2168.

Ather, S., Proudlock, F. A., Welton, T., Morgan, P. S., Sheth, V., Gottlob, I., & Dineen,
    R. A. (2019). Aberrant visual pathway development in albinism: From retina to
    cortex. *Human brain mapping*, *40*(3), 777–788.

Ayata, C. & Lauritzen, M. (2015). Spreading depression, spreading depolarizations, and
    the cerebral vasculature. *Physiological reviews*, *95*(3), 953–993.

Bach, M. (1996). The Freiburg Visual Acuity Test-automatic measurement of visual acu-
    ity. *Optometry & Vision Science*, *73*(1), 49–53.

Bach, M. (1997). Anti-aliasing and dithering in the'Freiburg Visual Acuity Test'. *Spatial*
    Vision, *11*(1), 85–89.

Bach, M. (2006). The Freiburg Visual Acuity Test-variability unchanged by post-hoc re-
    analysis. *Graefe's Archive for Clinical and Experimental Ophthalmology*, *245*(7),
    965–971.

Bach, M. & Schäfer, K. (2016). Visual acuity testing: feedback affects neither outcome
    nor reproducibility, but leaves participants happier. *PloS one*, *11*(1), e0147803.

Baden, T., Berens, P., Franke, K., Rosón, M. R., Bethge, M., & Euler, T. (2016). The
    functional diversity of retinal ganglion cells in the mouse. *Nature*, *529*(7586), 345–
    350.

Bandettini, P. A. & Ungerleider, L. G. (2001). From neuron to BOLD: new connections.
    Nature neuroscience, *4*(9), 864–866.

Bandettini, P. A., Wong, E. C., Hinks, R. S., Tikofsky, R. S., & Hyde, J. S. (1992). Time
    course EPI of human brain function during task activation. *Magnetic resonance in*
    medicine, *25*(2), 390–397.

Bao, P., Purington, C. J., & Tjan, B. S. (2015). Using an achiasmic human visual system
    to quantify the relationship between the fMRI BOLD signal and neural response.
    Elife, *4*.

Baseler, H. A., Brewer, A. A., Sharpe, L. T., Morland, A. B., Jägle, H., & Wandell, B. A. (2002). Reorganization of human cortical maps caused by inherited photoreceptor abnormalities. *Nature neuroscience*, *5*(4), 364.

Baseler, H. A., Gouws, A., Haak, K. V., Racey, C., Crossland, M. D., Tufail, A., ... Morland, A. B. (2011). Large-scale remapping of visual cortex is absent in adult humans with macular degeneration. *Nature neuroscience*, *14*(5), 649–655.

Bazin, P.-L. & Pham, D. L. (2007). Topology-preserving tissue classification of magnetic resonance brain images. *IEEE transactions on medical imaging*, *26*(4), 487–496.

Beckmann, C. F., DeLuca, M., Devlin, J. T., & Smith, S. M. (2005). Investigations into resting-state connectivity using independent component analysis. *Philosophical Transactions of the Royal Society of London B: Biological Sciences*, *360*(1457), 1001–1013.

Binda, P., Thomas, J. M., Boynton, G. M., & Fine, I. (2013). Minimizing biases in estimating the reorganization of human visual areas with BOLD retinotopic mapping. *Journal of vision*, *13*(7), 13–13.

Birn, R. M., Bandettini, P. A., Cox, R. W., & Shaker, R. (1999). Event-related fMRI of tasks involving brief motion. *Human brain mapping*, *7*(2), 106–114.

Birn, R. M., Smith, M. A., Jones, T. B., & Bandettini, P. A. (2008). The respiration response function: the temporal dynamics of fMRI signal fluctuations related to changes in respiration. *Neuroimage*, *40*(2), 644–654.

Biswal, B. B., Kylen, J. V., & Hyde, J. S. (1997). Simultaneous assessment of flow and BOLD signals in resting-state functional connectivity maps. *NMR in Biomedicine*, *10*(45), 165–170.

Biswal, B., Zerrin Yetkin, F., Haughton, V. M., & Hyde, J. S. (1995). Functional connectivity in the motor cortex of resting human brain using echo-planar mri. *Magnetic resonance in medicine*, *34*(4), 537–541.

Boynton, G. M., Engel, S. A., Glover, G. H., & Heeger, D. J. (1996). Linear systems analysis of functional magnetic resonance imaging in human V1. *Journal of Neuroscience*, *16*(13), 4207–4221.

Brainard, D. H. & Vision, S. (1997). The psychophysics toolbox. *Spatial vision*, *10*, 433–436.

Brewer, A. A. & Barton, B. (2014). Visual cortex in aging and Alzheimer's disease: changes in visual field maps and population receptive fields. *Frontiers in psychology*, *5*.

Brewer, A. A., Liu, J., Wade, A. R., & Wandell, B. A. (2005). Visual field maps and stimulus selectivity in human ventral occipital cortex. *Nature neuroscience*, *8*(8), 1102–1109.

Brown, M. & Semelka, R. C. (2003). *MRI : Basic Principles and Applications: 3rd ed.* Wiley-Liss.

Brown, S. a., Weih, L., Mukesh, N., McCarty, C., & Taylor, H. (2001). Assessment of adult stereopsis using the Lang 1 Stereotest: a pilot study. *Binocular vision & strabismus quarterly*, *16*(2), 91–98.

Calhoun, V. D., Adali, T., Pearlson, G. D., & Pekar, J. (2001). A method for making group inferences from functional MRI data using independent component analysis. *Human brain mapping*, *14*(3), 140–151.

Cang, J., Kaneko, M., Yamada, J., Woods, G., Stryker, M. P., & Feldheim, D. A. (2005). Ephrin-as guide the formation of functional maps in the visual cortex. *Neuron*, *48*(4), 577–589.

Carrera, E. & Tononi, G. (2014). Diaschisis: past, present, future. *Brain*, *137*(9), 2408–2422.

Caruyer, E., Lenglet, C., Sapiro, G., & Deriche, R. (2013). Design of multishell sampling schemes with uniform coverage in diffusion MRI. *Magnetic resonance in medicine*, *69*(6), 1534–1540.

Carvalho, J., Ahmadi, K., Invernizzi, A., Hoffmann, M. B., Renken, R., & Cornelissen, F. W. (2019). Micro-probing the visual cortex: high-resolution mapping of neuronal sub-populations. *Organization for Human Brain Mapping (OHBM), Rome, Italy.*

Chang, C., Cunningham, J. P., & Glover, G. H. (2009). Influence of heart rate on the BOLD signal: the cardiac response function. *Neuroimage*, *44*(3), 857–869.

Chen, C.-C., Bockisch, C. J., Olasagasti, I., Weber, K. P., Straumann, D., & Huang, M. Y.-Y. (2014). Positive or negative feedback of optokinetic signals: degree of the misrouted optic flow determines system dynamics of human ocular motor behavior. *Investigative ophthalmology & visual science*, *55*(4), 2297–2306.

Chen, F. K., Patel, P. J., Xing, W., Bunce, C., Egan, C., Tufail, A. T., ... Da Cruz, L. (2009). Test–retest variability of microperimetry using the Nidek MP1 in patients with macular disease. *Investigative ophthalmology & visual science*, *50*(7), 3464–3472.

Cooper, M. L. & Blasdel, G. G. (1980). Regional variation in the representation of the visual field in the visual cortex of the Siamese cat. *Journal of comparative Neurology*, *193*(1), 237–253.

Creel, D. (1979). Luminance-onset, pattern-onset and pattern-reversal evoked potentials in human albinos demonstrating visual system anomalies. *Journal of biomedical engineering*, *1*(2), 100–104.

Creel, D. J. (1971). Visual system anomaly associated with albinism in the cat. *Nature*, *231*(5303), 465.

Davies-Thompson, J., Scheel, M., Lanyon, L. J., & Barton, J. J. S. (2013). Functional organisation of visual pathways in a patient with no optic chiasm. *Neuropsychologia*, *51*(7), 1260–1272.

DeYoe, E. A., Carman, G. J., Bandettini, P., Glickman, S., Wieser, J., Cox, R., ... Neitz, J. (1996). Mapping striate and extrastriate visual areas in human cerebral cortex. *Proceedings of the National Academy of Sciences*, *93*(6), 2382–2386.

Dijkstra, E. W. (1959). A note on two problems in connexion with graphs. *Numerische mathematik*, *1*(1), 269–271.

Dougherty, R. F., Koch, V. M., Brewer, A. A., Fischer, B., Modersitzki, J., & Wandell, B. A. (2003). Visual field representations and locations of visual areas V1/2/3 in human visual cortex. *Journal of vision*, *3*(10), 1–1.

Dumoulin, S. O. & Wandell, B. A. (2008). Population receptive field estimates in human visual cortex. *Neuroimage*, *39*(2), 647–660.

Duncan, R. O. & Boynton, G. M. (2003). Cortical magnification within human primary visual cortex correlates with acuity thresholds. *Neuron*, *38*(4), 659–671.

Duong, T. Q. (2007). Cerebral blood flow and BOLD fMRI responses to hypoxia in awake and anesthetized rats. *Brain research, 1135*, 186–194.

Eick, C., Ahmadi, K., Sweeney-Reed, C. M., & Hoffmann, M. B. (2019). Interocular transfer of visual memory–Influence of visual impairment and abnormalities of the optic chiasm. *Neuropsychologia.*

Engel, S. A., Glover, G. H., & Wandell, B. A. (1997). Retinotopic organization in human visual cortex and the spatial precision of functional MRI. *Cerebral cortex (New York, NY: 1991), 7*(2), 181–192.

Engel, S. A., Rumelhart, D. E., Wandell, B. A., Lee, A. T., Glover, G. H., Chichilnisky, E.-J., & Shadlen, M. N. (1994). fMRI of human visual cortex. *Nature.*

Erskine, L. & Herrera, E. (2014). Connecting the retina to the brain. *ASN neuro, 6*(6), 1759091414562107.

Felleman, D. J. & Van Essen, D. C. (1987). Receptive field properties of neurons in area V3 of macaque monkey extrastriate cortex. *Journal of neurophysiology, 57*(4), 889–920.

Fletcher, R. & Powell, M. J. (1963). A rapidly convergent descent method for minimization. *The computer journal, 6*(2), 163–168.

Forrester, J. V., Dick, A. D., McMenamin, P. G., Roberts, F., & Pearlman, E. (2015). *The Eye E-Book: Basic Sciences in Practice.* Elsevier Health Sciences.

Fracasso, A., Koenraads, Y., Porro, G. L., & Dumoulin, S. O. (2016). Bilateral population receptive fields in congenital hemihydranencephaly. *Ophthalmic and Physiological Optics, 36*(3), 324–334.

Fracasso, A., Luijten, P. R., Dumoulin, S. O., & Petridou, N. (2018). Laminar imaging of positive and negative BOLD in human visual cortex at 7 T. *Neuroimage, 164*, 100–111.

Friston, K. J., Fletcher, P., Josephs, O., Holmes, A., Rugg, M., & Turner, R. (1998). Event-related fMRI: characterizing differential responses. *Neuroimage, 7*(1), 30–40.

Glover, G. H. (2011). Overview of functional magnetic resonance imaging. *Neurosurgery Clinics of North America, 22*(2), 133–139.

Gravel, N., Harvey, B., Nordhjem, B., Haak, K. V., Dumoulin, S. O., Renken, R., … Cornelissen, F. W. (2014). Cortical connective field estimates from resting state fMRI activity. *Frontiers in neuroscience, 8*.

Grenga, P., Lupo, S., Domanico, D., & Vingolo, E. M. (2008). Efficacy of intravitreal triamcinolone acetonide in long standing diabetic macular edema: a microperimetry and optical coherence tomography study. *Retina, 28*(9), 1270–1275.

Grill-Spector, K. & Malach, R. (2004). The human visual cortex. *Annu. Rev. Neurosci. 27*, 649–677.

Grønskov, K., Ek, J., & Brondum-Nielsen, K. (2007). Oculocutaneous albinism. *Orphanet journal of rare diseases, 2*(1), 43.

Guillery, R. (1986). Neural abnormalities of albinos. *Trends in neurosciences, 9*, 364–367.

Guillery, R., Hickey, T., Kaas, J., Felleman, D., Debruyn, E., & Sparks, D. L. (1984). Abnormal central visual pathways in the brain of an albino green monkey (Cercopithecus aethiops). *Journal of Comparative Neurology, 226*(2), 165–183.

Guillery, R., Okoro, A. N., & Witkop, C. J. (1975). Abnormal vision pathways in the brain of a human albino. *Brain research.*

Gustavsson, A., Svensson, M., Jacobi, F., Allgulander, C., Alonso, J., Beghi, E., . . . Fratiglioni, L. et al., (2011). Cost of disorders of the brain in Europe 2010. *European neuropsychopharmacology*, *21*(10), 718–779.

Haak, K. V., Winawer, J., Harvey, B. M., Renken, R., Dumoulin, S. O., Wandell, B. A., & Cornelissen, F. W. (2013). Connective field modeling. *Neuroimage*, *66*, 376–384.

Hadjikhani, N., del Rio, M. S., Wu, O., Schwartz, D., Bakker, D., Fischl, B., . . . Tootell, R. B. et al., (2001). Mechanisms of migraine aura revealed by functional MRI in human visual cortex. *Proceedings of the National Academy of Sciences*, *98*(8), 4687–4692.

Han, X., Pham, D. L., Tosun, D., Rettmann, M. E., Xu, C., & Prince, J. L. (2004). CRUISE: cortical reconstruction using implicit surface evolution. *NeuroImage*, *23*(3), 997–1012.

Hanout, M., Horan, N., & Do, D. V. (2015). Introduction to microperimetry and its use in analysis of geographic atrophy in age-related macular degeneration. *Current opinion in ophthalmology*, *26*(3), 149–156.

Hartline, H. K. (1938). The response of single optic nerve fibers of the vertebrate eye to illumination of the retina. *American Journal of Physiology–Legacy Content*, *121*(2), 400–415.

Harvey, B. M. & Dumoulin, S. O. (2011). The relationship between cortical magnification factor and population receptive field size in human visual cortex: constancies in cortical architecture. *Journal of Neuroscience*, *31*(38), 13604–13612.

Harvey, B. M., Klein, B. P., Petridou, N., & Dumoulin, S. O. (2013). Topographic representation of numerosity in the human parietal cortex. *Science*, *341*(6150), 1123–1126.

Heckenlively, J. R., Arden, G. B., & Bach, M. (2006). *Principles and practice of clinical electrophysiology of vision*. MIT press.

Heeger, D. J. & Ress, D. (2002). What does fMRI tell us about neuronal activity? *Nature Reviews Neuroscience*, *3*(2), 142–151.

Heinzle, J., Kahnt, T., & Haynes, J.-D. (2011). Topographically specific functional connectivity between visual field maps in the human brain. *Neuroimage*, *56*(3), 1426–1436.

Hoffmann, M. B. & Dumoulin, S. O. (2015). Congenital visual pathway abnormalities: a window onto cortical stability and plasticity. *Trends in neurosciences*, *38*(1), 55–65.

Hoffmann, M. B., Kaule, F. R., Levin, N., Masuda, Y., Kumar, A., Gottlob, I., . . . Wolynski, B. et al., (2012). Plasticity and stability of the visual system in human achiasma. *Neuron*, *75*(3), 393–401.

Hoffmann, M. B., Lorenz, B., Morland, A. B., & Schmidtborn, L. C. (2005). Misrouting of the optic nerves in albinism: estimation of the extent with visual evoked potentials. *Investigative ophthalmology & visual science*, *46*(10), 3892–3898.

Hoffmann, M. B., Lorenz, B., Preising, M., & Seufert, P. S. (2006). Assessment of cortical visual field representations with multifocal VEPs in control subjects, patients with albinism, and female carriers of ocular albinism. *Investigative ophthalmology & visual science*, *47*(7), 3195–3201.

Hoffmann, M. B., Seufert, P. S., & Bach, M. (2004). Simulated nystagmus suppresses pattern-reversal but not pattern-onset visual evoked potentials. *Clinical neurophysiology, 115*(11), 2659–2665.

Hoffmann, M. B., Seufert, P. S., & Schmidtborn, L. C. (2007). Perceptual relevance of abnormal visual field representations: static visual field perimetry in human albinism. *British journal of ophthalmology, 91*(4), 509–513.

Hoffmann, M. B., Tolhurst, D. J., Moore, A. T., & Morland, A. B. (2003). Organization of the visual cortex in human albinism. *Journal of Neuroscience, 23*(26), 8921–8930.

Hoffmann, M. B., Wolynski, B., Bach, M., Meltendorf, S., Behrens-Baumann, W., & Golla, F. (2011). Optic nerve projections in patients with primary ciliary dyskinesia. *Investigative ophthalmology & visual science, 52*(7), 4617–4625.

Holm, S. (1979). A simple sequentially rejective multiple test procedure. *Scandinavian journal of statistics*, 65–70.

Hougaard, A., Amin, F. M., Hoffmann, M. B., Rostrup, E., Larsson, H. B., Asghar, M. S., ... Ashina, M. (2014). Interhemispheric differences of fMRI responses to visual stimuli in patients with side-fixed migraine aura. *Human brain mapping, 35*(6), 2714–2723.

Hougaard, A., Amin, F., Hauge, A. W., Ashina, M., & Olesen, J. (2013). Provocation of migraine with aura using natural trigger factors. *Neurology, 80*(5), 428–431.

Huang, K. & Guillery, R. (1985). A demonstration of two distinct geniculocortical projection patterns in albino ferrets. *Developmental Brain Research, 20*(2), 213–220.

Hubel, D. H. & Wiesel, T. N. (1968). Receptive fields and functional architecture of monkey striate cortex. *The Journal of physiology, 195*(1), 215–243.

Hubel, D. & Wiesel, T. (1971). Aberrant visual projections in the Siamese cat. *The Journal of physiology, 218*(1), 33–62.

Huberman, A. D., Feller, M. B., & Chapman, B. (2008). Mechanisms underlying development of visual maps and receptive fields. *Annu. Rev. Neurosci. 31*, 479–509.

Ilia, M. & Jeffery, G. (1999). Retinal mitosis is regulated by dopa, a melanin precursor that may influence the time at which cells exit the cell cycle: analysis of patterns of cell production in pigmented and albino retinae. *Journal of Comparative Neurology, 405*(3), 394–405.

In, M.-H. & Speck, O. (2012). Highly accelerated PSF-mapping for EPI distortion correction with improved fidelity. *Magnetic Resonance Materials in Physics, Biology and Medicine, 25*(3), 183–192.

Jasper, H. H. (1958). The ten twenty electrode system of the international federation. *Electroencephalography and Clinical Neuroph siology, 10*, 371–375.

Jeffery, G. (2001). Architecture of the optic chiasm and the mechanisms that sculpt its development. *Physiological reviews, 81*(4), 1393–1414.

Jeffery, G. & Erskine, L. (2005). Variations in the architecture and development of the vertebrate optic chiasm. *Progress in retinal and eye research, 24*(6), 721–753.

Jeurissen, B., Tournier, J.-D., Dhollander, T., Connelly, A., & Sijbers, J. (2014). Multi-tissue constrained spherical deconvolution for improved analysis of multi-shell diffusion MRI data. *NeuroImage, 103*, 411–426.

Jezzard, P., Matthews, P. M., & Smith, S. M. (2002). *Functional Magnetic Resonance Imaging: An Introduction to Methods*. Oxford University Press.

Kaas, J., Huerta, M., Weber, J., & Harting, J. (1978). Patterns of retinal terminations and laminar organization of the lateral geniculate nucleus of primates. *Journal of Comparative Neurology*, *182*(3), 517–553.

Kaule, F. R., Wolynski, B., Gottlob, I., Stadler, J., Speck, O., Kanowski, M., . . . Hoffmann, M. B. (2014). Impact of chiasma opticum malformations on the organization of the human ventral visual cortex. *Human brain mapping*, *35*(10), 5093–5105.

Kay, K. N., Winawer, J., Rokem, A., Mezer, A., & Wandell, B. A. (2013). A two-stage cascade model of BOLD responses in human visual cortex. *PLoS computational biology*, *9*(5), e1003079.

Keliris, G. A., Li, Q., Papanikolaou, A., Logothetis, N. K., & Smirnakis, S. M. (2019). Estimating average single-neuron visual receptive field sizes by fMRI. *Proceedings of the National Academy of Sciences*, *116*(13), 6425–6434.

Kemper, V. G., De Martino, F., Emmerling, T. C., Yacoub, E., & Goebel, R. (2018). High resolution data analysis strategies for mesoscale human functional MRI at 7 and 9.4 T. *NeuroImage*, *164*, 48–58.

Klein, B. P., Fracasso, A., van Dijk, J. A., Paffen, C. L., Te Pas, S. F., & Dumoulin, S. O. (2018). Cortical depth dependent population receptive field attraction by spatial attention in human V1. *NeuroImage*, *176*, 301–312.

Klemen, J., Hoffmann, M. B., & Chambers, C. D. (2012). Cortical plasticity in the face of congenitally altered input into V1. *cortex*, *48*(10), 1362–1365.

Kupfer, C., Chumbley, L., & Downer, J. d. C. (1967). Quantitative histology of optic nerve, optic tract and lateral geniculate nucleus of man. *Journal of anatomy*, *101*(Pt 3), 393.

Lang, J. (1983). A new stereotest. *Journal of pediatric ophthalmology and strabismus*, *20*(2), 72–74.

Lauritzen, M. & Olesen, J. (1984). Regional cerebral blood flow during migraine attacks by Xenon-133 inhalation and emission tomography. *Brain*, *107*(2), 447–461.

Lee, S., Papanikolaou, A., Logothetis, N. K., Smirnakis, S. M., & Keliris, G. A. (2013). A new method for estimating population receptive field topography in visual cortex. *Neuroimage*, *81*, 144–157.

Leo, A. & Morison, R. (1945). Propagation of spreading cortical depression. *Journal of Neurophysiology*, *8*(1), 33–45.

Leske, D. A. & Holmes, J. M. (2004). Maximum angle of horizontal strabismus consistent with true stereopsis. *Journal of American Association for Pediatric Ophthalmology and Strabismus*, *8*(1), 28–34.

Levin, N., Dumoulin, S. O., Winawer, J., Dougherty, R. F., & Wandell, B. A. (2010). Cortical maps and white matter tracts following long period of visual deprivation and retinal image restoration. *Neuron*, *65*(1), 21–31.

Lieberman, H. R. & Pentland, A. P. (1982). Microcomputer-based estimation of psychophysical thresholds: the best PEST. *Behavior Research Methods*, *14*(1), 21–25.

Lindblad, M., Hougaard, A., Amin, F. M., & Ashina, M. (2017). Can migraine aura be provoked experimentally? A systematic review of potential methods for the provocation of migraine aura. *Cephalalgia*, *37*(1), 74–88.

Livingstone, M. & Hubel, D. (1988). Segregation of form, color, movement, and depth: anatomy, physiology, and perception. *Science*, *240*(4853), 740–749.

Logothetis, N. K., Pauls, J., Augath, M., Trinath, T., & Oeltermann, A. (2001). Neurophysiological investigation of the basis of the fMRI signal. *Nature, 412*(6843), 150.

Logothetis, N. K. & Wandell, B. A. (2004). Interpreting the BOLD signal. *Annu. Rev. Physiol. 66*, 735–769.

Luck, S. J. (2005). *An introduction to the event-related potential technique.* MIT press.

Mackey, W. E., Winawer, J., & Curtis, C. E. (2017). Visual field map clusters in human frontoparietal cortex. *Elife, 6*.

Mansfield, P. (1977). Multi-planar image formation using NMR spin echoes. *Journal of Physics C: Solid State Physics, 10*(3), L55.

Masuda, Y., Dumoulin, S. O., Nakadomari, S., & Wandell, B. A. (2008). V1 projection zone signals in human macular degeneration depend on task, not stimulus. *Cerebral cortex, 18*(11), 2483–2493.

Maunsell, J. & van Essen, D. C. (1983). The connections of the middle temporal visual area (MT) and their relationship to a cortical hierarchy in the macaque monkey. *Journal of Neuroscience, 3*(12), 2563–2586.

McLaughlin, T. & O'Leary, D. D. (2005). Molecular gradients and development of retinotopic maps. *Annu. Rev. Neurosci. 28*, 327–355.

McRobbie, D. W., Moore, E. A., Graves, M. J., & Prince, M. R. (2007). *MRI from Picture to Proton: 2nd ed.* Cambridge University Press.

Midena, E., Radin, P. P., Pilotto, E., Ghirlando, A., Convento, E., & Varano, M. (2004). Fixation pattern and macular sensitivity in eyes with subfoveal choroidal neovascularization secondary to age-related macular degeneration. A microperimetry study. In *Seminars in ophthalmology* (Vol. 19, *1-2*, pp. 55–61). Taylor & Francis.

Midena, E., Vujosevic, S., Convento, E., Cavarzeran, F., Pilotto, E. et al., (2007). Microperimetry and fundus autofluorescence in patients with early age-related macular degeneration. *British Journal of Ophthalmology, 91*(11), 1499–1503.

Molina-Martin, A., Pinero, D. P., & Perez-Cambrodi, R. J. (2015). Fixation pattern analysis with microperimetry in nystagmus patients. *Canadian Journal of Ophthalmology/Journal Canadien d'Ophtalmologie, 50*(6), 413–421.

Morland, A. B. (2015). Organization of the central visual pathways following field defects arising from congenital, inherited, and acquired eye disease. *Annual review of vision science, 1*, 329–350.

Morland, A. B., Baseler, H. A., Hoffmann, M. B., Sharpe, L. T., & Wandell, B. A. (2001). Abnormal retinotopic representations in human visual cortex revealed by fMRI. *Acta psychologica, 107*(1-3), 229–247.

Muckli, L., Naumer, M. J., & Singer, W. (2009). Bilateral visual field maps in a patient with only one hemisphere. *Proceedings of the National Academy of Sciences, 106*(31), 13034–13039.

Odom, J. V., Bach, M., Brigell, M., Holder, G. E., McCulloch, D. L., Tormene, A. P. et al., (2010). ISCEV standard for clinical visual evoked potentials (2009 update). *Documenta ophthalmologica, 120*(1), 111–119.

Oetting, W. S. (1999). Albinism. *Current opinion in pediatrics, 11*(6), 565–571.

of the International Headache Society (IHS), H. C. C. (2013). The international classification of headache disorders, (beta version). *Cephalalgia, 33*(9), 629–808.

Ogawa, S., Menon, R., Kim, S., & Ugurbil, K. (1998). On the characteristics of functional magnetic resonance imaging of the brain. *Annual review of biophysics and biomolecular structure, 27*(1), 447–474.

Ogawa, S., Lee, T.-M., Kay, A. R., & Tank, D. W. (1990). Brain magnetic resonance imaging with contrast dependent on blood oxygenation. *Proceedings of the National Academy of Sciences, 87*(24), 9868–9872.

Olesen, J., Gustavsson, A., Svensson, M., Wittchen, H.-U., & Jönsson, B. (2012). The economic cost of brain disorders in Europe. *European journal of neurology, 19*(1), 155–162.

Olesen, J., Tfelt-Hansen, P., & Welch, K. (2000). *The Headaches.* Lippincott Williams & Wilkins.

Olesen, J., Friberg, L., Olsen, T. S., Iversen, H. K., Lassen, N. A., Andersen, A. R., & Karle, A. (1990). Timing and topography of cerebral blood flow, aura, and headache during migraine attacks. *Annals of neurology, 28*(6), 791–798.

Olesen, J., Larsen, B., & Lauritzen, M. (1981). Focal hyperemia followed by spreading oligemia and impaired activation of rCBF in classic migraine. *Annals of neurology, 9*(4), 344–352.

Olman, C. A., Bao, P., Engel, S. A., Grant, A. N., Purington, C., Qiu, C., . . . Tjan, B. S. (2016). Hemifield columns co-opt ocular dominance column structure in human achiasma. *Neuroimage.*

Papanikolaou, A., Keliris, G. A., Lee, S., Logothetis, N. K., & Smirnakis, S. M. (2015). Nonlinear population receptive field changes in human area V5/MT+ of healthy subjects with simulated visual field scotomas. *NeuroImage, 120,* 176–190.

Parker, A. J., Smith, J. E., & Krug, K. (2016). Neural architectures for stereo vision. *Phil. Trans. R. Soc. B, 371*(1697), 20150261.

Pavone, P., Nigro, F., Falsaperla, R., Greco, F., Ruggieri, M., Rizzo, R., . . . Pavone, L. (2013). Hemihydranencephaly: living with half brain dysfunction. *Italian journal of pediatrics, 39*(1), 3.

Pelli, D. G. (1997). The VideoToolbox software for visual psychophysics: Transforming numbers into movies. *Spatial vision, 10*(4), 437–442.

Plank, T., Rosengarth, K., Schmalhofer, C., Goldhacker, M., Brandl-Rühle, S., & Greenlee, M. W. (2014). Perceptual learning in patients with macular degeneration. *Frontiers in psychology, 5,* 1189.

Poulter, J. A., Al-Araimi, M., Conte, I., van Genderen, M. M., Sheridan, E., Carr, I. M., . . . Bradbury, J. et al., (2013). Recessive mutations in SLC38A8 cause foveal hypoplasia and optic nerve misrouting without albinism. *The American Journal of Human Genetics, 93*(6), 1143–1150.

Provis, J. M., Diaz, C. M., & Dreher, B. (1998). Ontogeny of the primate fovea: a central issue in retinal development. *Progress in neurobiology, 54*(5), 549–581.

Puzniak, R. J., Ahmadi, K., Kaufmann, J., Gouws, A. D., Morland, A. B., Pestilli, F., & Hoffmann, M. B. (2019). Quantification of nerve decussation abnormalities in the optic chiasm. *Organization for Human Brain Mapping (OHBM), Rome, Italy.*

Queiroz, L. P., Friedman, D. I., Rapoport, A. M., & Purdy, R. A. (2011). Characteristics of migraine visual aura in Southern Brazil and Northern USA. *Cephalalgia, 31*(16), 1652–1658.

Radtke, N. D., Aramant, R. B., Petry, H. M., Green, P. T., Pidwell, D. J., & Seiler, M. J. (2008). Vision improvement in retinal degeneration patients by implantation of retina together with retinal pigment epithelium. *American journal of ophthalmology*, *146*(2), 172–182.

Rohrschneider, K., Bültmann, S., & Springer, C. (2008). Use of fundus perimetry (microperimetry) to quantify macular sensitivity. *Progress in retinal and eye research*, *27*(5), 536–548.

Rosengarth, K., Keck, I., Brandl-Rühle, S., Frolo, J., Hufendiek, K., Greenlee, M. W., & Plank, T. (2013). Functional and structural brain modifications induced by oculomotor training in patients with age-related macular degeneration. *Frontiers in psychology*, *4*, 428.

Rostrup, E., Larsson, H. B., Born, A. P., Knudsen, G. M., & Paulson, O. B. (2005). Changes in BOLD and ADC weighted imaging in acute hypoxia during sea-level and altitude adapted states. *Neuroimage*, *28*(4), 947–955.

Russell, M. B. & Olesen, J. (1996). A nosographic analysis of the migraine aura in a general population. *Brain*, *119*(2), 355–361.

Saad, Z. S., Glen, D. R., Chen, G., Beauchamp, M. S., Desai, R., & Cox, R. W. (2009). A new method for improving functional-to-structural MRI alignment using local Pearson correlation. *Neuroimage*, *44*(3), 839–848.

Sanes, J. R. & Masland, R. H. (2015). The types of retinal ganglion cells: current status and implications for neuronal classification. *Annual review of neuroscience*, *38*, 221–246.

Schira, M. M., Wade, A. R., & Tyler, C. W. (2007). Two-dimensional mapping of the central and parafoveal visual field to human visual cortex. *Journal of neurophysiology*, *97*(6), 4284–4295.

Schmitz, B., Käsmann-Kellner, B., Schäfer, T., Krick, C. M., Grön, G., Backens, M., & Reith, W. (2004). Monocular visual activation patterns in albinism as revealed by functional magnetic resonance imaging. *Human brain mapping*, *23*(1), 40–52.

Schulze-Bonsel, K., Feltgen, N., Burau, H., Hansen, L., & Bach, M. (2006). Visual acuities "hand motion" and "counting fingers" can be quantified with the Freiburg visual acuity test. *Investigative Ophthalmology & Visual Science*, *47*(3), 1236–1240.

Schwarzkopf, D. S., Anderson, E. J., de Haas, B., White, S. J., & Rees, G. (2014). Larger extrastriate population receptive fields in autism spectrum disorders. *Journal of Neuroscience*, *34*(7), 2713–2724.

Schwarzkopf, D. S., Song, C., & Rees, G. (2011). The surface area of human V1 predicts the subjective experience of object size. *Nature neuroscience*, *14*(1), 28.

Sereno, M. I., Dale, A., Reppas, J., Kwong, K., Belliveau, J., Brady, T., . . . Tootell, R. (1995). Borders of multiple visual areas in humans revealed by functional magnetic resonance imaging. *Science*, *268*(5212), 889–893.

Seth, A., Culverwell, J., Walkowicz, M., Toro, S., Rick, J. M., Neuhauss, S. C., . . . Karlstrom, R. O. (2006). belladonna/(lhx2) is required for neural patterning and midline axon guidance in the zebrafish forebrain. *Development*, *133*(4), 725–735.

Sherrington, C. S. (1910). Flexion-reflex of the limb, crossed extension-reflex, and reflex stepping and standing. *The Journal of physiology*, *40*(1-2), 28–121.

Sinha, P. & Meng, M. (2012). Superimposed hemifields in primary visual cortex of achiasmic individuals. *Neuron, 75*(3), 353–355.

Smirnakis, S. M., Brewer, A. A., Schmid, M. C., Tolias, A. S., Schüz, A., Augath, M., . . . Logothetis, N. K. (2005). Lack of long-term cortical reorganization after macaque retinal lesions. *Nature, 435*(7040), 300.

Smith, R. E., Tournier, J.-D., Calamante, F., & Connelly, A. (2012). Anatomically-constrained tractography: improved diffusion MRI streamlines tractography through effective use of anatomical information. *Neuroimage, 62*(3), 1924–1938.

Solomon, S. G. & Lennie, P. (2007). The machinery of colour vision. *Nature Reviews Neuroscience, 8*(4), 276.

Stovner, L., Hagen, K., Jensen, R., Katsarava, Z., Lipton, R., Scher, A., . . . Zwart, J.-A. (2007). The global burden of headache: a documentation of headache prevalence and disability worldwide. *Cephalalgia, 27*(3), 193–210.

Striem-Amit, E. & Amedi, A. (2014). Visual cortex extrastriate body-selective area activation in congenitally blind people "seeing" by using sounds. *Current Biology, 24*(6), 687–692.

Takemura, H., Caiafa, C. F., Wandell, B. A., & Pestilli, F. (2016). Ensemble tractography. *PLoS computational biology, 12*(2), e1004692.

Tanabe, S., Doi, T., Umeda, K., & Fujita, I. (2005). Disparity-tuning characteristics of neuronal responses to dynamic random-dot stereograms in macaque visual area V4. *Journal of neurophysiology, 94*(4), 2683–2699.

Teo, P. C., Sapiro, G., & Wandell, B. A. (1997). Creating connected representations of cortical gray matter for functional MRI visualization. *IEEE transactions on medical imaging, 16*(6), 852–863.

Thomas, J. M., Huber, E., Stecker, G. C., Boynton, G. M., Saenz, M., & Fine, I. (2015). Population receptive field estimates of human auditory cortex. *NeuroImage, 105*, 428–439.

Thoreson, W. B., Babai, N., & Bartoletti, T. M. (2008). Feedback from horizontal cells to rod photoreceptors in vertebrate retina. *Journal of Neuroscience, 28*(22), 5691–5695.

Tootell, R. B. & Hadjikhani, N. (2001). Where is 'dorsal V4'in human visual cortex? Retinotopic, topographic and functional evidence. *Cerebral Cortex, 11*(4), 298–311.

Tootell, R. B., Mendola, J. D., Hadjikhani, N. K., Ledden, P. J., Liu, A. K., Reppas, J. B., . . . Dale, A. M. (1997). Functional analysis of V3A and related areas in human visual cortex. *Journal of Neuroscience, 17*(18), 7060–7078.

Tootell, R. B., Mendola, J. D., Hadjikhani, N. K., Liu, A. K., & Dale, A. M. (1998). The representation of the ipsilateral visual field in human cerebral cortex. *Proceedings of the National Academy of Sciences, 95*(3), 818–824.

Tournier, J. D., Calamante, F., & Connelly, A. (2010). Improved probabilistic streamlines tractography by 2nd order integration over fibre orientation distributions. In *Proceedings of the international society for magnetic resonance in medicine* (Vol. 18, p. 1670).

Tournier, J.-D., Calamante, F., & Connelly, A. (2013). Determination of the appropriate b value and number of gradient directions for high-angular-resolution diffusion-weighted imaging. *NMR in Biomedicine, 26*(12), 1775–1786.

Tournier, J.-D., Yeh, C.-H., Calamante, F., Cho, K.-H., Connelly, A., & Lin, C.-P. (2008). Resolving crossing fibres using constrained spherical deconvolution: validation using diffusion-weighted imaging phantom data. *Neuroimage*, *42*(2), 617–625.

Trampel, R., Ott, D. V., & Turner, R. (2011). Do the congenitally blind have a stria of Gennari? First intracortical insights in vivo. *Cerebral Cortex*, *21*(9), 2075–2081.

Tuch, D. S., Reese, T. G., Wiegell, M. R., Makris, N., Belliveau, J. W., & Wedeen, V. J. (2002). High angular resolution diffusion imaging reveals intravoxel white matter fiber heterogeneity. *Magnetic Resonance in Medicine: An Official Journal of the International Society for Magnetic Resonance in Medicine*, *48*(4), 577–582.

Van de Moortele, P.-F., Auerbach, E. J., Olman, C., Yacoub, E., Uğurbil, K., & Moeller, S. (2009). T1 weighted brain images at 7 Tesla unbiased for Proton Density, T2∗ contrast and RF coil receive B1 sensitivity with simultaneous vessel visualization. *Neuroimage*, *46*(2), 432–446.

van Genderen, M. M., Riemslag, F. C., Schuil, J., Hoeben, F., Stilma, J. S., & Meire, F. M. (2006). Chiasmal misrouting and foveal hypoplasia without albinism. *British journal of ophthalmology*, *90*(9), 1098–1102.

Vancleef, K., Read, J. C., Herbert, W., Goodship, N., Woodhouse, M., & Serrano-Pedraza, I. (2017). Overestimation of stereo thresholds by the TNO stereotest is not due to global stereopsis. *Ophthalmic and Physiological Optics*.

Viana, M., Sances, G., Linde, M., Ghiotto, N., Guaschino, E., Allena, M., . . . Tassorelli, C. (2017). Clinical features of migraine aura: results from a prospective diary-aided study. *Cephalalgia*, *37*(10), 979–989.

Victor, J. D., Apkarian, P., Hirsch, J., Conte, M. M., Packard, M., Relkin, N. R., . . . Shapley, R. M. (2000). Visual function and brain organization in non-decussating retinal–fugal fibre syndrome. *Cerebral Cortex*, *10*(1), 2–22.

Victor, J. D., Purpura, K., Katz, E., & Mao, B. (1994). Population encoding of spatial frequency, orientation, and color in macaque V1. *Journal of neurophysiology*, *72*(5), 2151–2166.

Vincent, J. L., Kahn, I., Snyder, A. Z., Raichle, M. E., & Buckner, R. L. (2008). Evidence for a frontoparietal control system revealed by intrinsic functional connectivity. *Journal of neurophysiology*, *100*(6), 3328–3342.

Vincent, M. & Hadjikhani, N. (2007). Migraine aura and related phenomena: beyond scotomata and scintillations. *Cephalalgia*, *27*(12), 1368–1377.

Von Dem Hagen, E. A., Houston, G. C., Hoffmann, M. B., & Morland, A. B. (2007). Pigmentation predicts the shift in the line of decussation in humans with albinism. *European Journal of Neuroscience*, *25*(2), 503–511.

von dem Hagen, E. A., Hoffmann, M. B., & Morland, A. B. (2008). Identifying human albinism: a comparison of VEP and fMRI. *Investigative ophthalmology & visual science*, *49*(1), 238–249.

Vujosevic, S., Midena, E., Pilotto, E., Radin, P. P., Chiesa, L., & Cavarzeran, F. (2006). Diabetic macular edema: correlation between microperimetry and optical coherence tomography findings. *Investigative Ophthalmology & Visual Science*, *47*(7), 3044–3051.

Waehnert, M., Dinse, J., Weiss, M., Streicher, M. N., Waehnert, P., Geyer, S., . . . Bazin, P.-L. (2014). Anatomically motivated modeling of cortical laminae. *Neuroimage, 93*, 210–220.

Wandell, B., Dumoulin, S., & Brewer, A. (2009). Visual cortex in humans. *Encyclopedia of neuroscience, 10*, 251–257.

Wandell, B. A., Chial, S., & Backus, B. T. (2000). Visualization and measurement of the cortical surface. *Journal of cognitive neuroscience, 12*(5), 739–752.

Wandell, B. A., Dumoulin, S. O., & Brewer, A. A. (2007). Visual field maps in human cortex. *Neuron, 56*(2), 366–383.

Wandell, B. A. & Smirnakis, S. M. (2009). Plasticity and stability of visual field maps in adult primary visual cortex. *Nature Reviews Neuroscience, 10*(12), 873.

Wandell, B. A. & Winawer, J. (2015). Computational neuroimaging and population receptive fields. *Trends in cognitive sciences, 19*(6), 349–357.

Weber, K. P. & Landau, K. (2013). Teaching NeuroImages: Mind the gap! Postfixational blindness due to traumatic rupture of the optic chiasm. *Neurology, 80*(19), e197– e198.

Welton, T., Ather, S., Proudlock, F. A., Gottlob, I., & Dineen, R. A. (2017). Altered whole-brain connectivity in albinism. *Human brain mapping, 38*(2), 740–752.

Winawer, J., Horiguchi, H., Sayres, R. A., Amano, K., & Wandell, B. A. (2010). Mapping hV4 and ventral occipital cortex: the venous eclipse. *Journal of vision, 10*(5), 1–1.

Wolynski, B., Kanowski, M., Meltendorf, S., Behrens-Baumann, W., & Hoffmann, M. B. (2010). Self-organisation in the human visual system—visuo-motor processing with congenitally abnormal V1 input. *Neuropsychologia, 48*(13), 3834–3845.

Worsley, K. J., Liao, C., Aston, J., Petre, V., Duncan, G., Morales, F., & Evans, A. (2002). A general statistical analysis for fMRI data. *Neuroimage, 15*(1), 1–15.

Declaration of criminal convictions

I hereby declare that I have not been found guilty of a criminal offence involving scientific/academic misconduct.

Magdeburg, 19. June 2019

Khazar Ahmadi

Declaration of honour

I hereby declare that I prepared this thesis without the impermissible help of third parties and that none other than the aids indicated have been used; all sources of information are clearly marked, including my own publications.

In particular I have not consciously:

- fabricated data or rejected undesirable results,

- misused statistical methods with the aim of drawing other conclusions than those warranted by the available data,

- plagiarized external data or publications,

- presented the results of other researchers in a distorted way.

I am aware that violations of copyright may lead to injunction and damage claims by the author and also to prosecution by the law enforcement authorities. I hereby agree that the thesis may be electronically reviewed with the aim of identifying plagiarism.

This work has not yet been submitted as a doctoral thesis in the same or a similar form in Germany, nor in any other country. It has not yet been published as a whole.

Magdeburg, 19. June 2019

Khazar Ahmadi

Publications

* **Ahmadi, K**., Fracasso, A., van Dijk J.A., Kruijt, C., van Genderen, M., Dumoulin, S.O., Hoffmann, M.B. (2019). Altered organization of the visual cortex in FHONDA syndrome. NeuroImage (190), 224-231.

Eick, C., **Ahmadi, K.**, Sweeney-Reed, C. M., Hoffmann, M. B. (2019). Interocular transfer of visual memory: influence of visual impairment and abnormalities of the optic chiasm. Neuropsychologia (129), 171-178.

* Arngrim†, N., Hougaard†, A., **Ahmadi††, K.**, Vestergaard††, M. B., Schytz, H. W., Amin, F. M., Larsson, H.B.W., Olesen, J., Hoffmann†††, M.B. & Ashina†††, M. (2017). Heterogenous migraine aura symptoms correlate with visual cortex functional magnetic resonance imaging responses. Annals of neurology, 82(6), 925-939. [†, ††, ††† Denote equal first, second and senior author contributions].

Hoffmann, M. B., Thieme, H., & **Ahmadi, K.** (2017). Potential of fMRI for the functional assessment of the pathological visual system. Klinische Monatsblätter für Augenheilkunde, 234(03), 303-310.

Ahmadi, K., Pouretemad, H. R., Esfandiari, J., Yoonessi, A., & Yoonessi, A. (2015). Psychophysical evidence for impaired Magno, Parvo, and Konio-cellular pathways in dyslexic children. Journal of ophthalmic & vision research, 10(4), 433-40.

* Publications directly related to this thesis.